Master's Thesis

Feasibility study of using retroreflective foils for satellite laser ranging

Machbarkeitsanalyse zur Anwendung retroreflektierender Folien für das Satelliten-Laser-Ranging

Maximilian Feiling

Reviewed by
Prof. Dr. Sangam Chatterjee
Institute of Experimental Physics I
Justus-Liebig-Universität

Prof. Dr. rer. nat. Chris Volkmar
Department of Electrical Engineering and Information Technology
Technische Hochschule Mittelhessen

Supervisor
Moritz Vogel
Institute of Technical Physics
German Aerospace Center (DLR)

November 25, 2024

Selbstständigkeitserklärung

Hiermit versichere ich, die vorgelegte Thesis selbstständig und ohne unerlaubte fremde Hilfe und nur mit den Hilfen angefertigt zu haben, die ich in der Thesis angegeben habe. Alle Textstellen, die wörtlich oder sinngemäß aus veröffentlichten Schriften entnommen sind, und alle Angaben die auf mündlichen Auskünften beruhen, sind als solche kenntlich gemacht. Bei den von mir durchgeführten und in der Thesis erwähnten Untersuchungen habe ich die Grundsätze guter wissenschaftlicher Praxis, wie sie in der ‚Satzung der Justus-Liebig-Universität zur Sicherung guter wissenschaftlicher Praxis' niedergelegt sind, eingehalten. Entsprechend § 22 Abs. 2 der Allgemeinen Bestimmungen für modularisierte Studiengänge dulde ich eine Überprüfung der Thesis mittels Anti-Plagiatssoftware.

Datum	Unterschrift

Abstract

This study is a research project for the use of retroreflective foils for satellite laser ranging and was developed in collaboration with the Institute of Technical Physics from the German Aerospace Center (Deutsches Zentrum für Luft- und Raumfahrt) in Stuttgart. Due to the continually increasing number of objects in Low Earth Orbit, space surveillance systems are becoming essential, while conventional utilized radar systems are limited in accuracy. To reduce the growing risk for satellite missions, satellite laser ranging systems could contribute to more accurate position determination. The use of this technology urges satellite operators to implement passive optics in their payloads to enhance the optical cross section. This can be in conflict with dispenser systems [1]. Indeed, some stations may be able to range targets through only diffuse scattering. However, this requires high-power laser systems and consequently incurs high costs. The use of retroreflective foils leads to a more flexible implementation and could therefore make the use of satellite laser ranging more attractive. Also P. Sauer et al. [2] emphasizes the advantages of using retroreflective foils but has only ranged them in ground-based experiments over relatively short distances. Therefore, this study offers a detailed analysis of commercially available foils, accompanied by link budget calculations. Since the structure of retroreflective foils differs from that of conventionally used retroreflectors, certain assumptions must be made regarding a describtion of the far-field diffraction pattern, the peak optical cross section and the effective area including the retroreflective output aperture as a function of the incidence angle. Therefore both a theoretical and experimental examination will support these assumptions. The optical cross section of retroreflective foils will be calculated as a function of the embedded diameter, the reflectivity, and utilized area. In addition the required area and diameter will be calculated as a function of a given optical cross section.

Zusammenfassung

Diese Studie ist eine Machbarkeitsanalyse zum Einsatz von retroreflektierenden Folien für die Laserentfernungsmessung von Satelliten und wurde in Zusammenarbeit mit dem Institut für Technische Physik des Deutschen Zentrums für Luft- und Raumfahrt in Stuttgart entwickelt. Mit der ständig steigenden Anzahl von Objekten im niedrigen Erdorbit wächst die Nachfrage nach Weltraumüberwachungssysteme, während herkömmlich genutzte Radarsysteme in ihrer Genauigkeit begrenzt sind. Um das wachsende Risiko für Satellitenmissionen zu verringern, könnten Satelliten-Laser-Ranging-Systeme zu einer genaueren Positionsbestimmung beitragen. Der Einsatz dieser Technologie fordert Satellitenbetreiber jedoch, passive Optiken in ihre Nutzlasten einzubauen, um den optischen Wirkungsquerschnitt zu verbessern. Dies kann mit Satelliten-Dispenser in Konflikt geraten [1]. Experimente haben zwar erfolgreich zeigen können, dass Laserentfernungsmessungen an Zielen über diffuse Streuung möglich sind. Dies erfordert jedoch leistungsstarke Lasersysteme und verursacht folglich hohe Kosten. Eine alternative Verwendung von retroreflektierenden Folien würde eine flexiblere Implementierung ermöglichen und könnte daher den Einsatz von SLR attraktiver machen. Auch P. Sauer et al. [2] betont die Vorteile des Einsatzes von retroreflektierenden Folien, hat aber bisher nur an bodengebundenen Zielen Laserentfernungsmessungen durchgeführt. Daher bietet diese Studie eine detaillierte Analyse von kommerziell erhältlichen retroreflektierenden Folien, um präzise den optischen Wirkungsquerschnitts und darauffolgend ein Link Budget abschätzen zu können. Da sich die Struktur von retroreflektierenden Folien von der herkömmlicher Retroreflektoren unterscheidet, müssen bestimmte Annahmen hinsichtlich einer Beschreibung des Beugungsmusters, des optischen Wirkungsquerschnitts und der effektiven Fläche einschließlich der retroreflektierenden Ausgangsöffnung in Abhängigkeit des Einfallswinkels getroffen werden. Daher wird sowohl eine theoretische als auch eine experimentelle Untersuchung diese Annahmen stützen. Der optische Wirkungsquerschnitt von retroreflektierenden Folien wird in Abhängikeit des Durchmessers der eingebetteten Retroreflektoren, des Reflexionsvermögens und der verwendeten Fläche berechnet. Außerdem werden die benötigte Fläche und der Durchmesser in Abhängigkeit eines Referenzquerschnitts gesetzt, um die Größeneinordnung in Relation zu etablierten Optiken zu erleichtern.

Contents

List of Figures

List of Tables

List of Abbrevations

ILRS	International Laser Ranging Service
DLR	Deutsches Zentrum für Luft- und Raumfahrt
OCS	Optical Cross Section
CCRs	Corner Cube Reflectors
SLR	Satellite Laser Ranging
FFDP	Far-Field Diffraction Pattern
LEO	Low Earth Orbit
EF	Element Factor
AF	Array Function
TIR	Total Internal Reflection
FFT	Fast Fourier Transformation
PSF	Point Spread Function
DIC	Differential Interference Contrast
TOF	Time-of-Flight

List of Symbols

Physical Constants

G	$6.67430 \cdot 10^{-11}\,\mathrm{kg\,m^3\,s^{-2}}$	Gravitational constant
c	$299,792,458\,\mathrm{m\,s^{-1}}$	Speed of light in vacuum
g	$9.81\,\mathrm{m\,s^{-2}}$	Acceleration due to Earth's gravity
h	$6.626,070,15 \cdot 10^{-34}\,\mathrm{kg\,m^2\,s^{-1}}$	Planck constant

Greek Symbols

Γ^2	-	Quantity
$\Delta\theta_p$	rad	Beam pointing error
$\Delta\delta_a$	m	Manufacturing error of a CCR
Ω	sr	Effective solid angle
α	rad	Velocity aberration
α_e	rad	Elevation angle
α_{max}	rad	Maximum value of the velocity aberration
α_{min}	rad	Minimum value of the velocity aberration
γ	1	Reducing factor in accordance to the stretch factor a_s
δ_a	m	Range of manufacturing tolerances
η	1	y-coordinate of point Q
η_c	1	Reducing factor of the effective area from a circular or a hexagonal CCR
η_{obs}	1	Obscuration due to the secondary mirror
η_q	1	Quantum efficiency of the detector
η_t	1	Reducing factor of the effective area from a triangular CCR
θ	rad	Diffraction angle
θ_c	rad	Cut-off angle of a CCR
$\theta_{c,\,circ}$	rad	Cut-off angle of a circular CCR
$\theta_{c,\,hex}$	rad	Cut-off angle of a hexagonal CCR
$\theta_{c,\,tria}$	rad	Cut-off angle of a triangular CCR
$\theta_{circ_{min,\,0}}$	rad	Radial size of the central maximum from a circular aperture
θ_d	rad	Far-field beam divergence half angle
$\theta_{hex_{min,\,0}}$	rad	Radial size of the central maximum from a hexagonal aperture
θ_i	rad	Angle of incidence
θ_i'	rad	Propagation angle inside the CCR
$\theta_{min,\,0}$	rad	Radial size of the central maximum in general
θ_o	rad	Off-axis angle
θ_{zen}	rad	Angle between beam and zenith

λ	m	Wavelength
μ	sr^{-1}	Normalized reduced aperture radius along the tilt direction
ξ	1	x-coordinate of point Q
π	1	Mathematical constant representing the ratio of a circle's circumference to its diameter
ρ	1	Reflectivity
ρ_{ccr}	1	Reflectivity of a CCR
ρ_{circ}	1	Reflectivity of a circular CCR
ρ_{foil}	1	Reflectivity of a retroreflective foil
σ	$\mathrm{m}^2\,\mathrm{sr}^{-1}$	OCS
σ_0	$\mathrm{m}^2\,\mathrm{sr}^{-1}$	Peak OCS
$\sigma_{0,\,circ}$	$\mathrm{m}^2\,\mathrm{sr}^{-1}$	Peak OCS of a circular CCR
$\sigma_{0,\,hex}$	$\mathrm{m}^2\,\mathrm{sr}^{-1}$	Peak OCS of a hexagonal CCR
$\sigma_{0,\,tria}$	$\mathrm{m}^2\,\mathrm{sr}^{-1}$	Peak OCS of a triangular CCR
σ_{circ}	$\mathrm{m}^2\,\mathrm{sr}^{-1}$	OCS of a circular CCR
σ_{foil}	$\mathrm{m}^2\,\mathrm{sr}^{-1}$	OCS of retroreflective foil
τ_{atm}	1	Transmission efficiency of the atmosphere
τ_c	1	Transmission efficiency of cirrus clouds
τ_{filter}	1	Transmission efficiency of the filter
τ_r	1	Transmission efficiency of receiver
τ_t	1	Transmission efficiency of transmitter
ϕ	1	Phase distribution of the aperture function
φ	rad	Angle for components of R in the calculation of velocity aberration
ω	rad	Satellite movement

Latin Symbols

$\mathcal{A}$	1	Opening screen, from Section 2.1.1 defined as aperture function
$\mathcal{A}_0$	1	Amplitude distribution of the aperture function
$A_{1,\,hex}$	m^2	Required area of retroreflective foil to achieve an OCS equivalent to that of a circular CCR.
A	depending	Wave amplitude
A_{ccr}	m^2	Retroreflecting area of a circular CCR
A_r	m^2	Receiver aperture
A_q	m^2	Area of retroreflective foil
C	-	Quantity
C_1	1	Integral of intensity distribution of $I_{circ}(\theta)$
C_2	1	Integral of intensity distribution of $I_{hex}(\theta)$
D_{ccr}	m	Diameter of the retroreflecting area from a CCR
D_{circ}	m	Diameter of a circular CCR
D_{hex}	m	Diameter of the hexagonal output aperture from a hexagonal or a triangular CCR
D_r	m	Diameter of the receiving system

D_{tria}	m	Required diameter of the hexagonal output aperture from a triangular CCR to achieve an OCS equivalent to that of a circular CCR
E_h	1	Plane of face from a hexagonal CCR
E_p	Ws	Pulse energy of the laser
E_t	1	Plane of face from a triangular CCR
G_t	1	Gain of the transmitter
I_0	Wm^{-2}	Amplitude of angular intensity distribution
I_{circ}	Wm^{-2}	Angular intensity distribution of circular aperture
I_{hex}	Wm^{-2}	Angular intensity distribution of hexagonal aperture
J_0	1	Bessel function of the first kind of zero order
J_1	1	Bessel function of the first kind of first order
L	Wm^{-2}	Total intensity contained within each maximum from the Airy function
L_{ccr}	m	Length of a CCR
L_{circ}	m	Length of a circular CCR
L_{hex}	m	Length of a hexagonal CCR
L_{tria}	m	Length of a triangular CCR
M_E	kg	Mass of earth
N	1	Number of pixels
N'_F	1	Indicator for Fraunhofer conditions
N_{pe}	1	Mean numbers of photons recording by ranging detector per pulse
N_t	1	Total numbers of photons emitted per laser pulse
N_{tr}	1	Threshold detection number
P	1	Point in accordance to Figure 2.1
P_0	1	Point in accordance to Figure 2.1
P_d	1	Rate of detection
P_x	$\frac{\mathrm{Pixel}}{\mathrm{mm}}$	Pixel resolution
Q	1	Point in accordance to Figure 2.1
R	m	Slant Range
R_E	m	Earth radius
R_x	m	x-component from the vector quantity of the slant range
R_y	m	y-component from the vector quantity of the slant range
U_P	-	Complex amplitude from diffracted wave at point P
$U(r)$	-	Complex amplitude of a monochromatic spherical wave at distance r
a_c	m	Edge length of the hexagonal and triangular CCRs for constructing
a_s	1	Stretch factor
a_{sat}	m	Quadratic edge length of retroreflective foil
a_c	m	Edge length of an equilateral triangle from a triangular CCR
d	m	Distance between the screen and the wall in the setup
d_h	m	Projected edge length
dS	1	Integral surface
e	1	Euler's number
h_{sat}	m	Altitude of satellite above sea level

$h_{station}$	m	Altitude of SLR station above sea level
i	1	Imaginary number
k	m^{-1}	wavenumber
k_n	1	Number of occurrences in the Poisson distribution
k_x	m^{-1}	Spatial frequency of the aperture function
k_y	m^{-1}	Spatial frequency of the aperture function
n	1	Number of different quantities
n_{hex}	1	Number of hexagonal CCRs in retroreflective foil
n_{ref}	1	Refractive index
n_s	1	Normal vector of the integral surface dS
n_{tria}	1	Number of triangular CCRs in retroreflective foil
r	m	Distance from Point P_0 to Q
r'	m	Distance from Point P_0 to O
$\hat{r}$	1	Unit vector in direction from the SLR station to the satellite
r_{circ}	m	Radius of a circular aperture
r_{hex}	m	Radius of a hexagonal aperture
s	m	Distance from Point Q to P
s'	m	Distance from Point O to P
$\hat{s}$	1	Unit vector in direction from the satellite's movement in space
$\hat{v}$	1	Unit vector in direction from the center of the Earth to the satellite
v_t	ms^{-1}	Tangential velocity of the satellite
x	1	Argument of Bessel function depending on θ_o
x_0	1	x-component of O
y_0	1	y-component of O

1

Chapter 1.

Introduction

On February 10 in 2009 the Russian derelict military satellite Kosmos 2251 collided with the American communication satellite Iridium 33 [3]. The collision, which produced 1,832 newly cataloged fragments, is not an isolated incident and further contributes to the growing risk of space debris for satellite missions, particularly at altitudes above 800 km [3]. With the increasing number of objects in orbit space surveillance systems are forced to respond accordingly. Even though Satellite Laser Ranging (SLR) systems are not traditionally used for this purpose, these systems could contribute to the growing demand for collision avoidance systems [4].

Around 40 SLR stations are used in a world-wide network called International Laser Ranging Service (ILRS). Currently several stations are reaching their limits in terms of tracking requests [5]. The Institute of Technical Physics from the German Aerospace Center (Deutsches Zentrum für Luft- und Raumfahrt (DLR)) in Stuttgart develops laser systems for a wide range of applications. One of their long-standing experiences falls within the realm of SLR. Alongside development of passive optical systems, it has already developed a cost-effective SLR system called miniSLR® [5].

Since the beginning of satellite laser ranging, retroreflectors have been used to increase the Optical Cross Section (OCS) due to the limited power of the available laser systems [6] [7, p. 302 f.]. The use of common retroreflectors will require a non-negligible amount of volume occupying space on the exterior of the satellite, which can stay in conflict with dispenser systems [1]. Further developments successfully demonstrated SLR without passive optical amplification by detecting space debris [8]. However, these systems require a higher laser power, which significantly increases the costs of implementation.

Thus, the use of SLR for satellite operators, both with and without passive optics, imposes certain requirements. Since D. Hampf et al. [5] not only recommend equipping more satellites with retroreflectors but also to implement a standardized installation, alternatives that offer simpler and more flexible integration could make the actual use of SLR more attractive.

One alternative could be the use of retroreflective foils, which have so far only been used in the field of traffic to enhance visibility, but offer many advantages compared to established retroreflectors operating in space. Foils can be flexible implemented, are ultra-light, and are low-cost in addition. P. Sauer et al. [2] also emphasizes the advantages of using retroreflective foils but has only ranged them in ground-based experiments over relatively short distances.

The main disadvantage lies in the lower OCS, which depends on the properties of the respective embedded Corner Cube Reflectors (CCRs), including the material, the coating, the dihedral offset angle, and the aperture size. These properties can largely be derived from the diffraction behavior, specifically the Far-Field Diffraction Pattern (FFDP), which will be investigated in detail in this study.

From these investigations, adjustments necessary to apply the state-of-the-art calculation of the OCS, as utilized by J. Degnan [9], are derived for retroreflective foils. For this calculation, various assumptions must be made regarding both the structure and the diffraction behavior. Therefore, different commercially available foils are initially analyzed experimentally. In addition, ray tracing simulations will support the experimental data by providing a deeper insight into the diffraction behavior in relation to the microscopic structure. According to the obtained assumptions, this study presents the OCS of retroreflected foils as a function of the embedded diameter, the reflectivity, and utilized area. In addition, the required area and diameter will be calculated as a function of a given OCS. Finally, the calculation of link budgets in accordance with the specification of the miniSLR® will be presented.

2

Chapter 2.

Theoretical Background

For the analysis of this study an understanding of the principle of diffraction theory is necessary. Alongside the *Kirchhoff diffraction integral* and the Fraunhofer assumptions, the FFDP of a circular aperture will be described analytically and the array theorem will be examined. Afterward, the key areas of this study, including retroreflection, satellite laser ranging and the link budget equation, are explained. Finally, the background on structural designs of retroreflective foils is presented, followed by an introduction of the simulation software and the microscopic system used in this study.

2.1. Fraunhofer Diffraction

If a monochromatic spherical wave, which can be written as

$$U(r) = \frac{A\, e^{-ikr}}{r} \tag{2.1}$$

is traveling from the point source P_0 trough an aperture as seen in Figure 2.1, the *Kirchhoff diffraction integral* is defined by

$$U_P = -\frac{iA}{2\lambda} \iint_{\mathcal{A}} \frac{e^{ik\,(r+s)}}{rs} \left[\cos(n_s, r) - \cos(n_s, s)\right] dS. \tag{2.2}$$

U_P describes the complex amplitude in point P resulting through the surface integral over the aperture surface $\mathcal{A}$. The complex amplitude A depends on r and s which are the traveled distances from point P_0 and Q, whereby n_s presents the normal of the integral surface element dS. The wavenumber k and the wavelength λ characterizes the wave.

The *Kirchhoff diffraction integral* is further based on the assumption of the Huygens-Fresnel principle.[1] The diffracted wave in the field point P can be calculated by the integral of the transmitted waves through the aperture. [10, S.421ff.] [11, p.1009 ff.] [12, p.44ff.] [13, p.314] [14, p.289ff.] [15, p.69]

---

[1] For detailed information about this principle, M. Born et al. [10, 413ff.] is recommended.

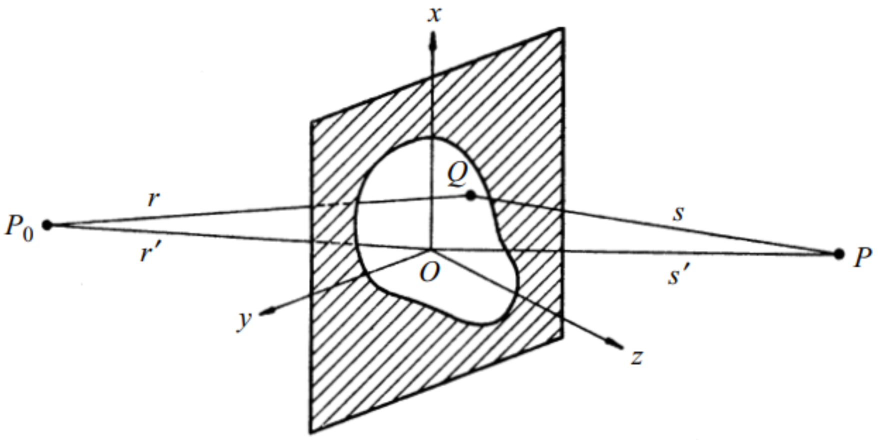

Figure 2.1.: Diffraction at an aperture in a plane screen [10, p.425]

This study is just interested in the diffraction of far fields. Therefore, the following assumptions will simplify the integral.
First of all, the distances P_0O and OP are assumed to be very large compared to the dimension of the aperture. By using (x_0, y_0, z_0) for the origin of the coordinate system and ξ and η for the shifted coordinates of Q laying in the aperture, the so-called *Fraunhofer conditions* leads to

$$|r'| \gg \frac{(\xi^2 + \eta^2)_{max}}{\lambda}, \tag{2.3a}$$

$$|s'| \gg \frac{(\xi^2 + \eta^2)_{max}}{\lambda}. \tag{2.3b}$$

For the next step of approximation r and s are expressed in terms of r' and s' using a Taylor expansion by neglecting higher-order terms. Additionally, a paraxial approximation is used so that the diffraction angle must be small to the optical axis. The resulting incident wave has a plane wave front, so that the amplitude and phase is constant over the aperture. The Kirchhoff diffraction integral then can be written by

$$U_P = C \iint_{\mathcal{A}} e^{ikf(\xi,\eta)}\, d\eta d\xi, \tag{2.4}$$

in accordance to

$$f(\xi, \eta) = -\frac{\xi x_0 + eta\, y_0}{r'}. \tag{2.5}$$

This is known as the Fraunhofer approximation. C is defined in terms of quantities depending on the position of the source and of the point of observation. [10, p.426f.] [11, p.924 ff.] [12, p. 51ff.] [13, p.315] [14, p. 297 ff.] [15, p. 70ff.] [16, p. 459ff.]

2.1.1. Fourier-Optics

The constant C before the integral from Equation 2.4 specifies only the amplitude and phase of the wave in the aperture in Point Q or rather in P. For a discussion about the relative distribution of the amplitude these terms are not necessary. The distribution of the amplitude and phase in the aperture can also be written by the aperture function

$$\mathcal{A}(\xi, \eta) = \mathcal{A}_0(\xi, \eta) e^{i\phi(\xi,\eta)}. \tag{2.6}$$

From Equation 2.5 we can define the spatial frequencies $k_x = \frac{x_0}{r'}$ and $k_y = \frac{y_0}{r'}$, and replace these with the phase component of the aperture function. Thus, the Fraunhofer diffraction integral can be expressed as

$$U_P = \iint_{-\infty}^{\infty} \mathcal{A}(\xi, \eta) e^{-ik_x\text{-}ik_y} \, d\eta d\xi, \tag{2.7}$$

which means that the distribution of amplitude in the FFDP is equal to the Fourier transform of the aperture function. [10, p. 428ff.] [11, p. 1077ff.] [12, p. 55f.] [13, p. 318] [14, p. 302f.] [16, p. 732ff.]

2.1.2. Airy Disk

The most common and for this study very important two-dimensional Fraunhofer diffraction pattern is caused by a circular aperture, which is illustrated in Figure 2.2. The intensity is radial distributed and can be described by

$$I_{circ}(\theta) = \left(\frac{2J_1(kr_{circ} \sin(\theta))}{kr_{circ} \sin(\theta)} \right)^2, \tag{2.8}$$

where J_1 is the Bessel function of the first kind of order one, evaluated over the radius r_{circ} of the aperture and the diffraction angle θ measured along the optical axis. Equation 2.8 is also called the *Airy function.* [10, S.439 ff] [11, S.929 ff.] [12, S. 60] [13, p.307] [14, p. 329ff.] [15, S.106] [16, p. 468 ff.] [17]

The size of the central maximum can be approximately calculated by [10, p. 442] [11, p. 935] [14, p. 390] [16, p. 466] [18]

$$\theta_{circ_{min,\,0}} \approx 0.61 \frac{\lambda}{r_{circ}}. \tag{2.9}$$

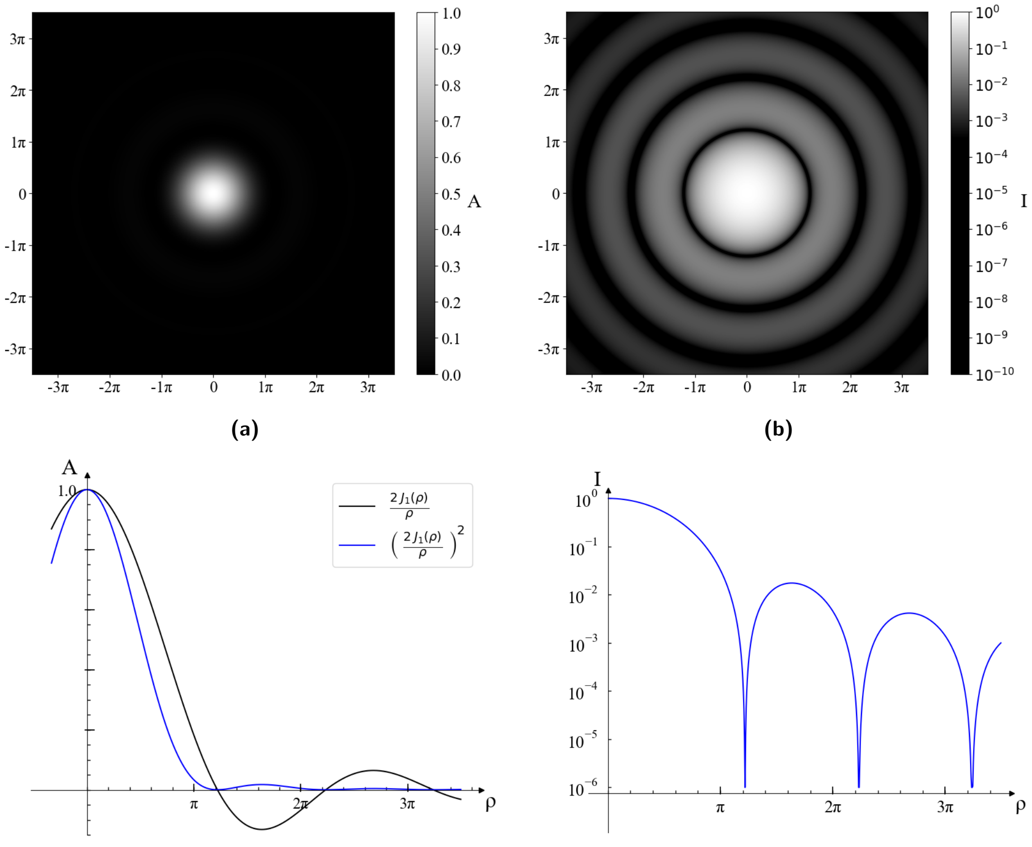

(a) (b)

(c) (d)

Figure 2.2.: Theoretical FFDP of a perfect circular aperture under Fraunhofer conditions. The argument of the Bessel function J_1 is reduced to ρ, representing the wavenumber and the diameter of the aperture according to Equation 2.8. The heatmaps describe the amplitude (a) and intensity (b) distribution. In addition, the radial distributions (c) and (d) are shown in the plots below.

2.1.3. Array Theorem

A theoretical estimation of Fraunhofer diffraction is required not only for a single aperture but also for an array of apertures. Therefore, the intensity and the FFDP will be discussed. D. Arnold [15, p. 117] shows an analytical derivation based on the Rayleigh-distribution for calculating the intensity of an array of CCRs[2]. The intensity is n_{ccr} times one retroreflector, where n_{ccr} is the number of CCRs in the array. Also M. Born et al. [10, S. 445] showed that a regular distribution of n identical apertures creates a diffraction pattern with an intensity n times one aperture. Both assume a large number n. In D. Arnold [15, p. 118] a guideline can be found, by which the number is related to the deviation from the assumed Poisson distribution. For $n = 10$ the difference is only 5 %.

As already shown the FFDP can be understood as the Fourier transform of the aperture function. The intensity distribution of an array of apertures can be derived from the array theorem, which states that the overall FFDP is generated by the superposition of the individual apertures. In this context, the FFDP of the individual aperture corresponds to the envelope, while the arrangement of the apertures corresponds to the carrier frequency. In other words, the Fourier transform of a periodical orientation of identical apertures will be equal to the Fourier transform of a single aperture function multiplied by the arrangement of the array which can be expressed as a point source distribution. [11, p. 1084] [10, s. 446 ff.] [15, p. 73 ff.] [14, p. 306ff.]
The individual retroreflectors embedded in the array can also be considered as emitters. J. Kästel et al. [19] shows the formation of a central maximum by an array of coherent laser sources as a function of the fill factor of the array. At a minimal distance between each source, a distinct central maximum form and is rapidly shrinking by reducing the fill factor. In A. Brown [20, p. 28], the same principle is illustrated using antenna arrays.

The formation of the overall pattern is not only a function of the relative positions of neighboring elements, but also, to return to the topic of retroreflection, on the phase relationship in the incident or rather retroreflected waves. The array theorem assumes periodical orientated and identical apertures, which thus generate the same phase shift. Regarding this, it must be assumed that the foils exhibit no manufacturing tolerances and are perfectly aligned. In addition, the angle of incident must be orientated normally to the face, avoiding path differences. This case is referred to as the so-called *coherent return* and is realistically feasible. The tolerances could be kept sufficiently small, but as seen further in this study, tolerances already in fractions of the corresponding wavelength will make a huge difference in the FFDP. Additionally, the angle of incidence is only normal to the face in the rarest instances.[3] [15, p. 132 ff.]
The so-called *incoherent return* represents a significantly more realistic scenario. However, two cases must be distinguished in this context. In the case of a wave incident at a non-normal angle, the resulting phase shift can be described using a gradient. This is equivalent to methods used in active electronically scanned arrays. Figure 2.3 illustrates the radial distribution of the electric field generated by a one-dimensional antenna array. In accordance with the array theorem, the Element Factor (EF) corresponds to the individual aperture, while the Array Function (AF) pertains to the arrangement of the array. As can be seen, a gradual phase shift in the array leads to a radial displacement of the central

---

2 A retroreflector acts like an aperture which will be discussed in the following section

3 Imagine a spinning satellite orbiting above the celestial sphere

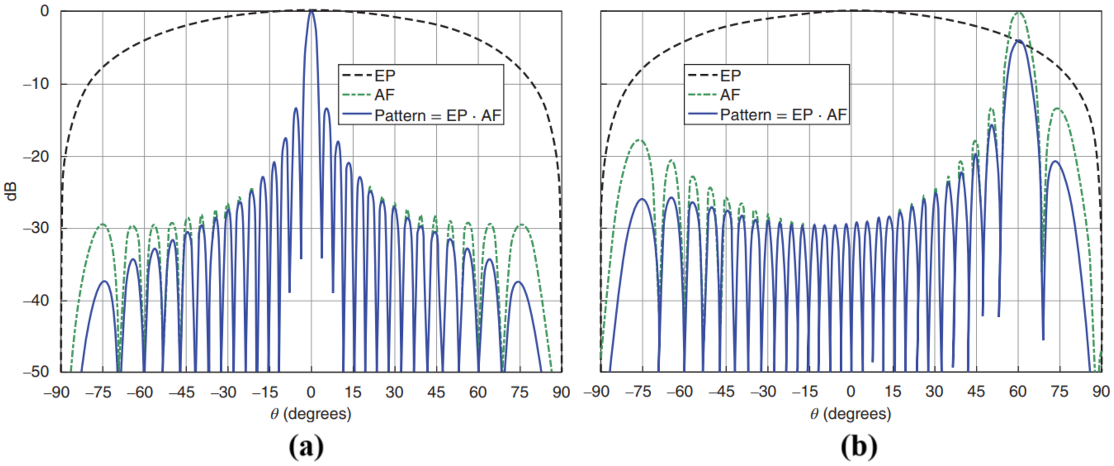

Figure 2.3.: Electric field distribution of a linear array pattern with 30 elements scanned to $\theta = 0\,^\circ$ (a) and $\theta = 60\,^\circ$ (b). [20, p. 35]

maximum. [21, p. 285 ff.] [22, p. 278ff.]

The situation should differ when implementing manufacturing tolerances. Here, the phase shift should depend on the tolerance error of each individual CCR, resulting in a random distribution within a certain range. J. Kästel et al. [19] and A. Brown [20, p. 31] demonstrate that the central maximum decreases in intensity and broadens as the phase error increases. In general, the interference conditions are no longer precisely satisfied, resulting in a blurring of the FFDP.

When using arrays of CCRs, it is generally assumed that the FFDPs of the individual CCRs interfere with each other, producing a central maximum of the same size as that of a single CCR. The different distances to the center of each individual CCR can be neglected by just adding all intensities together. [15, p. 149] [23] [24, p. 11]

Nevertheless, this study will examine the three coherence cases in greater detail which will not only provide a deeper understanding of the array theorem, but will also need to explain the diffraction phenomena observed in the experiment. This consistent relation will provide the physical foundation necessary to make the required adjustments in the calculation of the OCS.

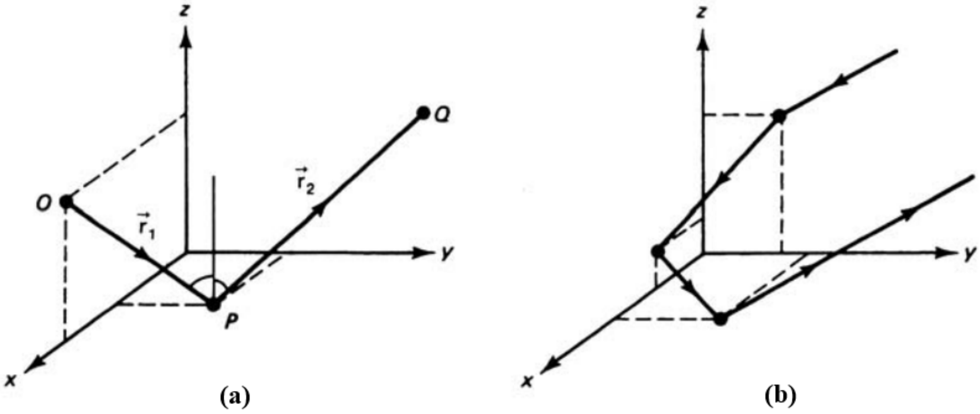

Figure 2.4.: Principle of specular reflection (a) and retroreflecting (b) realized by three mutually orthogonal surfaces. [16, p. 75]

2.2. Corner Cube Reflector

Optical reflection for engineering applications can be classified into three types: specular, diffuse and retroreflection [25]. This study will focus on the last one, which can be achieved by using corner cube or microsphere retroreflectors, where a CCR shows larger radiance, but therefore microspheres have a higher divergence. Both types can be metal coated in addition. [26]

CCRs are either made hollow or solid. The surface of solid CCRs can be bare or metal-coated, whereby reflections of bare rely on Total Internal Reflection (TIR). The coated CCRs show less reflectance at normal incidence but are therefore less effective at increasing incidence angles. [27]

The central difference between coated and uncoated CCRs lies in the behavior of polarization, where uncoated CCRs exhibit significant polarization effects, leading to losses in the return signal, whereas coated CCRs show almost no effects. [28]

Figure 2.4 illustrates the law of reflection at plane mirrors. In (a) the incident ray $\vec{r}_1 = (x, y, z)$ is reflected by hitting the xy-plane. The resulting ray becomes $\vec{r}_2 = (x, y, -z)$. In general, the component of a ray polarized perpendicular to the plane of incidence gets inverted. If three planes were positioned orthogonal to each other, a ray would reflect its source. [11, p.199ff.] [10, Kapitel3] [16, p.73 ff.] [18] [29]

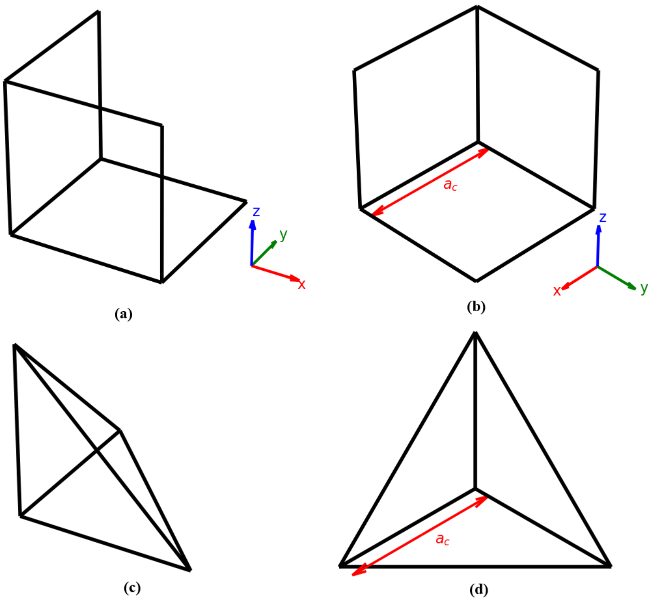

(a) (b) (c) (d)

Figure 2.5.: Visualization of a hexagonal (a), (b) and triangular CCR (c), (d), where (b) and (d) is oriented perpendicular to the face including the hexagonal output shape of the hexagonal CCR. For further visualizations B. Park et al. [28] and E. Brinksmeier [29] [30] are recommended.

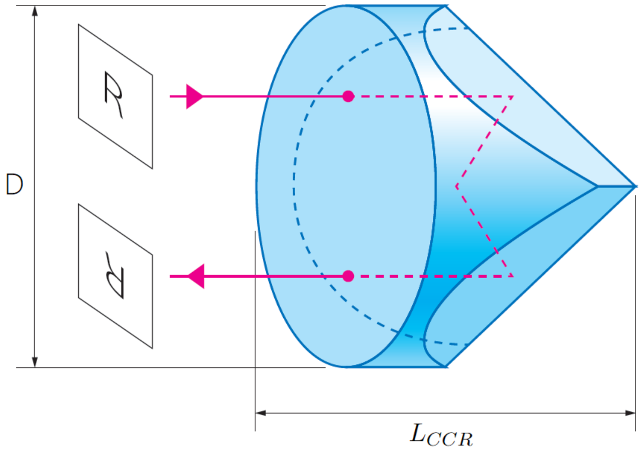

Figure 2.6.: Visualization of a circular CCR with a diameter D and the characteristic length L_{ccr}. [31]

There are three common types of a CCR, where the face or rather the protection plane determines the name. Figure 2.5 shows CCRs with a triangular and a hexagonal face. The mutually planes are triangles and rectangles. The hexagonal shape is only seen from the normal of incidence. [27] [30]

A cylindrical CCR is constructed by modifying a triangular CCR through the addition of a cylindrical cut and shown in Figure 2.6. These types are commonly used for SLR systems. [15, S. 9 ff.]

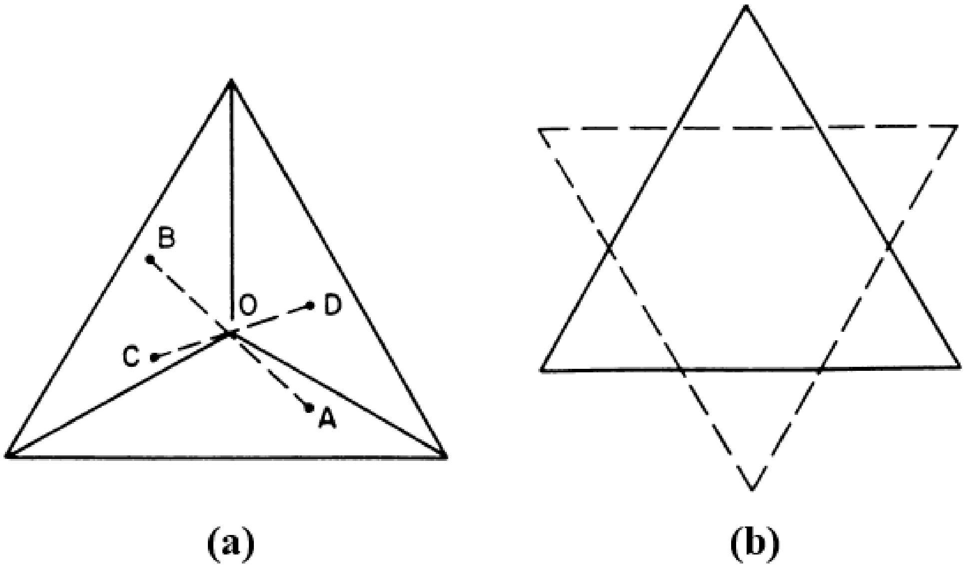

Figure 2.7.: In- (a) and output aperture (b) of a triangular CCR. [15, p. 9]

Further a CCR can be divided into an input and output aperture. The input aperture is the shape which the incident rays see. The output aperture is formed by the effective area, the part of the input aperture which is retroreflected. The effective area depends on the type of CCR and the angle of incidence. H. Eckhardt [18] presents a determination of the effective aperture for the three different CCR configurations discussed in this study. It also addresses the influence of the refractive index. In addition, H. Kim et al. [25] provides a more analytical description. Plots for the effective aperture as function of the incidence angle were also given in E. Brinksmeier et al. [29] [30].

Figure 2.7 illustrates the retroflected area for a triangular CCR. The output aperture is partly outside of the input aperture, so that only the overlapping parts resulting in retroreflection. For a perfect triangular CCR the output aperture is a hexagon, whereby approximately 66 % of the incidence light normal to the face is retroreflected.

For a hexagonal and a circular CCR, the input and output aperture is fully overlapped, so that 100 % is retroreflected. [29]

If the phase and amplitude is constant over the face, a retroreflector acts like a simple aperture. This means that both a triangular CCR and a hexagonal CCR act like a hexagonal aperture. A circular CCR acts like a circular aperture[4]. [15, p. 9-11, p. 29-50, p. 89]

---

[4] In R. Chang et al. [32] you can find a analytical description

2.3. Satellite Laser Ranging

The first successfully ranging experiment was reported in 1964, where a NASA team tracked the satellite Explorer 22 with an accuracy of 3 meters. Since then, higher accuracy was developed to provide an analysis of geodetic, tectonic and altimetry data. Today SLR is used in a comprehensive field of applications. Knowing the accurate position of satellites allows for the study of various types of disturbances, like earth gravity field structure or atmospheric drag. It is also used for space oceanographic and plate tectonic motion. For all these kinds of research geodetic satellites are used. The spherical surfaces of these objects are equipped with retroreflectors to improve an accuracy of 1-2 cm, which makes them the currently most accurate available system for detecting of objects in space. [6] [7, p. 302 f.]

SLR is based on Time-of-Flight (TOF) measurements of light. Therefore, a satellite with a high OCS (with a CCR or an array of CCRs) is tracked by an optical telescope. Co-aligned laser pulses trigger a start counter, whereby a sensitive light detector behind the telescope stops it again if the reflected pulse is registered. 60 years of development imposed limitations by laser pulse width, detector, risetime and stability, epoch timing accuracy and atmospheric propagation modeling. An important element of this science is the link budget equation, which will be discussed in the following section. It gives an accurate estimation of the amount of successfully returned photons that can be registered by the detector. [6] [7, p. 304]

2.4. Link Budget Equation

As mentioned before, one of the objectives of this study is to provide a comprehensive analysis of the OCS and a calculation of the link budget. This section will provide an overview of these calculations, where the listed equations were taken from J. Degnan [9] unless explicitly referenced. The radar link equation is written by

$$N_{pe} = N_t \cdot G_t \cdot \left(\frac{1}{4\pi R^2}\right)^2 \cdot \sigma \cdot A_r \cdot \tau_r \cdot \tau_t \cdot \eta_q \cdot \tau_{filter} \cdot \tau_{atm}^2 \cdot \tau_c^2. \tag{2.10}$$

The equation calculates the mean number of photons, N_{pe}, recorded by the ranging detector per laser pulse. In this context, N_t represents the total number of photons emitted per laser pulse, while G_t denotes the gain of the transmitter. The slant range between the transmitter and the target is given by R, and σ corresponds to the OCS of the target. The receiver aperture is represented by A_r. Additionally, τ_r and τ_t denote the transmission efficiencies of the receiver and transmitter, respectively. The term η_q refers to the quantum efficiency of the detector. The transmission through the optical filter is represented by τ_{filter} and τ_{atm} accounts for the atmospheric transmission. Further atmospheric losses result from the presence of cirrus clouds, which is presented by τ_c. [15, p. 146]

In the following, each of the terms in Equation 2.10 are examined in detail. First, the number of transmitted photons N_t can be calculated by

$$N_t = \frac{E_p \cdot \lambda}{h \cdot c}, \tag{2.11}$$

where E_p is the pulse energy and λ the wavelength of the laser. h and c are the Planck constant and the speed of light in vacuum.

The transmitter gain is assumed as a gaussian beam and can be written by

$$G_t = \frac{8}{\theta_d^2} \cdot exp \left[-2 \left(\frac{\Delta\theta_p}{\theta_d} \right)^2 \right]. \tag{2.12}$$

The far field divergence half angle θ_d is the angle between the beam center and the 1/e^2 intensity point. $\Delta\theta_p$ is the beam pointing error.

The slant range R is given by

$$\begin{gathered} R = -(R_E + h_{station}) \cdot \cos\left(\frac{\pi}{2} - \alpha_e\right) \\ + \sqrt{\left[(R_E + h_{station}) \cdot \cos\left(\frac{\pi}{2} - \alpha_e\right)\right]^2 + 2R_E(h_{sat} - h_{station}) + h_{sat}^2 - h_{station}^2}, \end{gathered} \tag{2.13}$$

where R_E is the earth radius. $h_{station}$ and h_{sat} give the altitude of the station and the satellite above sea level. The elevation angle α_e lies between the horizontal plane and the laser beam.

A_r describes the effective area of the receiving aperture and can be calculated by

$$A_r = \frac{\pi}{4} \cdot D_r^2 \cdot (1 - \eta_{obs}), \tag{2.14}$$

where D_r is the diameter of the receiving system and η_{obs} the obscuration due to the secondary mirror.

Fixed values are assumed for the transmission coefficients τ_r, τ_t, and τ_{filter}, based on the specifications of the SLR station in use. τ_c can be set to 0.8.
The transmission efficiency of the atmosphere is subject to a rather complex relationship, which can also be found in M. Naboulsi et al. [33]. Clear weather conditions will lead to $\tau_{atm} = 0.39$.

2.4.1. Optical Cross Section

The OCS gives the amount of light which is reflected to its source. J. Degnan [9] derivates the OCS of a retroreflector under the Fraunhofer conditions. This complex quantity is built out of the retroreflector properties, including the material, the coating, the dihedral angle offset and the aperture size.

Peak cross section

As already mentioned, a retroreflector reflects light back to its source, independent of the angle of incidence. Nevertheless, the incidence influences the shape of the input aperture of the CCR and therefore the far field diffraction pattern and the OCS.
The greatest value is achieved if the CCR is oriented normally to the incident light. The so-called peak cross section can be written by

$$\sigma_0 = \rho_{ccr}\, A_{ccr} \left(\frac{4\pi}{\Omega}\right) = \rho_{ccr} \left(\frac{4\pi A_{ccr}^2}{\lambda^2}\right), \tag{2.15}$$

where the area A_{ccr} and the reflectivity ρ_{ccr} depend on the type of CCR. $\frac{4\pi}{\Omega}$ is the on-axis retroreflector gain, whereby Ω is the effective solid angle occupied by the FFDP of the CCR. For a circular CCR with a diameter D_{circ} the peak cross section can further be evaluated by

$$\sigma_{0,\,circ} = \frac{\pi^3}{4\lambda^2}\, \rho_{circ}\, D_{circ}^4. \tag{2.16}$$

Velocity Aberration

Additionally, the velocity of the satellite must be taken into the account. If the satellite does not move, the light would be traveling back to its point of source. However a relative velocity between the station and the satellite causes an angular deflection from the station, which is called *velocity aberration* and can be written as

$$\alpha(h_{sat}, \theta_{zen}, \omega) = \frac{2}{c}\sqrt{\frac{R_E^2 \cdot g}{R_E + h_{sat}}} \cdot \sqrt{\cos^2(\omega) + \Gamma^2(h_{sat}, \theta_{zen}) \cdot \sin^2(\omega)}. \tag{2.17}$$

θ_{zen} is the angle between the beam and the zenith and therefore the complementary angle of α_e. The quantity $\Gamma^2(h_{sat}, \theta_{zen})$ is defined by

$$\Gamma^2(h_{\text{sat}}, \theta_{\text{zen}}) = 1 - \left(\frac{R_E \cdot \sin(\theta_{\text{zen}})}{R_E + h_{\text{sat}}}\right)^2 < 1. \tag{2.18}$$

ω refers to the satellite movement and can be written as

$$\omega = \arccos\left[(\hat{s} \times \hat{r}) \cdot \hat{v}\right], \tag{2.19}$$

where the unit vectors $\hat{s}$, $\hat{r}$ and $\hat{v}$ represent the direction from the center of the Earth to the satellite, from the SLR station to the satellite and from the satellite's movement in space. For the calculations $\hat{r}$ must be expressed in components. A detailed examination is attached in Section A.1.

The extreme values of α can be written by

$$\alpha_{\max}(h_{\text{sat}}) = \alpha(h_{\text{sat}}, \theta_{\text{zen}}, \omega = 0) = \frac{2}{c}\sqrt{\frac{R_E^2 \cdot g}{R_E + h_{sat}}}, \tag{2.20a}$$

$$\alpha_{\min}(h_{\text{sat}}, \theta_{\text{zen}}) = \alpha(h_{\text{sat}}, \theta_{\text{zen}}, \omega = \frac{\pi}{2}) = \frac{2}{c}\sqrt{\frac{R_E^2 \cdot g}{R_E + h_{sat}}} \cdot \Gamma(h_{\text{sat}}, \theta_{\text{zen}}), \tag{2.20b}$$

where g is the acceleration due to Earth's gravity. Figure 2.8 shows the velocity aberration as a function of the orbital altitude, where the established minimum and maximum values for the elevation angle were used.

In accordance with Section 2.2 it can be assumed that a CCR acts like an aperture under Fraunhofer conditions, so that the Airy function (cf. Section 2.1.2) can be used to determine

$$\sigma(\theta_o) = \sigma_0 \left[\frac{2J_1(x(\theta_o))}{x(\theta_o)}\right]^2, \tag{2.21}$$

where the argument $x(\theta_o)$ is calculated by

$$x(\theta_o) = \frac{\pi D_{circ}}{\lambda} \sin(\theta_o). \tag{2.22}$$

θ_o is defined as the off-axis angle and is determined by the velocity aberration, if no additional disturbances occurs. Equations 2.21 and 2.22 are only valid for a circular CCR. In accordance with that a CCR with a large diameter has a small-angle FFDP. As a consequence, a small diameter causes a large-angle FFDP. The diameter of the embedded CCRs in the foils examined in this study is significantly smaller than that of commonly used CCRs, resulting in a much smaller OCS that is less sensitive to the effects of velocity aberration.

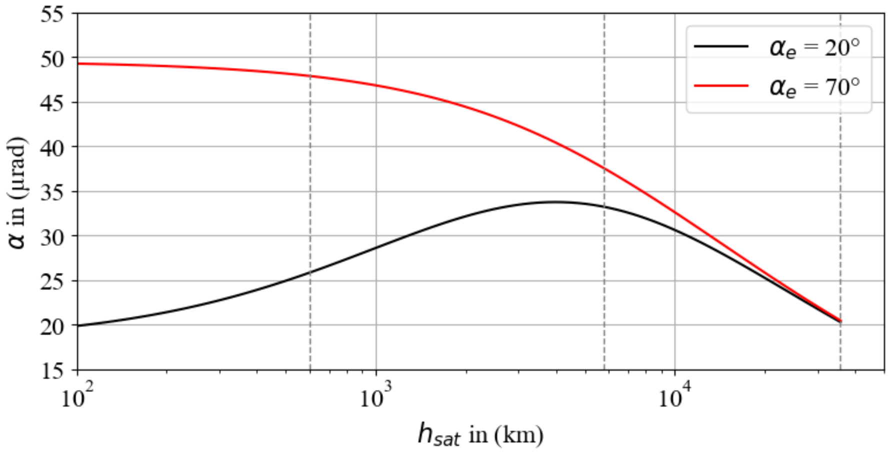

Figure 2.8.: Velocity aberration α as a function of the orbital altitude h_{sat}, whereby the elevation angles $\alpha_e = 20°$ and $\alpha_e = 70°$ determine the limit of the ranging angle.

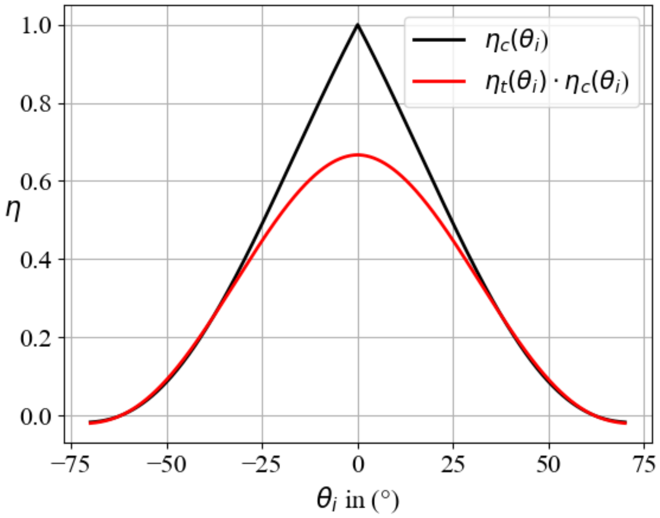

Figure 2.9.: Reducing factors for different types of CCRs. $\eta_c(\theta_i)$ is defined for circular and hexagonal CCRs, shown in black. The effective area of a triangular CCR is additionally reduced by $\eta_t(\theta_i)$ defined in Equation 2.29, resulting in the read curve. All reducing factors are calculated for $n_{ref} = 1.45$.

Effective Area

As already mentioned, the effective Area of a CCR depends on the incident angle θ_i. It is reduced by the factor $\eta(\theta_i)$ and for a circular CCR given by

$$\eta_c(\theta_i) = \frac{2}{\pi}\left[\arcsin(\mu) - \sqrt{2}\mu\tan(\theta_i')\right]\cos(\theta_i), \tag{2.23}$$

where θ_i' is the propagation angle inside the CCR and μ the normalized reduced aperture radius along the tilt direction.
It can be written by

$$\theta_i' = \arcsin\left(\frac{\sin(\theta_i)}{n_{ref}}\right) \tag{2.24}$$

and

$$\mu = \sqrt{1 - \tan(\theta_i')^2}, \tag{2.25}$$

where n_{ref} is the refractive index of the material from which the CCR is manufactured. In accordance to Equation 2.15 the area of a circular CCR A_{circ} can be adjusted by the reducing factor, so that the OCS is written as

$$\sigma(\theta_i) = \eta_c^2(\theta_i) \cdot \sigma_0. \tag{2.26}$$

With the adapted peak cross section as a function of the incidence angle the FFDP from Equation 2.21 can be written by

$$\sigma(\theta_o, \theta_i) = \eta_c^2(\theta_i)\,\sigma_0\left[\frac{2J_1(x(\theta_i,\theta_o))}{x(\theta_i,\theta_o)}\right]^2, \tag{2.27}$$

whereby D_{circ} from Equation 2.22 is also reduced by η_c and given by

$$x(\theta_i, \theta_o) = \frac{\pi \, D_{circ} \, \eta_c(\theta_i)}{\lambda} \sin(\theta_o). \tag{2.28}$$

In addition the reducing factor from Equation 2.23 is plotted in Figure 2.9, which also includes a fitted function to determine a reduction factor for a triangular CCR in accordance with H. Eckhardt [18] and given by

$$\eta_t = \frac{2}{3} \cdot (2 - 0.35^{\theta_i}). \tag{2.29}$$

Since the curves of the effective areas of a hexagonal and a circular CCR closely match, both will use Equation 2.23.

Maximum Angle of Incidence

As seen before the effective area of a CCR decreases by an increase of the incidence angle. Building on this, a cut-off angle θ_c can be defined beyond which retroreflection no longer occurs. For a circular CCR it is defined by

$$\theta_c = \arcsin\left(n_{ref} \sin\left(\arctan\left(\frac{D_{\mathrm{ccr}}}{2L_{\mathrm{ccr}}} \right) \right) \right), \tag{2.30}$$

where L_{ccr} is given by the manufacture [15, p. 29]. The length of a triangular and a hexagonal CCR will be adapted in Chapter 5.

Mean Optical Cross Section

In accordance with the velocity aberration and the effective area, the total cross section is a function of the relative position (incidence angle) and velocity from the satellite to the station. These values vary across the celestial sphere, so to obtain a meaningful estimation for the link budget, an average is calculated. The off-axis angle can be determined from the extreme values of the velocity aberration. The OCS is defined by

$$\sigma = \frac{1}{|\theta_o|} \frac{1}{|\theta_i|} \left(\sum_{\theta_o} \sum_{\theta_i} \sigma(\theta_o, \theta_i) \right), \tag{2.31}$$

for an angle range of

$$\theta_o \in [\alpha_{min}, \alpha_{max}] \tag{2.32a}$$

$$\theta_i \in [0, \theta_c], \tag{2.32b}$$

The numbers for the angle ranges are set to $|\theta_o| = 300$ and $|\theta_i| = 100$.

2.4.2. Rate of Detection

Since SLR involves a discrete distribution of events, by simply calculating the successful responses over a period, the Poisson distribution can be used to determine the expected outcomes. By assuming a detection threshold N_{tr} the probability of detection can be written by

$$P_d(N_{pe}, N_{tr}, k_n) = 1 - e^{-N_{pe}} \sum_{k_n=0}^{N_{tr}-1} \frac{N_{pe}^{k_n}}{k_n!}, \qquad (2.33)$$

where k_n refers to the number of occurrences. This study will focus on the link budget calculation for single photon mode. Thus, the equation simplifies with $N_{tr} = 1$ to

$$P_d(N_{pe}) = 1 - e^{-N_{pe}}. \qquad (2.34)$$

2.5. The miniSLR® System

Alongside geodetic studies SLR is already used for space traffic management. The demand for obtaining centimeter-precise orbit information during and after missions is very high. Many stations reach their limits in terms of number of tracked satellites while the number of satellites in Low Earth Orbit (LEO) is massively growing. Generally, SLR stations require on own buildings with an observatory dome and adjacent laboratory rooms. For further expansion of the ILRS network the DLR developed a small and inexpensive SLR system, called miniSLR®. However, if a less powerful laser system is used, an increase in the OCS of targets by retroreflectors is necessary. The fully sealed and weather proofed system measures 2 m × 2 m × 1.5 m. [5]
The calculation of the link budget in this study will based on the specifications of this system, listed in Table B.1.

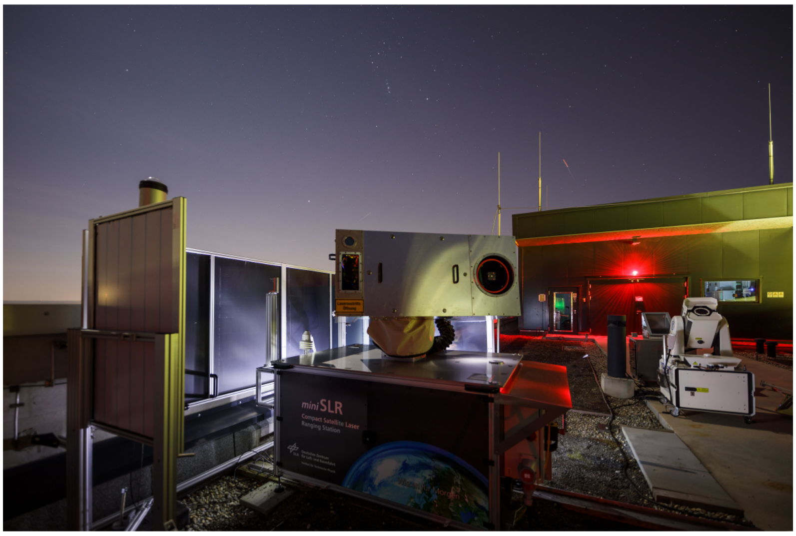

Figure 2.10.: View of the miniSLR® system, placed on the roof of the DLR in Stuttgart, Germany. (Photo: Paul Wagner / DLR)

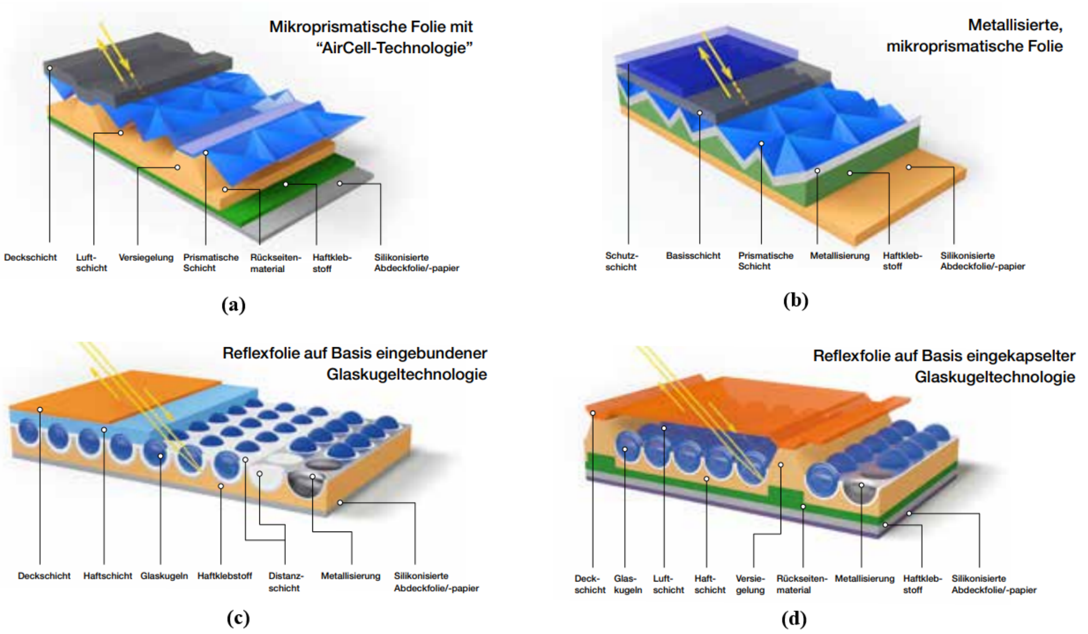

Figure 2.11.: Principles of constructing different types of retroreflectors. (c) and (d) present microspheres, while (a) show uncoated and (b) coated CCRs [31].

2.6. Retroreflective Foils

The principle of retroreflection is used in numerous applications. In the field of radar systems, tracking objects are equipped with retroreflectors to increase the return signal. Range finding and modulation devices in optical communication systems are additional typical applications. The most used area is in traffic, where retroreflective foils are specifically employed to enhance visibility for bicycles and clothing. [27] [29] [26] [30]

Retroreflective foils can be constructed by either using microspheres or CCRs [29]. This study will focus on CCRs. Triple mirrors are preferred in measurement applications, as a smaller amount of light is lost due to scattering effects [27]. There are three standard methods of building retroreflective foils, the direct cutting, also called fly-cutting, pin building and laminating techniques. In addition, gray shade lithography and micro-EDM can be used, but provide less optical quality. Over ten years ago the three standard methods were determining the minimum manufacturing limit for the diameter of the CCRs embedded in the foils, which were at around 500 µm. Since then, diamond micro chiseling was developed for downscaling the structure size with realistic production times. [30] [29]

E. Brinksmeier et al. [29] showed that the minimal prism size is 40 µm, 50 times the wavelength of visible light. Otherwise, diffractive light modulation will increase and deteriorate the reflectance. In addition, a roughness of 10 µm is recommended.

Figure 2.11 shows the discussed types of retroreflectors. The foils researched in this study will use (a) and (b).

2.7. Ansys Zemax OpticStudio

OpticStudio is a comprehensive design software widely used for simulating optical systems. It supports both simple lens systems and complex optical setups involving scattering, diffraction, and stray light analysis. The software will be used for the calculation of the diffraction phenomena, discussed above.

OpticStudio is separated into two different modes, the sequential and the non-sequential mode. The first one uses iterative ray tracing algorithms from surface to surface in a strict sequence, while the non-sequential mode represents a more actual way of physics. Here the rays can hit objects and surfaces which may not be in sequential order. In non-sequential mode 3D solid objects can also be modeled to build more complex optical systems. The software also supports a mixed mode. As further seen, this will be very helpful for this study. [34, p. 498 ff.]

For the calculation of the FFDPs the Point Spread Function (PSF) will be used. The software provides two different calculation algorithms, PSF Fast Fourier Transformation (FFT) and the Huygens PSF. In the FFT, the signal or rather the wave fronts are transformed in the frequency domain to calculate the PSF. Huygens PSF models waves using a discrete field, where each element represents a point source. The diffraction pattern of each point source is calculated by integral over the wavelets.
Therefore the FFT PSF is based on Equation 2.7, Huygens PSF on Equation 2.4.

2.8. Differential Interference Contrast Microscopy

This study will use the Differential Interference Contrast (DIC) microscope to measure the diameter of the CCRs embedded in the retroreflective foils. Besides its common application in biology, it is also used in material science capable of producing pseudo three dimensional images without the need of probe preparation. Therefore, a short overview of the physical examination of the microscope's mechanism is presented in this section.
The method of DIC is based on phase contrast observation, whereby the phase variations of two mutually coherent wave fronts illuminating a specimen are converted into an intensity distribution using interference methods. A plane polarized beam is split into two orthogonally polarized, mutually coherent components by a Normaski prism. The prism creates an internal differential displacement of a few tenths of a micrometer, so that the specimen is illuminated in two different points. The resulting phase shift is analyzed after another Normaski prism recombines the shifted beams into one. Therefore, the intensity distribution is a function of the spatial optical-path length distribution and correlated to the size along the optical axis. [35]

3

Chapter 3.

Experimental Measurements

In the following chapter six commercially available retroreflective foils will be classified by their specifications. The size of the CCRs embedded within the foil was not listed in the specification sheets in most cases and were therefore specifically requested. In addition, the structure will be analyzed by a DIC microscope for comparison. After that the setup will be presented to analyze the FFDP of each foil, whereby all requirements are discussed, such as the Fraunhofer conditions, including the collimation of the laser beam. Finally, the analysis and therefore the custom Python scripts will be examined.

3.1. Analysis of the Microscopic Structure

The foils were obtained from three different companies, whereby care was taken to ensure that the embedded CCRs differ in size. In addition, the highest reflectivity class was preferred.

The foils are either coated with aluminum or rely on TIR. The thickness ranges from between 0.2 mm (VC170) to 0.5 mm (OR6910). Additionally, an adhesive layer is integrated. Next to four common types of foil, so-called Lasercubes® developed by IMOS will be analyzed. This type is neither flexible nor adhesive and embedded in a plastic case. Table B.2 lists each foil with their relevant specifications.

Based on a microscopic analysis the foils can be classified into three groups: hexagonal, triangular and unclassified CCRs. Figure 3.1 shows the difference between the hexagonal and the triangular shape, whereby the size of the embedded CCRs was measured by their hexagonal output aperture. The foil 3M4090 could not be classified into either a hexagonal or a triangular array structure. The company have not provided any information regarding the structure size. The microscopic structure is presented in Figure 3.2.

Upon reviewing Table B.2 a difference in size of the diameter between the manufacturer and the DIC analysis can be seen, which is attributed to the measurement method. The diameter of the hexagon should be measured in the same manner as for a circle. Since a circle can be considered as a polygon with an infinite number of edges, the hexagonal diameter must be measured between opposite corners, rather than between opposite sides. Therefore, the manufacturer specification is not flawed, the size is just measured between opposite sides. It should be emphasized throughout the entire study that when referring to D_{hex}, the hexagonal output aperture of both hexagonal CCRs and triangular CCRs is meant.

The additional missing data can be attributed to the fact that the specific request was restricted to the size of the embedded CCRs, as the other specifications are not relevant for the calculation of the link budget.

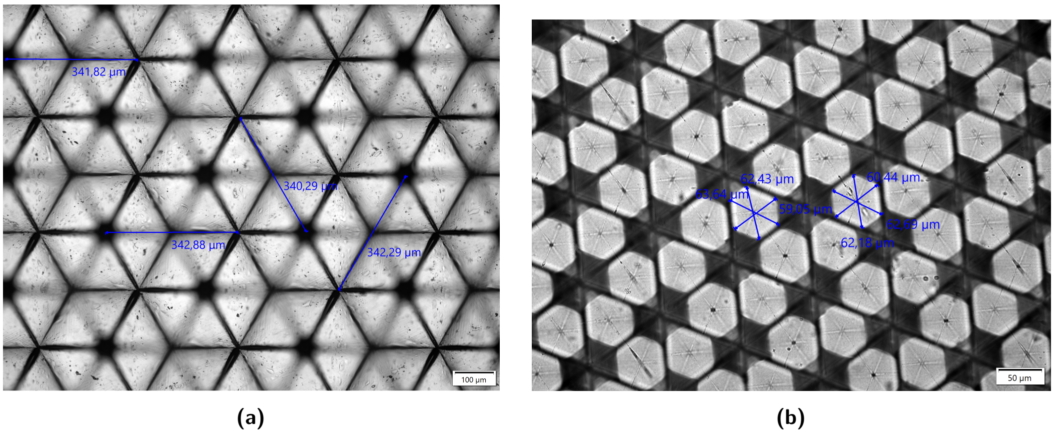

Figure 3.1.: Microscopic structure of M120-24 (a) and VC170 (b). Although the input apertures differ (hexagonal in (a) and triangular in (b)), the hexagonal output aperture is clearly visible on both foils.

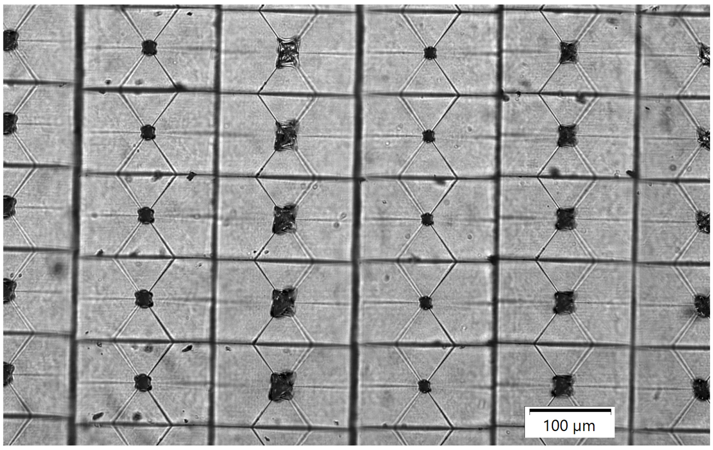

Figure 3.2.: Microscopic structure of 3M4090.

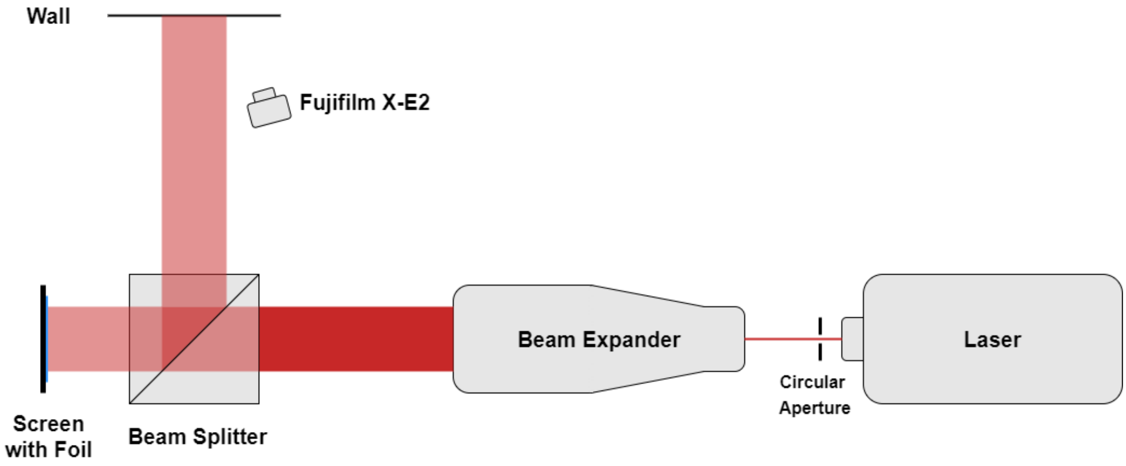

Figure 3.3.: Schematic of the setup for analyzing the FFDP of retroreflective foils.

3.2. Setup

Figure 3.3 shows a schematic of the setup. This study is using a helium-neon laser, a type of gas laser which operates at $\lambda = 632.8\,\mathrm{nm}$. The laser beam is filtered separately with a circular aperture. In the next step the beam is expanded and collimated with a beam expander. After that, a beam splitter is used. First the beam passes through the beam splitter and hits the screen on which the foil is applied. The angle of incidence is orientated normally to the foil. The retroreflective beam passes the beam splitter again and is deflected at an angle of 90° hitting the wall in the distance d. A camera captures the FFDP. Table B.3 provides an inventory of all relevant optical systems used in the setup.

3.2.1. Requirements

The setup was continuously improved over multiple experimental series. For improved collimation, a custom lens setup was replaced by the previously mentioned beam expander to ensure Fraunhofer conditions. Equation 2.3a can be used to estimate the required distance d between the aperture and the wall, whereby $(\xi + \eta^2)_{max}$ can be expressed through the hexagonal output aperture D_{hex} of the CCR. Additionally, an indicator can be defined by dividing d, which can be written by

$$N'_F = \frac{D_{hex}^2}{\lambda d} \ll 1. \tag{3.1}$$

For estimation purposes, the largest diameter should be used. The distance between the foil and the screen was limited to the dimensions of the laboratory and is $d = 4.32\,\mathrm{m}$. With the wavelength $\lambda = 632.8\,\mathrm{nm}$ and the largest diameter $D_{hex} = 462\,\mu\mathrm{m}$ the indicator yields $N'_F \approx 0.08$, which is at the boundary but still likely within an acceptable range.

In addition, a beam splitter with an undefined wavelength range was replaced to reduce the effect of ghosting. Further, the stabilization time of the laser was measured. As seen in Figure C.3 the laser exhibits three typical phases. The transient phase lasted approximately 40 seconds before transitioning into the warm-up phase. After around 800 seconds the laser reached a stable state, indicating the necessary warm-up time for all measurements.

3.2.2. Analysis of the FFDP

To reduce noise the room was darkened to the maximum extent. The patterns were captured with an exposure time of 8 seconds.

Calibration

Alongside the recording a calibration is necessary to determine the pixel size. Figure C.4 shows the used calibration tool, which is simply a picture of vertical dark lines in a fixed distance of 2.5 mm to each other. After postprocessing the raw data of the calibration image, the two-dimensional array is cut horizontal. As seen in Figure 3.4 the intensity distribution is only approximately rectangular, so that the distance between two lines depends on the position of the horizontal cut. Therefore, the cut is set as low as possible to reach the local minima. The distance between each cut is measured in pixels. The data is collected in an array and after that filtered. The resulting pixel resolution is $P_x = (0.0962 \pm 0.0034)\,\frac{\mathrm{Pixel}}{\mathrm{mm}}$, which corresponds to a derivation of about 3 %.

Analysis

The Python libraries *numpy* and *scipy* are used for mathematical calculations. All figures are presented using *matplotlib*. For the analysis the raw data is used and evaluated by *rawpy*. All parameters which adapt to the brightness are deactivated. The postprocess of the raw data yields a two-dimensional array, where each element contains the intensity of the RGB values measured in bits. At the wavelength used here, it is sufficient for the analysis of the intensity distribution to focus on the R value.
In addition to creating a heatmap, the intensity of the FFDPs is also analyzed radially. For each pixel a radius is created in the cartesian array, as shown in Figure 3.5. An approximation between adjacent pixels is ignored. The centering is set manually by using vertical and horizontal cut lines through the array with the alignment based on the maximum intensity values. For each radius the mean intensity is calculated, so that a square picture with $n \times n$ pixels will give $n/2$ values of intensity per radius.

For each foil the intensity distribution is analyzed linear and logarithmic. Alongside the experimental data the plots also include a theoretical estimation. The Airy function can be adapted for hexagonal apertures[1], allowing the expected position of the first minimum from the envelope to be calculated using the diameter D_{hex} of the embedded CCRs. Therefore Equation 4.8 is used. The minimum is represented as a blue dashed circle in the heatmap and as a blue dashed vertical line in the intensity distribution. The diameter is taken from the microscopic data also listed in Table B.2.

---

[1] The relation between the Airy function of a circular aperture and the intensity distribution of a hexagonal or a triangular CCR will be discussed later in Chapter 4.

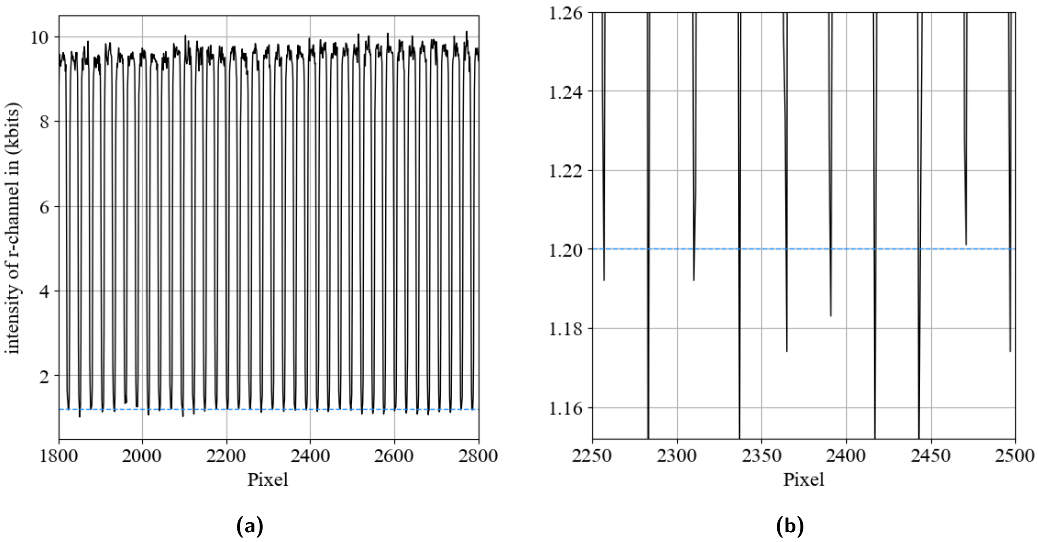

Figure 3.4.: Intensity distribution of the r-channel along a horizontal cut through the calibration image (a). In addition, the cut represented in blue is shown as a zoomed-in view (b).

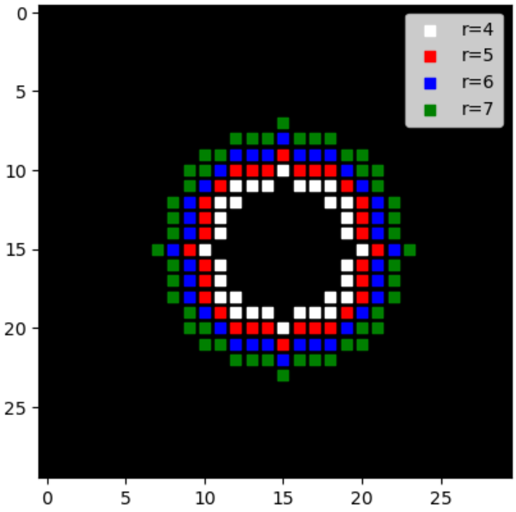

Figure 3.5.: Simplified representation of the radial evaluation of a Cartesian array.

Results

The results are shown on the following pages. Diffraction effects are clearly visible in all measurements. However, there are significant individual differences.

Figure 3.9 shows the FFDP of the foil VC170, in which, alongside a clear minimum in the radial intensity distribution, secondary maxima can also be observed. The main maximum is circular, analogous to the diffraction pattern of a hexagonal aperture. A diffraction angle of $\theta_{min,0} \approx 12.8\,\text{mrad}$ is in clear agreement with the value expected from the envelope of the embedded CCR with a diameter of $D_{hex} = 66\,\mu\text{m}$. The array function in between the envelope could not be observed in the diffraction patterns examined here.

The remaining triangular foils OR6910 and F056 in the Figures 3.8 to 3.11 exhibit more complex structures, although they show characteristic star-shaped diffraction patterns. While the radial distribution of OR6910 shows a kind of saddle point between 5 to 10 mrad, no clear minima can be identified, making a definitive statement about the diffraction angle difficult. In general, however, this angle appears to be significantly larger as expected according to the heatmaps. The assumption of uniformly distributed perfectly hexagonal apertures shows significant deviations from the actual conditions in this case. In accordance to Figure C.1 both foils do not exhibit equilateral triangular CCRs, causing the hexagons to be asymmetrical and the arrangement to deviate, leading to pair formation. Furthermore, effects of the macrostructure also play a role in OR6910 (see Figure C.2).

The Lasercubes® M120-24 and M149-20, embedded with hexagonal CCRs, clearly exhibit more distinct star-shaped patterns as seen in the Figures 3.12 to 3.15. However, no minima can be clearly identified here either. Nevertheless, the intensity distribution clearly shows that the diffraction angle of M120-20 is significantly larger, while for M149-20, a substructure with high intensity appears within the expected main maximum of the envelope.

For 3M4090, no relation could be established between the microscopic structure and the diffraction pattern due to the unknown microscopic structure. Therefore, the analysis is correspondingly limited to a heatmap and a radial distribution, which is shown in the Figures 3.16 and 3.17.

For the calculation of the OCS, the relationship between the microscopic structure, or rather the diameter of the embedded CCRs, and the diffraction angle is essential. With VC170, this estimation can be implemented. Here, by assuming a specific diameter, the diffraction angle can be determined using Equation 4.8, and the intensity distribution can be calculated with Equation 4.7. As already mentioned, the adaptation of the Airy function to fit the FFDP of hexagonal and triangular CCRs will be examined in detail in the next chapter. In addition, this chapter will also explore the observed diffraction effects in detail, covering both coherent and incoherent scenarios.

The other foils, however, exhibit more complex diffraction patterns, which sometimes lead to much larger diffraction angles than expected based on their microscopic structure. It can therefore be assumed that a general correlation between embedded CCRs and circular main maxima cannot be assumed by using the Airy function or a simple adaption. The microscopic structure is crucial. Nevertheless, as will be discussed in detail later, the adaptation of the Airy function to hexagonal CCRs can also be used to further expand the diffraction angle, thereby not exactly covering the experimentally observed diffraction phenomena, but rather providing an appropriate compromise.

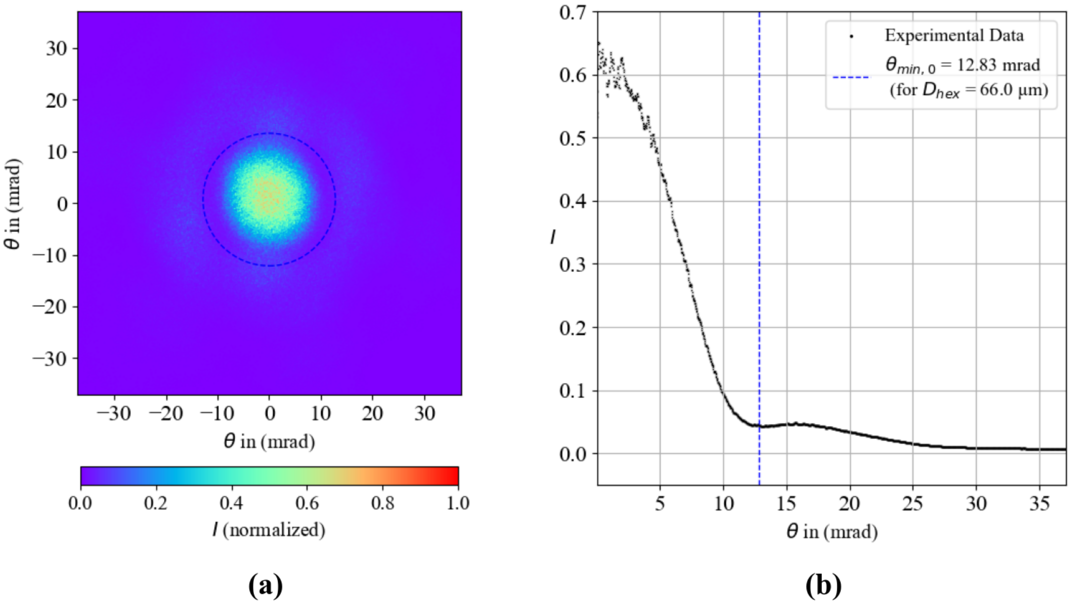

Figure 3.6.: FFDP (a) with the corresponding radial intensity distribution (b) of foil VC170.

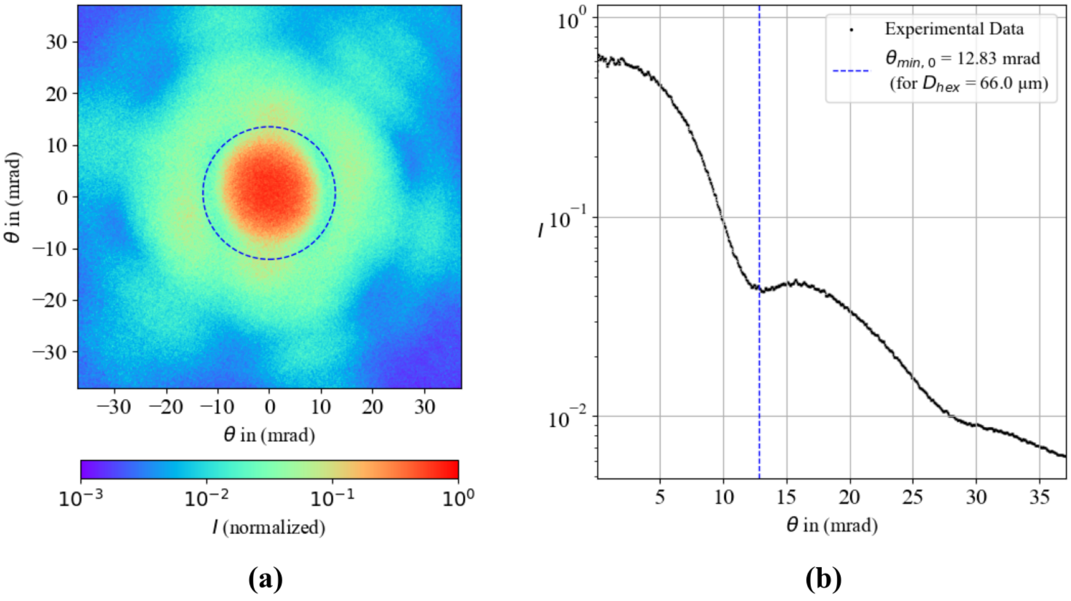

Figure 3.7.: Logarithmically scaled FFDP (a) with the corresponding radial intensity distribution (b) of foil VC170.

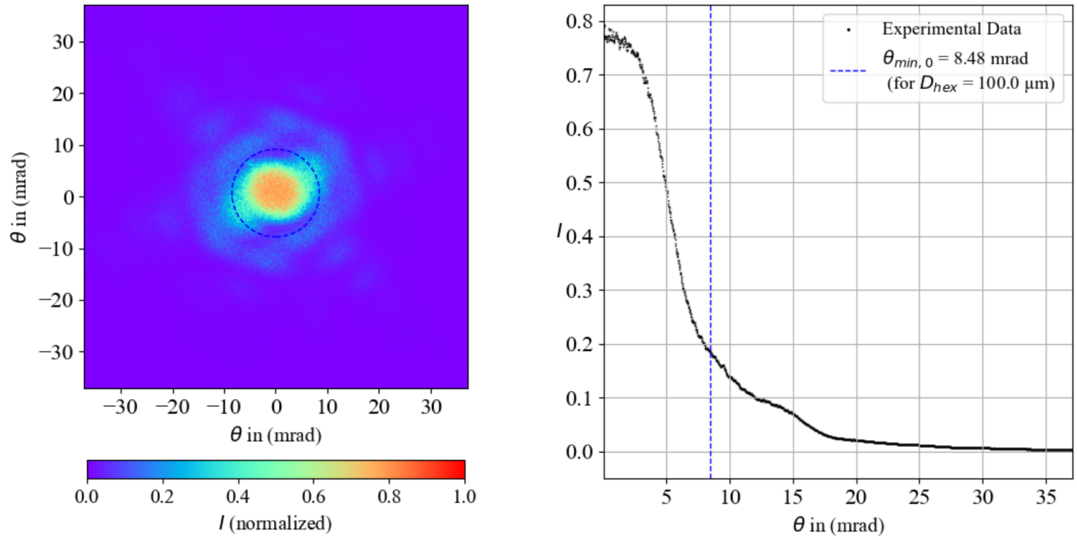

(a) **(b)**

Figure 3.8.: FFDP (a) with the corresponding radial intensity distribution (b) of foil F056.

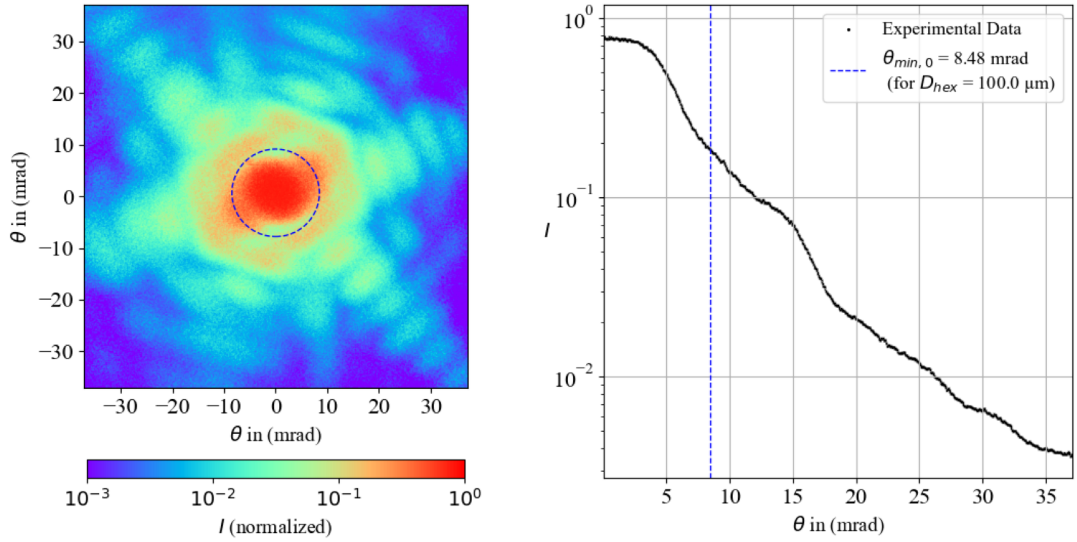

(a) **(b)**

Figure 3.9.: Logarithmically scaled FFDP (a) with the corresponding radial intensity distribution (b) of foil F056.

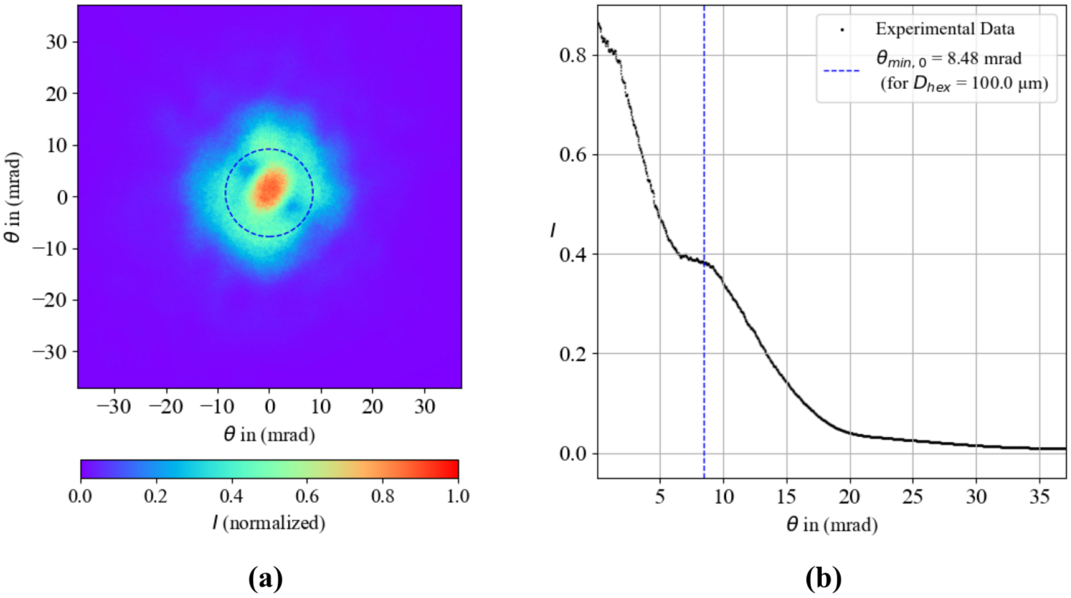

Figure 3.10.: FFDP (a) with the corresponding radial intensity distribution (b) of foil OR6910.

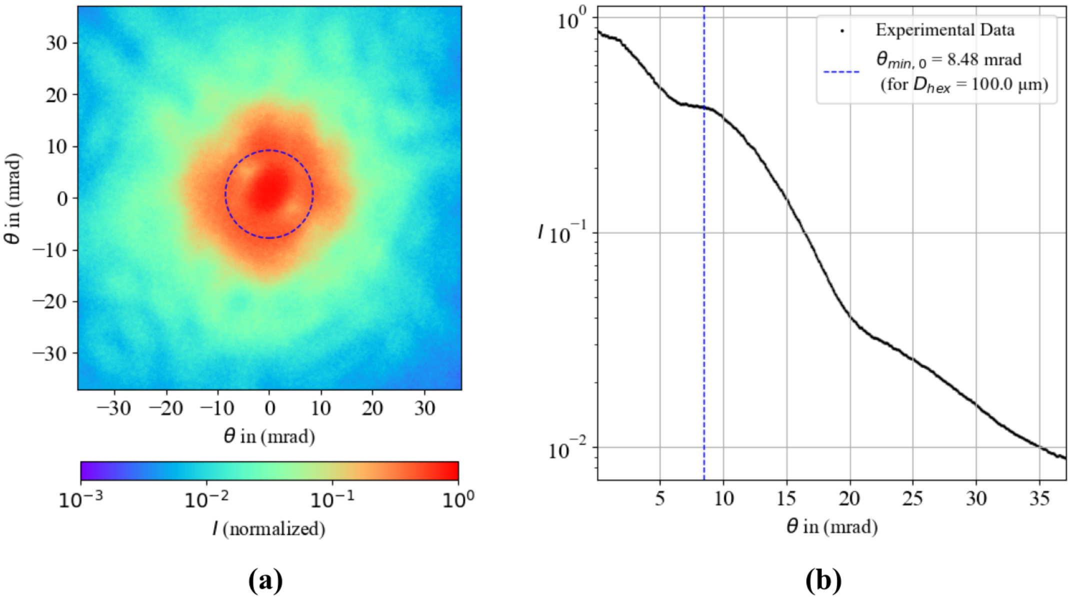

Figure 3.11.: Logarithmically scaled FFDP (a) with the corresponding radial intensity distribution (b) of foil OR6910.

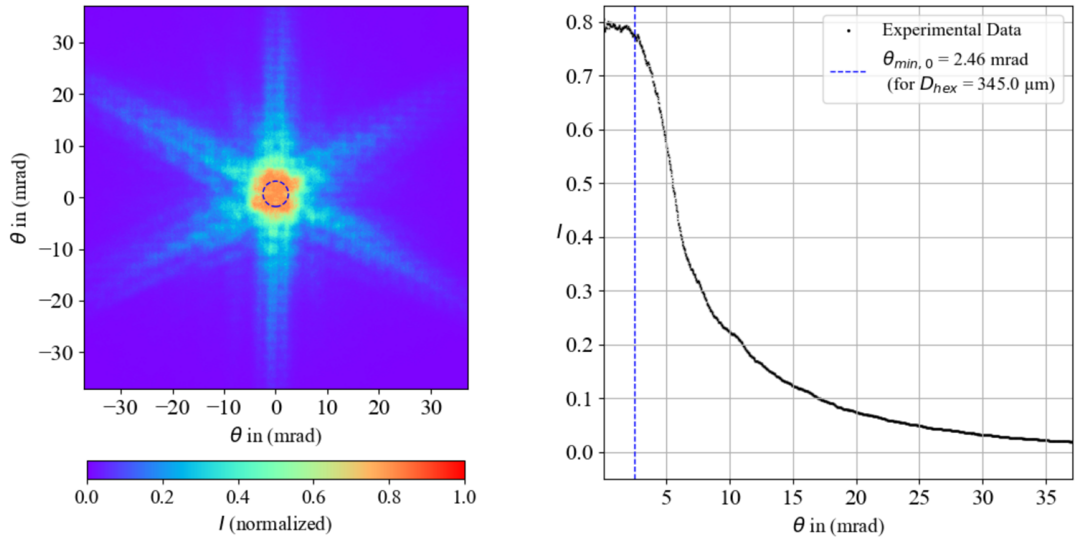

(a) **(b)**

Figure 3.12.: FFDP (a) with the corresponding radial intensity distribution (b) of foil M120-24.

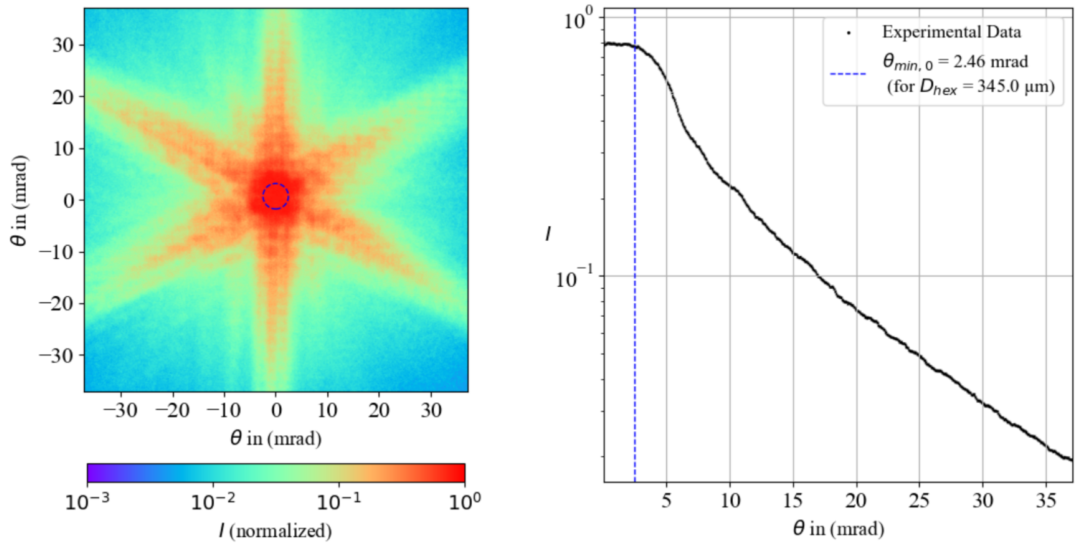

(a) **(b)**

Figure 3.13.: Logarithmically scaled FFDP (a) with the corresponding radial intensity distribution (b) of foil M120-24.

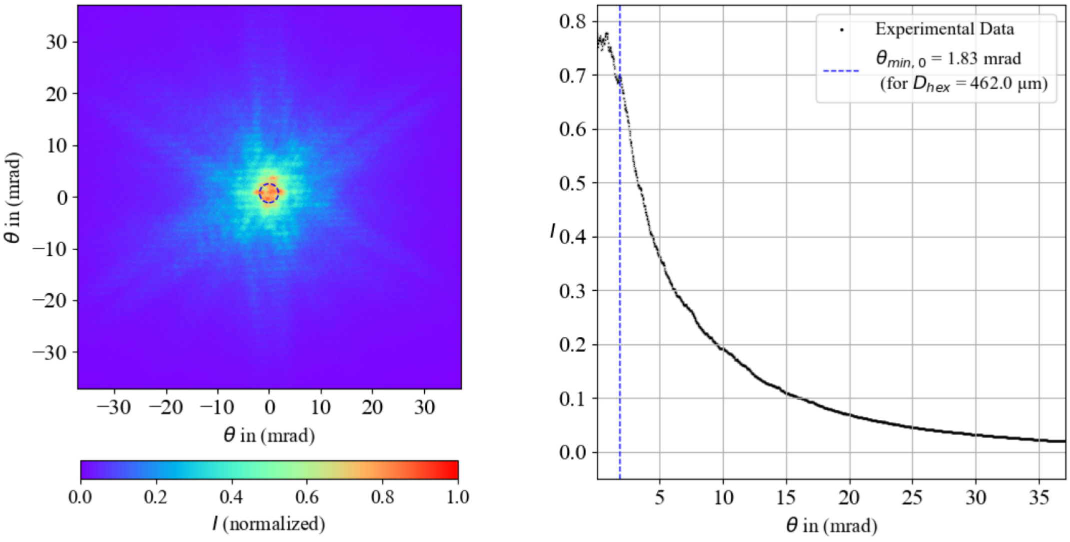

(a) **(b)**

Figure 3.14.: FFDP (a) with the corresponding radial intensity distribution (b) of foil M149-20.

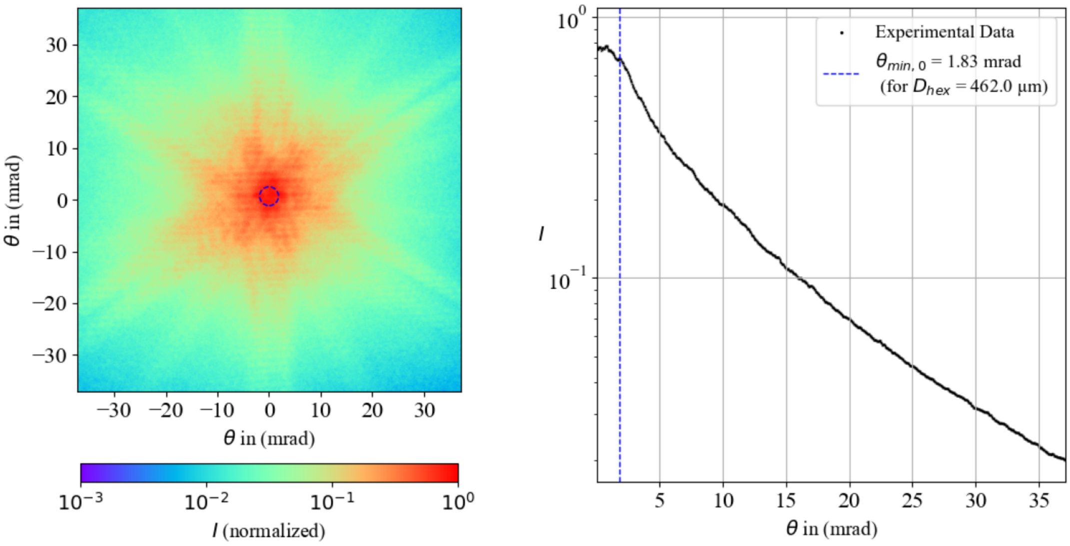

(a) **(b)**

Figure 3.15.: Logarithmically scaled FFDP (a) with the corresponding radial intensity distribution (b) of foil M149-20.

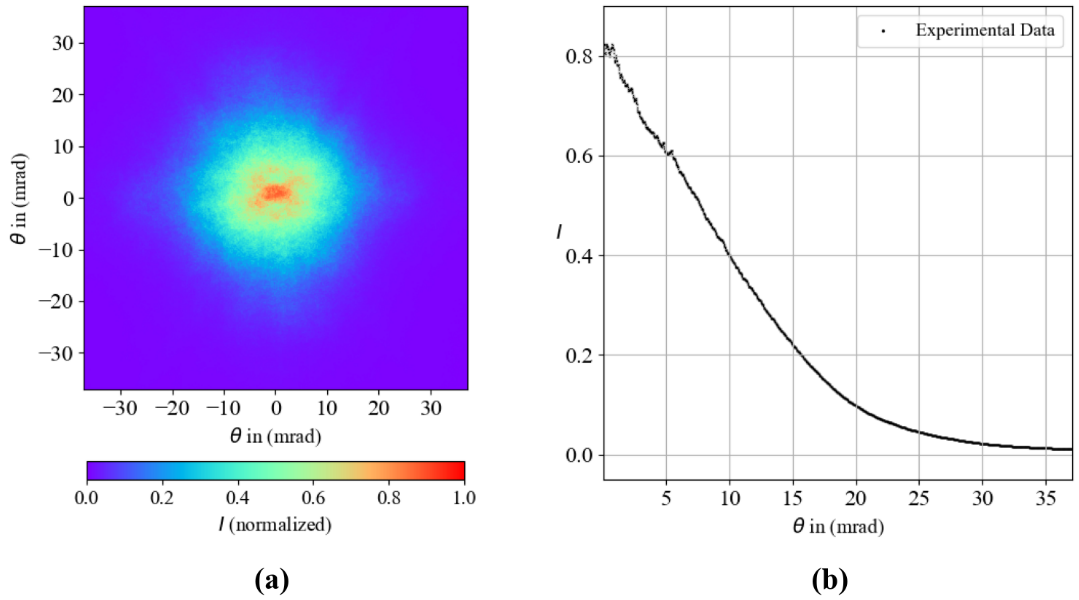

Figure 3.16.: FFDP (a) with the corresponding radial intensity distribution (b) of foil 3M4090 without an analytically description.

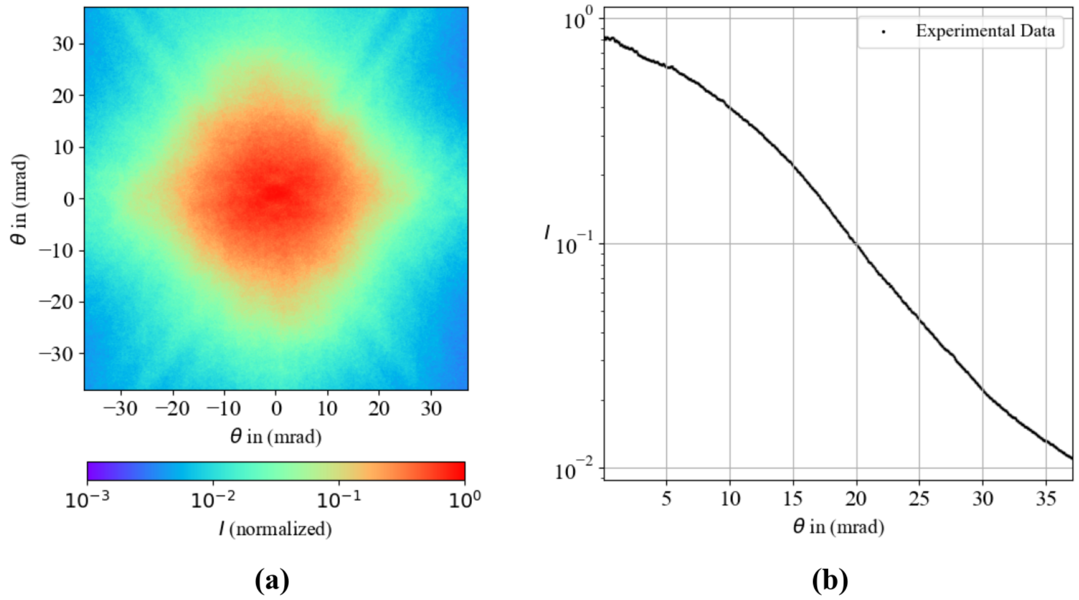

Figure 3.17.: Logarithmically scaled FFDP (a) with the corresponding radial intensity distribution (b) of foil 3M4090 without an analytically description.

In addition to the analysis of the FFDPs, Figure 3.18 shows a specular reflection, which was detected by each foil with and without attached on the screen under a small angle of incidence.

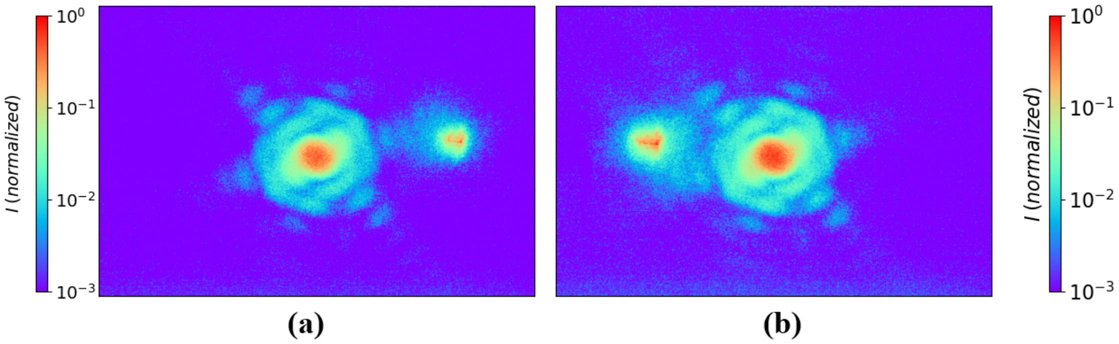

(a) **(b)**

Figure 3.18.: Logarithmically scaled FFDP of foil F056 with specular reflection. In (a), the screen is tilted slightly in a clockwise direction, while in (b), it is tilted slightly in a counterclockwise direction. A Calibration was not performed; thus, no quantitative assessment can be presented.

4

Chapter 4.

Simulation Analysis

The following chapter will further investigate the diffraction effects observed in the experiment with retroreflective foils. In this context, a consistent relationship between the microscopic structure and the FFDP should be established, along with an analytical description of the intensity distribution equivalent to Equation 2.8 for the case of a hexagonal CCR. In addition, the aperture behavior of an ideal CCR will be examined. Finally, a comprehensive analysis of CCR arrays will be conducted in accordance with the array theorem.

4.1. Settings

As already discussed, the Fraunhofer conditions has to be ensured. In Zemax plane waves creating source can be constructed with setting a focal image, so that the physical distance is negligible. Additionally, Zemax needs to define an input aperture for the simulation system. Therefore, a circular aperture is used. The diffraction is minimized by setting the diameter much larger than the dimensions of the apertures and CCRs under investigation. All files are built in mixed mode. The sequential mode provides only the basic characters for the research. To build complex optical structures like idealized retroreflective foils it is necessary to define custom polygon objects which is only done in non-Sequential mode. For all simulations a wavelength of $\lambda = 633\,\mathrm{nm}$ is used. Unless explicitly stated otherwise the incidence angle of the wave front is orientated normal to the face of the apertures.

4.2. Data Analysis

For further adjustments, such as the analysis of the simulation data and the constructing of the retroreflective arrays, custom Python scripts are used. For the investigation of the FFDPs, the script of the experimental analysis is extended. In addition to the expected position of the first minimum from the envelope with the diameter of the embedded CCRs measured in the microscope, the intensity distribution of this diameter is also plotted. Therefore Equation 4.7 is used.

The calculated FFDP in Zemax consists of two-dimensional arrays and is read in from a text file. Each element in the array stays for a value of intensity, where the intensity is normalized.
Additionally Zemax uses $\sin(\theta)$ for the field angle. To compare the simulation data with the analytical calculation, particularly Equation 2.8, the calculations must be adjusted accordingly.

As already mentioned, Zemax provides the so-called polygon-objects, where complex structures can be defined and included in the non-sequential mode. Therefore, the polygon syntax is used, requiring the definition of the coordinates of the edges, the connections between each edge, the type of surface, and the optical properties.[1] For the constructing of the CCRs certain calculations must be performed, where the triangular and the hexagonal CCRs presented separately. Figure 2.5, previously introduced in Section 2.2, shows the two types of CCRs used in this study. The edge points were defined along the axes, so that the normal of the face is along $n_{face} = (x, y, z)$.

The hexagonal structure is defined by three mutually orthogonal squares, which are specified in the Python script using a quadratic edge length with a value of a_c. Three out of six edge points lie in the same plane. Nevertheless, all six points create the hexagonal output aperture. The challenge in construction lies in expressing a_c as a function of the diameter of the hexagonal output aperture (cf. Section 3.1 for measurement method). This can be done by using the projected edge length of this hexagon. The three edge points $P_1 = (a_c,\, 0,\, a_c)$, $P_2 = (0,\, a_c,\, a_c)$ and $P_3 = (a_c,\, a_c,\, 0)$ lie in the same plane which can be defined by

$$E_h = x + y + z - 2 \cdot a_c = 0. \tag{4.1}$$

The opposite corner (hexagonal output aperture) of P_1 is denoted as $P_4 = (0,\, a_c,\, 0)$. The distance between E_h and P_4 in direction of the normal vector of E_h and therefore the projected edge length can be calculated by

$$d_h = \frac{|Ax_4 + By_4 + Cz_4 + D|}{\sqrt{A^2 + B^2 + C^2}}, \tag{4.2}$$

where $A = B = C = 1$, $D = -2a_c$, $x_4 = z_4 = 0$ and $y_4 = a_c$ gives

$$d_h = \frac{1}{\sqrt{3}} a_c. \tag{4.3}$$

The distance between the opposite corners is $|\overrightarrow{P_1P_4}| = \sqrt{3}\, a_c$. Using the Pythagorean theorem, the diameter of the output aperture of a hexagonal CCR can be written by

$$a_c = \frac{\sqrt{6}}{4} D_{hex}. \tag{4.4}$$

---

[1] vgl. [34, 695ff.]

A much simpler method can be used for the triangular CCR. Here too, the structure is defined along the axes with a length of a_c. The edge length of the input aperture (equilateral triangle) a_{tria} can be related to the hexagonal output aperture with

$$a_{tria} = \frac{3}{2} D_{hex}. \tag{4.5}$$

Further the term $a_{tria} = \sqrt{2}\, a_c$ leads to

$$a_c = \frac{3\sqrt{2}}{4} D_{hex}. \tag{4.6}$$

Alongside simple CCRs the Python script can be extended to copy and rotate operations to even construct arrays. Therefore, the edge points of a single CCR will be rotated 5 times 60° around one fixed edge point. After that the structure is shifted 6 times again.

4.3. Results

First, the FFDP of a circular and a hexagonal aperture will be examined. A relation between both diffraction patterns will be analyzed and an analytical description for the intensity distribution will be adapted. Subsequently, this simulation will be extended to analyze hexagonal and triangular shaped CCRs. The consistency between the CCRs and apertures previously discussed will be observed. The last part of this chapter will simulate the FFDP of CCR arrays. Additionally, the incoherent cases discussed in Section 2.1.3 will be examined.

4.3.1. Single Apertures

Figures 4.2 and 4.3 show the FFDP with the corresponding radial distribution of a circular and hexagonal aperture[2]. The circular aperture shows the expected Airy disk distribution. The radial intensity distribution and the angular position of the first minimum are consistent with the Equations 2.8 and 2.9.

As seen the central maximum of the hexagonal aperture is still circular shaped with a larger diameter. If the first minimum of the circular and the hexagonal aperture is related for different diameters, a linear relation is evident. Figure 4.1 shows this linear correlation between the first minima, allowing for the introduction of the stretch factor a_s that can be used to radially stretch the intensity distribution which can be written by

$$I_{hex}(\theta) = I_0 \left(\frac{2 J_1(a_s k\, r_{hex} \sin(\theta))}{a_s k\, r_{hex} \sin(\theta)} \right)^2 . \tag{4.7}$$

In addition, the first minimum for a hexagonal aperture can be adjusted, resulting in

$$\theta_{hex_{min,0}} \approx 0.61 \frac{\lambda}{r_{hex} \cdot a_s}. \tag{4.8}$$

---

[2] The FFDPs with a wide field angle are attached in Figure C.6

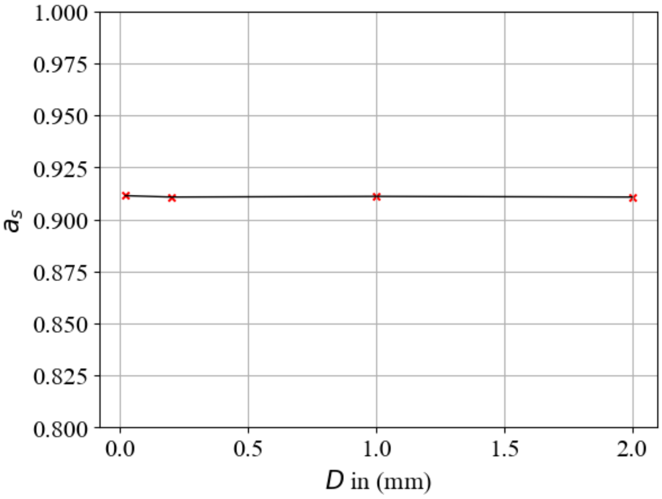

Figure 4.1.: Relationship between the first minimum of a circular and hexagonal aperture. The stretch factor is calculated by $a_s = (\theta_{circ_{min,0}} \,/\, \theta_{hex_{min,0}})$, where four different diameters demonstrate the linear relationship. The value $a_s = 0.911$ results from the mean of the four ratios.

Ensure that this applies only to the description up to the first order.
As previously mentioned, these equations are also used to provide an expected description of the intensity distribution, and the first minimum of the foils investigated in this study. This implies the assumption of perfectly hexagonal CCRs embedded in the foils. The adapted Airy function is also implemented in the analysis of the hexagonal aperture shown in Figure 4.3.

4.3.2. Single CCRs

Figure 4.4 and 4.5 show the FFDP with their corresponding radial distribution from a hexagonal and a triangular CCR, respectively, with both output apertures having the same diameter. As seen both the FFDP and the radial intensity distribution and so the first minimum are the same and identical to the diffraction properties of a hexagonal aperture. Accordingly, the adapted Airy function also aligns with the observed patterns here.

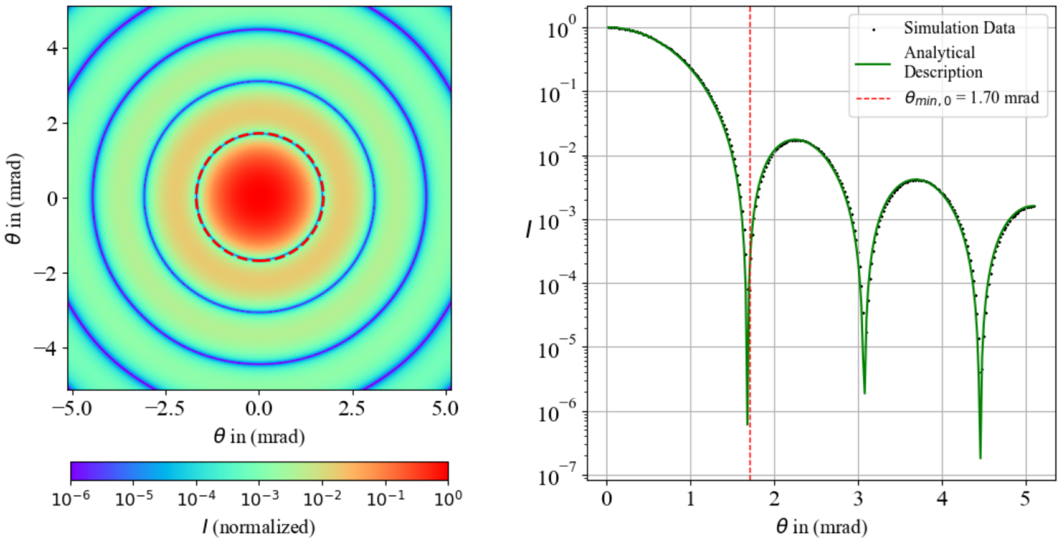

(a) **(b)**

Figure 4.2.: FFDP (a) and radial intensity distribution (b) of a circular aperture with a radius $r_{circ} = 230\,\mu\text{m}$ for a wavelength $\lambda = 633\,\text{nm}$. The first minimum $\theta_{min,0}$ is indicated by a dashed red line and circle in both plots, calculated from the simulation data. The analytical distribution (green) is calculated by Equation 2.8.

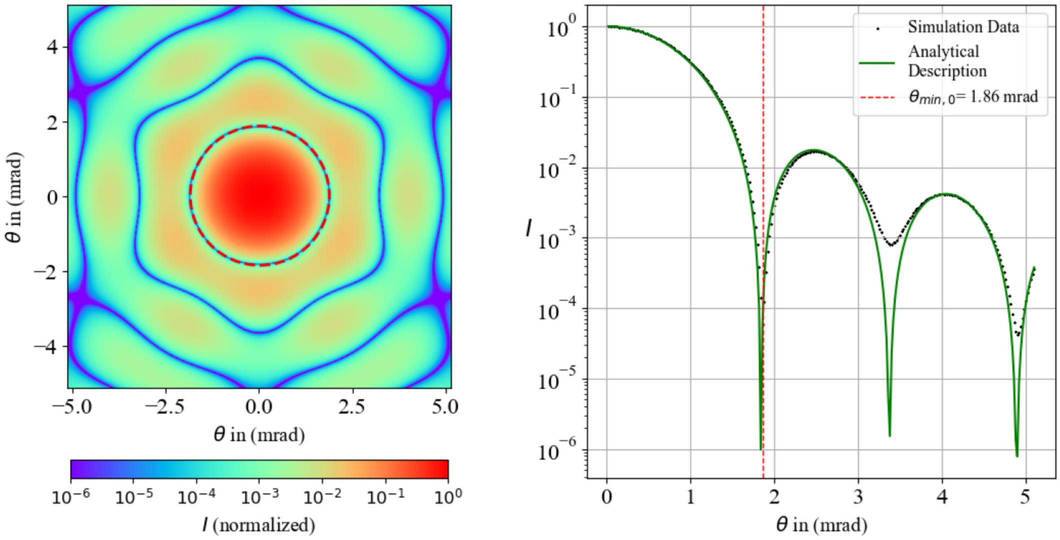

(a) **(b)**

Figure 4.3.: FFDP (a) and radial intensity distribution (b) of a hexagonal aperture with a radius $r_{hex} = 230\,\mu\text{m}$ for a wavelength $\lambda = 633\,\text{nm}$. The first minimum $\theta_{min,0}$ is indicated by a dashed red line and circle in both plots, calculated from the simulation data. The analytical distribution (green) is calculated by Equation 4.7.

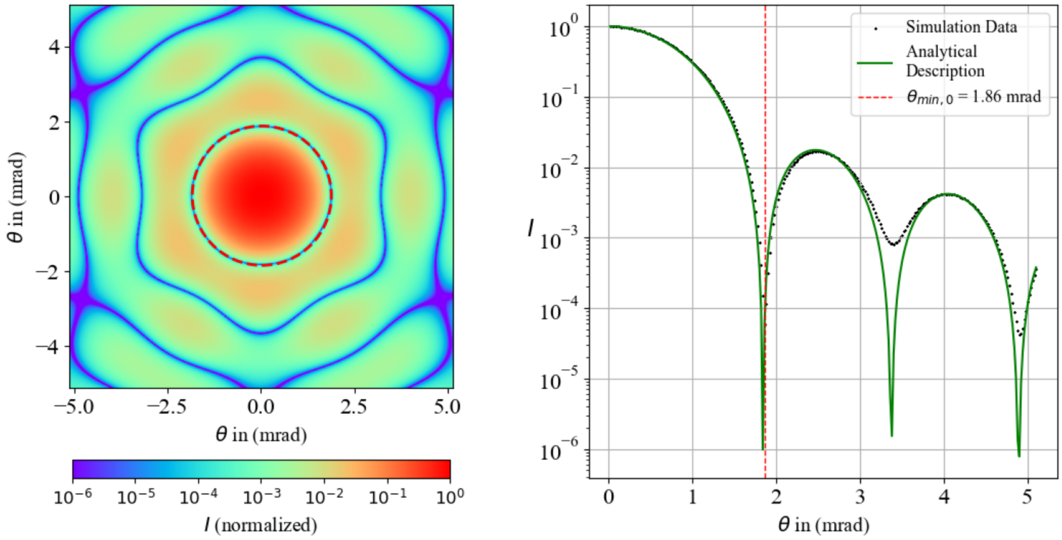

(a) **(b)**

Figure 4.4.: FFDP (a) and radial intensity distribution (b) of a hexagonal CCR with a diameter $D_{hex} = 460\,\mu\text{m}$ for a wavelength $\lambda = 633\,\text{nm}$. The first minimum $\theta_{min,0}$ is indicated by a dashed red line and circle in both plots, calculated from the simulation data. The analytical distribution (green) is calculated by Equation 4.7.

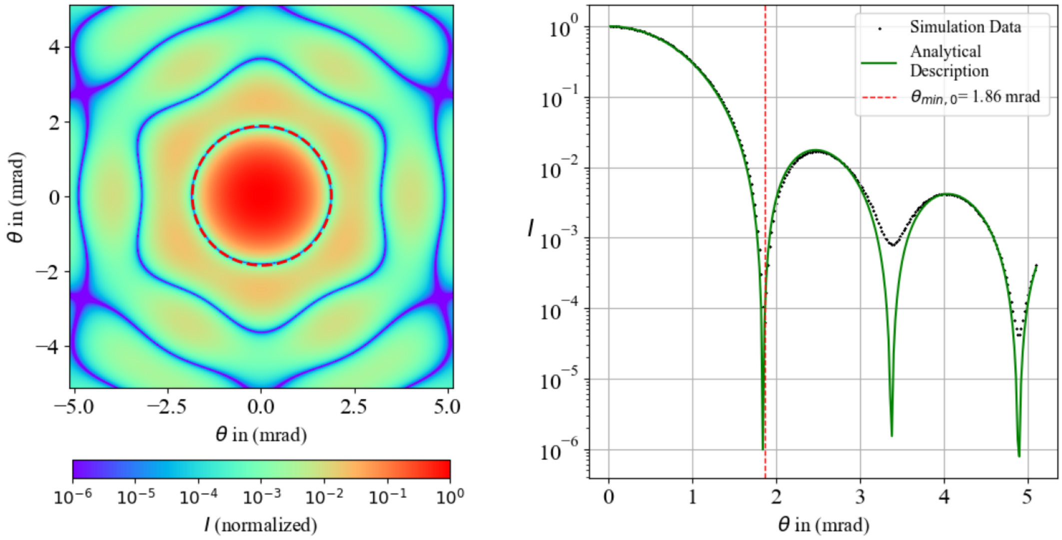

(a) **(b)**

Figure 4.5.: FFDP (a) and radial intensity distribution (b) of a triangular CCR with a diameter $D_{hex} = 460\,\mu\text{m}$ for a wavelength $\lambda = 633\,\text{nm}$. The first minimum $\theta_{min,0}$ is indicated by a dashed red line and circle in both plots, calculated from the simulation data. The analytical distribution (green) is calculated by Equation 4.7.

4.3.3. Array of CCRs

The analysis of the FFDPs from the array structures are separated in three different parts. Both the coherent and incoherent cases are examined, with two different approaches presented for the incoherent case.

Coherent Return

Figure C.7 and C.8 show the idealized arrays built with the polygon object syntax.
The FFDPs and the radial distributions are shown in Figure 4.6 and 4.7. Notably the central maximum is much smaller than the maximum from only one CCR the same size, which is consistent with the expectations of the coherent return, discussed in Section 2.1.3. The FFDP of the AF generates structures with significantly smaller diffraction angles, which are enveloped by the FFDP of the individual CCR (EF). The first maximum is $\theta_{0,min} = 0.24\,\mathrm{mr}$ in size.
Alongside the complex diffraction patterns generated by the AF, the first minimum of the EF is also recognizable, which is marked with a dashed red line and circle. Figure C.9 shows the FFDPs with a wide field angle. Here the minimum from the EF are more clearly visible. The triangular array generates a more clearly first minimum, whereas the hexagonal array additionally exhibits side lobes. Therefore, the coherent diffraction patterns from the array structures align well with the array theorem and therefore the overall expectations.

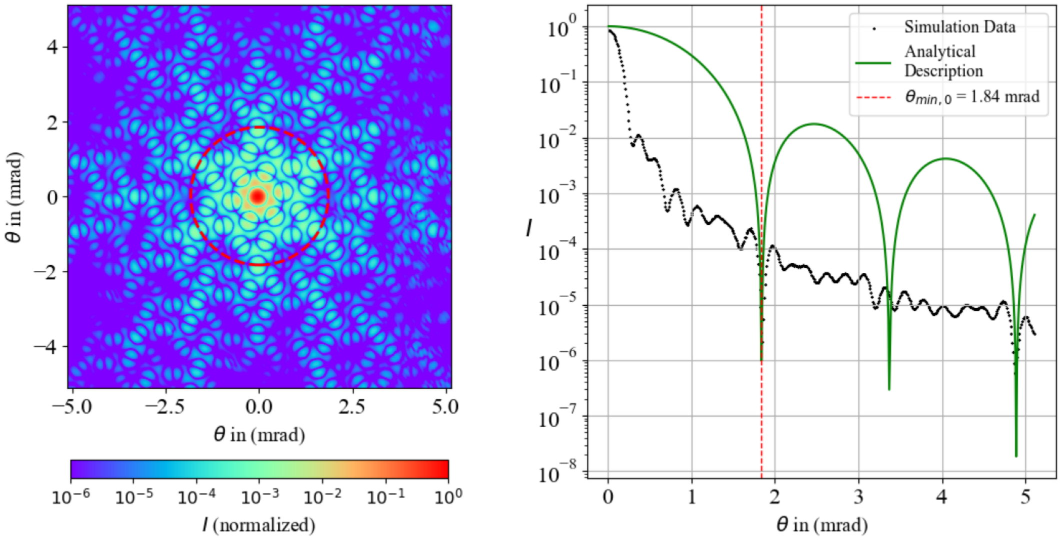

(a) **(b)**

Figure 4.6.: The FFDP (a) and radial intensity distribution (b) of an array of triangular CCRs, where the embedded CCRs have a diameter of $D_{hex} = 460\,\mu\mathrm{m}$. The utilized wavelength is $\lambda = 633\,\mathrm{nm}$. The analytical distribution (green) is calculated by Equation 4.7 due to the expected intensity distribution of the envelope (EF). The dashed red line and circle indicate the first minimum caused by a single CCR with a diameter of $D_{hex} = 460\,\mu\mathrm{m}$, calculated by Equation 4.8.

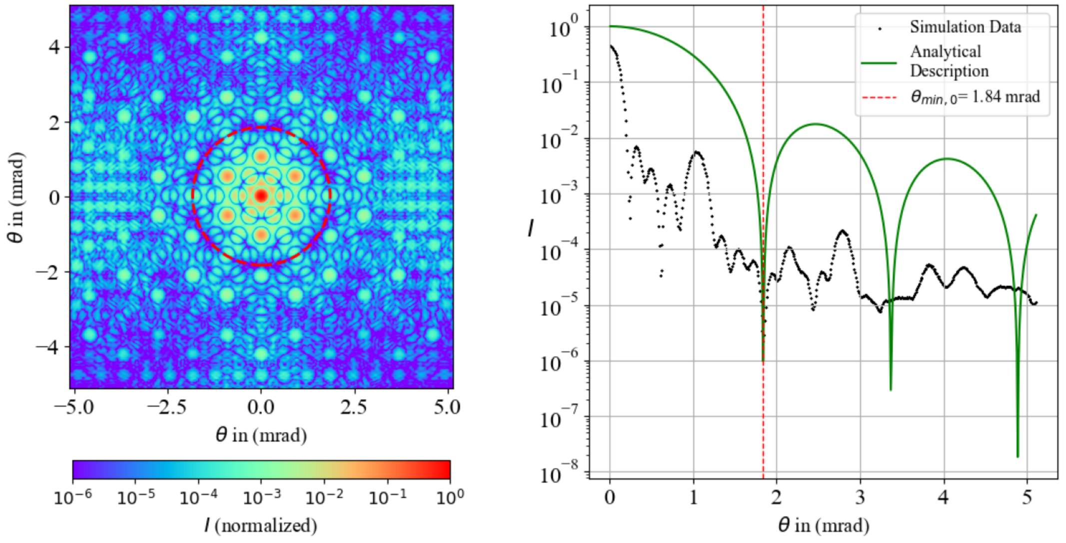

(a) **(b)**

Figure 4.7.: The FFDP (a) and radial intensity distribution (b) of an array of triangular CCRs, where the embedded CCRs have a diameter of $D_{hex} = 460\,\mu\text{m}$. The utilized wavelength is $\lambda = 633\,\text{nm}$. The analytical distribution (green) is calculated by Equation 4.7 due to the expected intensity distribution of the envelope (EF). The dashed red line and circle indicate the first minimum caused by a single CCR with a diameter of $D_{hex} = 460\,\mu\text{m}$, calculated by Equation 4.8.

The arrays from Figure C.7 and C.8 were fully illuminated. By reducing the illumination, the array function will be defined by the circular shaped beam, which is shown in C.10. Since the overall structure of the array changes, the entire diffraction pattern must accordingly change which as well represents a further agreement with the array theorem.

As can be seen from the simulation data, in the coherent case, the diffraction angle depends significantly from the FFDP of the array function, where the majority of the intensity is contained within $\theta = 0.3\,\text{mrad}$. The FFDPs in the coherent case differ significantly from those observed experimentally. As already mentioned and suspected, the diffraction patterns of the array functions cannot be recognized in the experiment due to the manufacturing errors of the foils and the general deviation from symmetrically arranged perfect hexagonal apertures. These deviations will now be further investigated in additional simulations.

Incoherent Return

First, the embedded CCRs can be built imperfect by modelling manufacturing tolerances. Therefore, the defined edge points of the array structure will be adapted by adding an offset δ_a in a range of $-\Delta\delta_a \leq \delta_a \leq \Delta\delta_a$ to each component of all edge points. Resulting gaps and overlaps are negligible, because the offsets will be in dimensions smaller than one wavelength.

In considering Figure 4.8 and 4.9 the FFDP becomes blurry proportional to the increasing manufacturing tolerance, which leads to an increased diffraction angle. This demonstrates how the FFDP of retroreflective foils arises in real scenarios providing a consistent explanation for why, in the experiment, the array function was not visible, and the diffraction angle was larger than theoretically expected in some cases. With increasing tolerance for errors, it is clearly observable how the diffraction pattern of the array function begins to blur, while a more homogeneous intensity distribution forms within the main maximum of the envelope. Further increase of the tolerance error also impacts the envelope. Simulation data have shown that with increasing error tolerance, a more homogeneous intensity distribution emerges across the entire diffraction pattern. The increasing diffraction angle produced due to manufacturing tolerances can be accounted for using the stretch factor a_s assuming a larger diffraction angle.

Next the array structure can be tilted, so that an angle of incidence will induce a phase shift of the wave front, which can be described by a gradient. Since the maximum number of defined points per POB file has been significantly exceeded, the array had to be divided into several substructures. During a rotation of the overall structure, displacements along the z-axis would also need to be performed, complicating the construction (Imagine cutting a line into two pieces and tilting both about their own center). Therefore, the hole POB files were combined into a CAD file using a Boolean function provided by Zemax.
The analysis of the gradient phase shift was evaluated using both triangular and hexagonal CCR arrays. The arrays were tilted about the x-axis by different angles, wherein each tilt is represented by two in a plot.
According to Section 2.1.3, a gradient phase in the array generate a spatial displacement of the central maximum generated by the EF. However, there are two differences compared to the principle of phased array antennas. First, if the array is tilted the output aperture of both the individual CCR (EF) and the overall array (AF) change, so that alongside a spatial shift the entire FFDP would also have to narrow. In addition, Figure 2.3 only assumes a one-dimensional arrangement by using a cosine function for the EF, resulting in analytical differences in both the EF and the AF.
Upon examining Figure 4.10, 4.11 and 4.12, not only the radial displacement is evident, but it also demonstrates how, through the multiplication of the EF with the AF, side lobes are significantly amplified and form equivalent maxima. It is notable that the number of maxima is increasing with the tilt, so that side lobes are significantly more visible compared in case of an antenna array. The change of the effective area is clearly visible in the hexagonal CCR arrays, where the EF transitions from a circular to an elliptical shape. As already seen in Figure C.7 and C.8 the triangular CCR exhibits a higher symmetry, which positively affects the centering of the FFDP in Zemax. Although the change in the effective area is not visible in Figures 4.13, 4.14 and 4.15, a central maximum is still evident in the center even at high angles. Especially at an incidence angle of $\theta_i = 45°$, one of the three planes in the CCRs is oriented orthogonally, thereby significantly impacting the FFDP. Nevertheless, the radial displacement is clearly visible.
Since the spatial displacement primarily affects the array function due to unavoidable tolerance errors, it is not accounted for in the calculation of the OCS. Therefore, no additional assumptions for the OCS calculation are made based on this investigation. Nevertheless, it was demonstrated here how an angle changes the effective area, in accordance with Section 2.4.1.

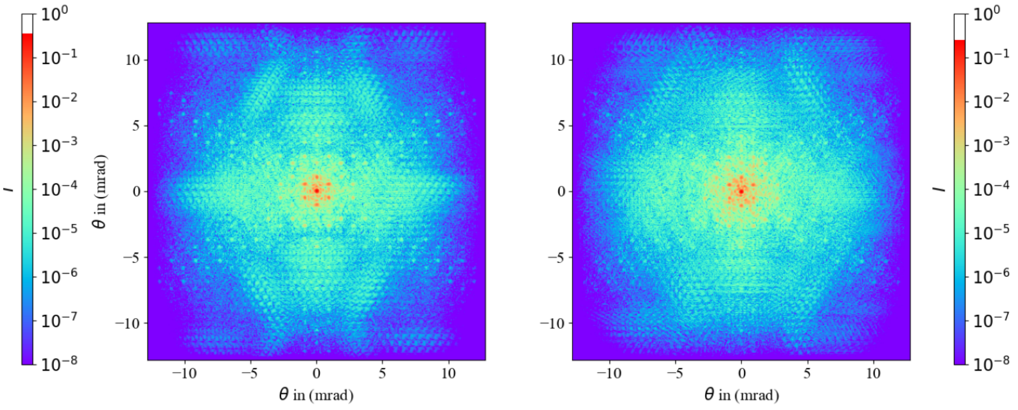

(a) **(b)**

Figure 4.8.: FFDP of a triangular CCR array with manufacturing tolerances of $\Delta\delta_a = 0.1\lambda$ (a) and $\Delta\delta_a = 0.2\lambda$ (b).

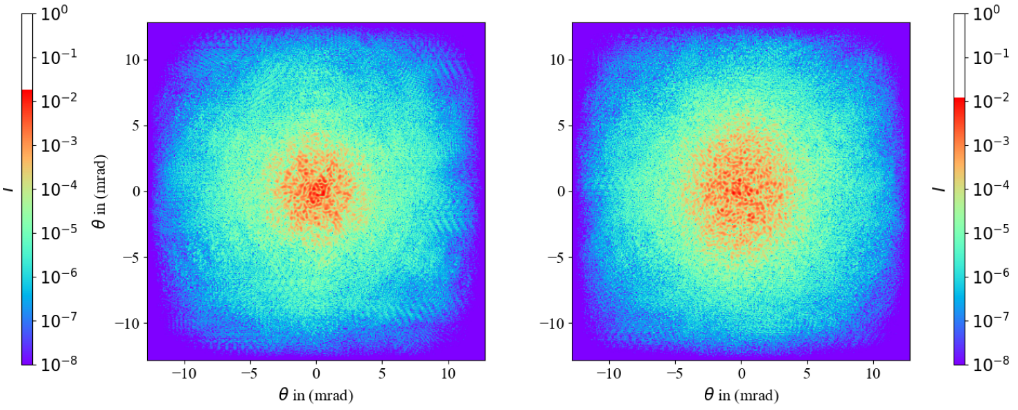

(a) **(b)**

Figure 4.9.: FFDP of a triangular CCR array with manufacturing tolerances of $\Delta\delta_a = 0.4\lambda$ (a) and $\Delta\delta_a = 0.7\lambda$ (b).

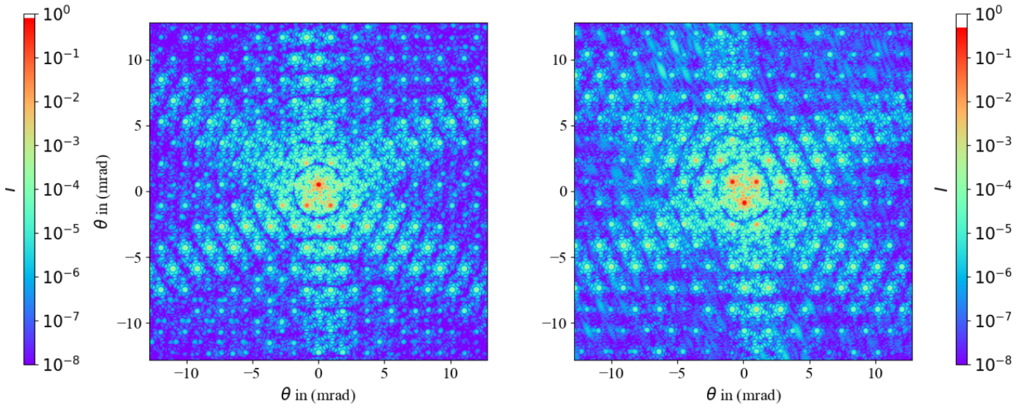

(a) **(b)**

Figure 4.10.: FFDP of a hexagonal CCR array with a tilt of 5° (a) and 10° (b) along the x-axis.

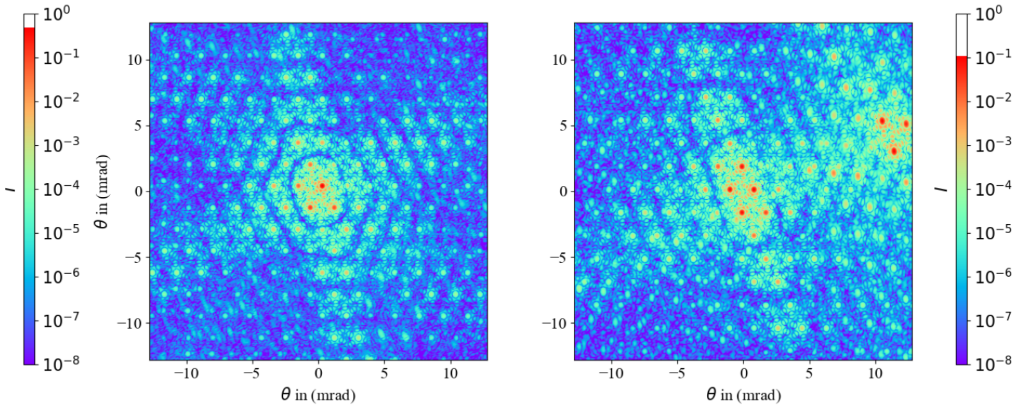

(a) **(b)**

Figure 4.11.: FFDP of a hexagonal CCR array with a tilt of 15° (a) and 25° (b) along the x-axis.

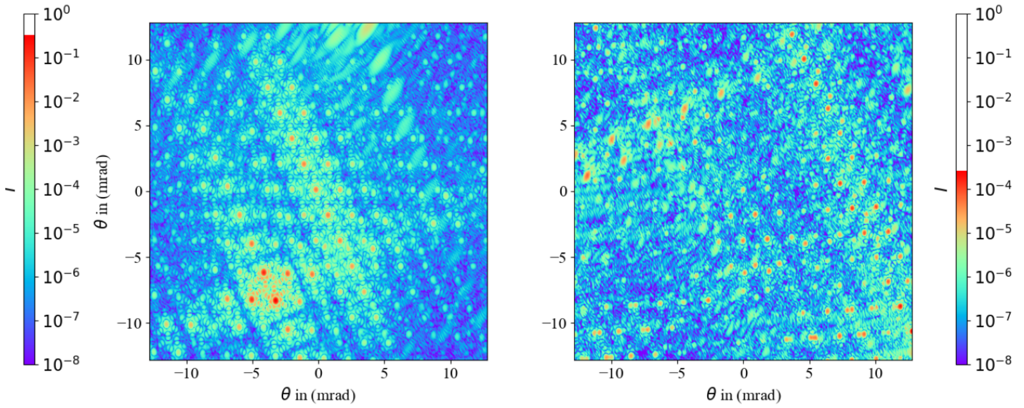

(a) **(b)**

Figure 4.12.: FFDP of a hexagonal CCR array with a tilt of 35° (a) and 45° (b) along the x-axis.

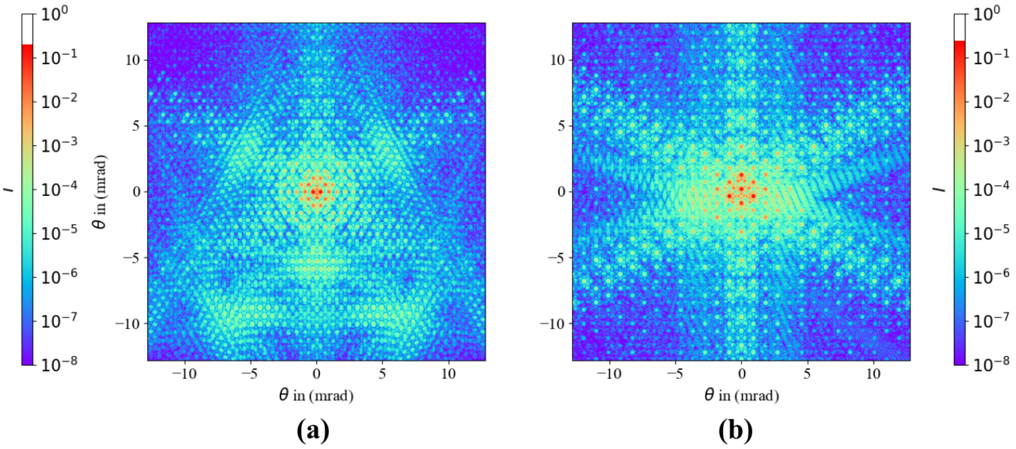

Figure 4.13.: FFDP of a triangular CCR array with a tilt of 5° (a) and 10° (b) along the x-axis.

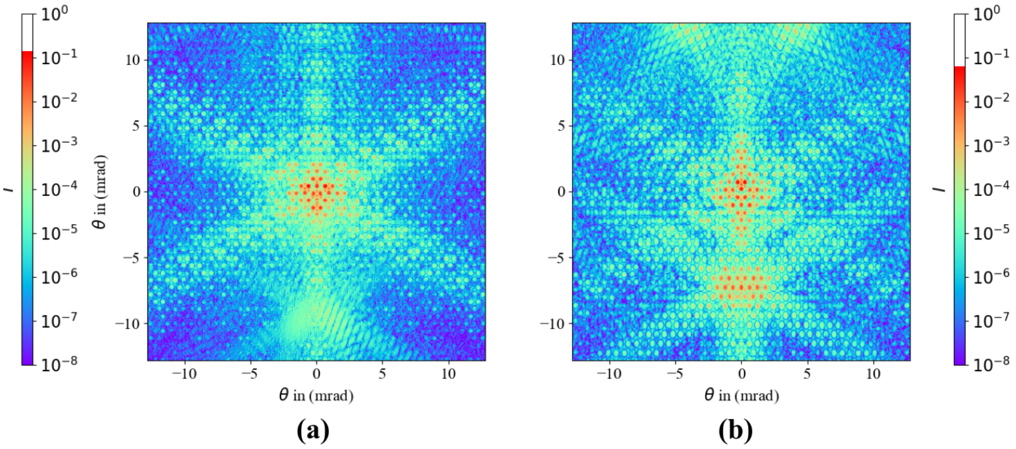

Figure 4.14.: FFDP of a triangular CCR array with a tilt of 15° (a) and 25° (b) along the x-axis.

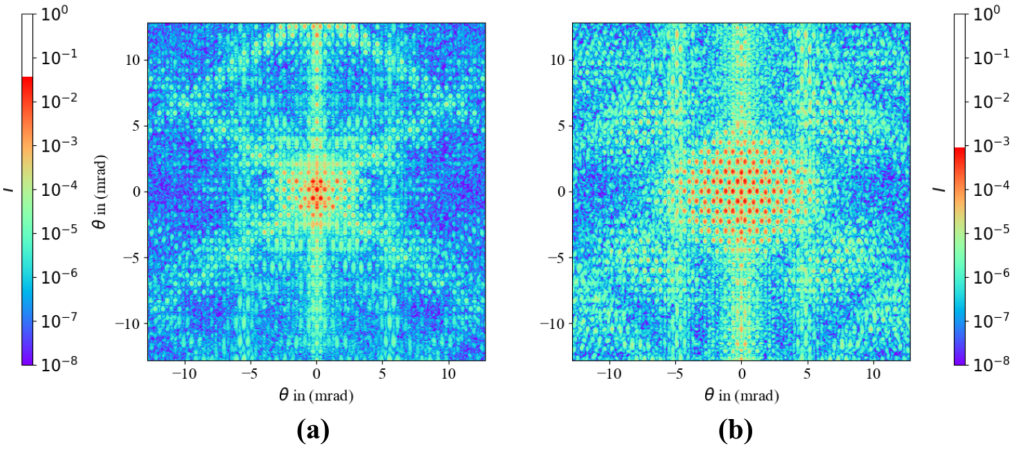

Figure 4.15.: FFDP of a triangular CCR array with a tilt of 35° (a) and 45° (b) along the x-axis.

5 Chapter 5. Optical Cross Section

After the FFDP has been experimentally verified and further analyzed in simulations, the assumptions derived can now be implemented in the OCS calculations which will be listed again in Section 5.1. This will lead to different design options and therefore different results for the OCS of retroreflective foils. For comparison a single CCR with a diameter $D_{circ} = 10\,\mathrm{mm}$ and a diffuse scattering surface is used. Alongside the calculation of the OCS and the link budget, this study will also provide the area of retroreflective foil needed to achieve the same OCS as a single circular CCR.

5.1. Assumptions for Retroreflective Foil

During this study, various investigations were conducted. In Section 2.4.1 the calculation of the OCS were derived by using Equation 2.27. In principle, this term can be separated into three partially independent components: the reduction of the retroreflective area due to the angle of incidence, the peak cross section which depends on the type of retroreflector, and the FFDP, which is influenced by both.
The reducing factors $\eta_c(\theta_i)$ and $\eta_t(\theta_i)$ for the effective area of hexagonal and triangular CCRs were already derived in Section 2.4.1. Nevertheless, assumptions for the peak OCS, the FFDP and the length of the CCRs required to calculate the maximum angle of incidence still need to be made.

5.1.1. Peak OCS

In accordance to Equation 2.15 the peak OCS for a hexagonal CCR can be determined using $A_{hex} = \frac{3\sqrt{3}}{4} D_{hex}$, resulting in

$$\sigma_{0,\,hex} = \frac{27\pi}{16\lambda^2}\,\rho_{foil}\,D_{hex}^4. \tag{5.1}$$

This formula aligns with G. Ruck et al. [36, p. 591], where, in this case, the cross section is specified based on the edge length. As already derived, this edge length can be calculated with Equation 4.4 from which the OCS can be written by

$$\sigma_{0,\,hex} = \frac{12\pi}{\lambda^2}\,\rho_{foil}\,a_c^4. \tag{5.2}$$

Equation 5.1 can also be used for a triangular CCR, with the note that it applies to the output aperture. Consequently, the triangular CCR is scaled with Equation 4.6. Equivalent to the preceding, the OCS expressed in terms of the edge length can be written by

$$\sigma_{0,\,tria} = \frac{4\pi}{3\lambda^2}\,\rho_{foil}\,a_c^4. \tag{5.3}$$

By using n CCRs the OCS will be n times that of a single CCR (cf. Section 2.1.3). The number of embedded CCRs can be determined using an area A_q and the input aperture of the respective CCRs with the equations

$$n_{hex} = \frac{A_q}{A_{hex}} = \frac{8}{3\sqrt{3}} \frac{A_q}{D_{hex}^2} \tag{5.4}$$

and

$$n_{tria} = \frac{A_q}{A_{tria,in}} = \frac{16}{9\sqrt{3}} \frac{A_q}{D_{hex}^2}. \tag{5.5}$$

Therefore, the peak OCS can be written by

$$\sigma_{0,\,hex} = \frac{3\sqrt{3}}{2} \frac{A_q\, \pi\, \rho_{foil}}{\lambda^2} (D_{hex})^2, \tag{5.6a}$$

$$\sigma_{0,\,tria} = \sqrt{3}\, \frac{A_q\, \pi\, \rho_{foil}}{\lambda^2} (D_{hex})^2. \tag{5.6b}$$

5.1.2. Adjusted FFDP

In Chapter 4 the stretch factor a_s was introduced. As already mentioned, the diffraction angle should derive from the envelope in the FFDP, neglecting the intensity distribution due to the array function, as it becomes negligible in real structures. With this factor a hexagonal diameter can be reduced to an effective diameter to maintain the assumption of an intensity distribution equivalent to that of a circular aperture. Nevertheless, it must be considered that stretching the function results in a reduction of the intensity density. If only the FFDP were modified, according to Equation 2.27, an even better value would result, as the far field only indicates the shift toward the center, and with a larger diffraction angle, the shift has a less significant impact.

Therefore, an additional factor must be introduced to normalize the stretched Airy function. This factor can be determined by the ratio of the integrals of the respective Airy functions. The reducing factor can be calculated by

$$\gamma = \frac{C_1}{C_2}, \tag{5.7}$$

where C_1 is the integral of Equation 2.8 and C_2 is the integral of Equation 4.7 within the limits of 0 to π. Numerical calculations have shown that both the diameter D_{hex} and the effective area η_c have no influence on γ, which was expected as both Airy functions depend equally on these values. Furthermore, the reducing factor is approximately equal to the stretch factor resulting in

$$\gamma \approx a_s. \tag{5.8}$$

Thus, the OCS of retroreflective foils can be written by

$$\sigma_{foil}(\theta_o, \theta_i) = a_s\, \eta_c^2(\theta_i)\, \sigma_0 \left[\frac{2J_1(x(\theta_i, \theta_o))}{x(\theta_i, \theta_o)}\right]^2, \tag{5.9}$$

where the argument $x(\theta_i, \theta_o)$ can be calculated unchanged using Equation 2.28. For the triangular foils, the corresponding effective area must be used, of course.
Alongside using $a_s = 0.911$ for a foil under perfect conditions, a smaller stretch factor will also be applied to cover larger diffraction angles in accordance with the experimental data.

5.1.3. Adaption of Length

As mentioned in Section 2.4.1, the length of a hexagonal and a triangular CCR differs from that of a circular CCR. Equivalent to L_{ccr} the length L_{tria} and L_{hex} can be defined and derived according to the same principle outlined in Section 4.2. The center point of a triangular and a hexagonal CCR is the same for both and lies at $P_0 = (0, 0, 0)$. Equivalent to Equation 4.1 the plane $E_t : x + y + z - a_c = 0$ contains the edge points of the triangular CCR. The distance between each plane and the center point can be calculated using Equation 4.2. The length can be related to the edge length a_c, or alternatively expressed as a function of the diameter which can be written by

$$L_{hex} = \frac{2}{\sqrt{3}}\, a_c = \frac{\sqrt{2}}{2}\, D_{hex}, \tag{5.10a}$$

$$L_{tria} = \frac{1}{\sqrt{3}}\, a_c = \frac{\sqrt{6}}{4}\, D_{hex}. \tag{5.10b}$$

According to Equation 2.30 the maximum angle of incidence is calculated by

$$\theta_{c,\,hex} = \arcsin\left(n_{ref} \sin\left(\arctan\left(\frac{1}{\sqrt{2}}\right)\right)\right), \tag{5.11a}$$

$$\theta_{c,\,tria} = \arcsin\left(n_{ref} \sin\left(\arctan\left(\frac{\sqrt{6}}{3}\right)\right)\right). \tag{5.11b}$$

Thus, a maximum angle of incidence of $\theta_{c,\,hex} = 56.84°$ and $\theta_{c,\,tria} = 66.5$ is obtained, compared to $\theta_{c,\,circ} = 53.54°$ for the referenced circular CCR. The triangular CCR exhibits retroreflection at higher angles of incidence, which has to consider for a comparison between all types. Therefore, $\theta_{c,\,tria}$ should be the limit for averaging the mean OCS of all CCRs, including the circular one.

5.1.4. Required Area

In addition, the required area of foil needed to reach the same OCS as a single circular CCR can be calculated. For the peak OCS Equations 2.16 and 5.6a or alternatively 5.6b can be equated which leads to

$$A_{q,\,hex} = \frac{\pi^2 \cdot \rho_{circ} \cdot D_{ccr}^4}{6\sqrt{3} \cdot \rho_{foil} \cdot (D_{hex})^2}, \tag{5.12a}$$

$$A_{q,\,tria} = \frac{\pi^2 \cdot \rho_{circ} \cdot D_{ccr}^4}{4\sqrt{3} \cdot \rho_{foil} \cdot (D_{hex})^2}. \tag{5.12b}$$

Furthermore, the required diameter D_{hex} for a given area of foil can be determined and written by

$$D_{hex} = \pi D_{circ}^2 \sqrt{\frac{\rho_{circ}}{6\sqrt{3} \cdot \rho_{foil} \cdot A_{q,hex}}}, \tag{5.13a}$$

$$D_{tria} = \pi D_{circ}^2 \sqrt{\frac{\rho_{circ}}{4\sqrt{3} \cdot \rho_{foil} \cdot A_{q,tria}}}. \tag{5.13b}$$

The term D_{tria} is used here to distinguish the required diameters and will continue to refer to the diameter of the hexagonal output aperture of triangular CCRs.

5.1.5. Velocity aberration

As already mentioned in Section 2.4.1, the diffraction angle of retroreflective foils is much larger than that of a single CCR with a diameter $D_{circ} = 10\,\text{mm}$, so that the velocity aberration has only a minimal effect on σ_{foil}. The reduction caused by the velocity aberration is within the range from 0.0002 % to 0.07 % by using diameters between $D_{hex} = 50\,\mu\text{m}$ to $400\,\mu\text{m}$. Here, the number used for averaging is reduced to $|\theta_o| = 20$.

5.2. Single circular CCR

For an initial classification a satellite equipped with a single circular CCR is considered. The link budget is calculated by using the specifications of the miniSLR@ system and Equation 2.27 for the OCS. All required parameters not taken from Table B.1 and used for the calculation are listed in Table 5.1. For a single circular CCR with a diameter $D_{circ} = 10\,\text{mm}$ a peak OCS of $\sigma_{0,circ} = 63.7 \cdot 10^3\,\text{m}^2\text{sr}^{-1}$ and a mean OCS of $\sigma_{circ} = 13.3 \cdot 10^3\,\text{m}^2\text{sr}^{-1}$ is obtained. Under an elevation angle of $\alpha_e = 20°$ which represents the worst possible conditions the ranging probability is $P_d(N_{pe}) = 0.327\,\%$.

Table 5.1.: Further parameters used for the link budget calculation of a single CCR.

Parameter	D_{circ}	L_{circ}	ρ_{circ}	n_{ref}	h_{sat}
Value	10 mm	9 mm	0.93	1.45	600 km

5.3. Diffuse Scattering

In addition to examining a single circular CCR, an orientation for the order of magnitude is useful to consider the OCS if no passive amplification is used. Assuming a diffusely reflective area A_{diff} with a reflectivity ρ_{diff} the OCS can be calculated by

$$\sigma_{diff}(\theta_i) = \rho_{diff} \cdot A_{diff} \cdot \cos(\theta_i). \tag{5.14}$$

At a wavelength of $\lambda = 1064\,\text{nm}$, the reflectivity of metallic surfaces exceeds 90 %, resulting in an OCS on the order of the utilized area, which is getting smaller in the case of high incidence angles. A mean OCS in accordance with Equation 2.31 can be estimated by neglecting the velocity aberration and averaging over $\cos(\theta_i)$ in a range from $\theta_i = 20°$ to 70° which results in a slightly lower, but still comparable OCS.

As calculated above a single CCR with a diameter $D_{circ} = 10\,\mathrm{mm}$ yields an OCS of $\sigma_{circ} = 13.3 \cdot 10^3\,\mathrm{m^2sr^{-1}}$. To achieve the same OCS by using diffuse reflective surfaces an area of $A_{diff} \approx 13 \cdot 10^3\,\mathrm{m}^2$ will be required, which corresponds to a square edge length of $a_{sat} = 114\,\mathrm{m}$.

5.4. Retroreflective foil

The following calculations of the OCS are performed by using a range of values for the reflectivity ρ_{foil} and for the diameter D_{hex}. The orbital altitude and the refractive index are taken from Table 5.1. This section will also examine the peak OCS in addition to the mean OCS.

5.4.1. Peak OCS

Figure 5.1 shows the peak OCS for an area of $A_q = 100\,\mathrm{cm}^2$, which corresponds to a 1U-sized CubeSat[1]. As previously mentioned, the analysis of the retroreflective foil focuses on low-budget missions, such as CubeSats. In alignment with the TRACE CubeSat team from the TU Darmstadt, which is planning a satellite mission utilizing a 2U CubeSat with dimensions of $(10 \times 10)\,\mathrm{cm}$ [37], a reference area of $A_q = 100\,\mathrm{cm}^2$ is used in this study.
As expected, the cross section is significantly weaker than that of the single circular CCR. The best result is $\sigma_{0,\,foil} = 10.3 \cdot 10^3\,\mathrm{m^2sr^{-1}}$ by using hexagonal CCRs with a diameter of $D_{hex} = 400\,\mathrm{\mu m}$ and $\rho_{foil} = 0.9$ (best case scenario). The OCS corresponds to approximately 16.3 % of $\sigma_{0,\,circ}$.

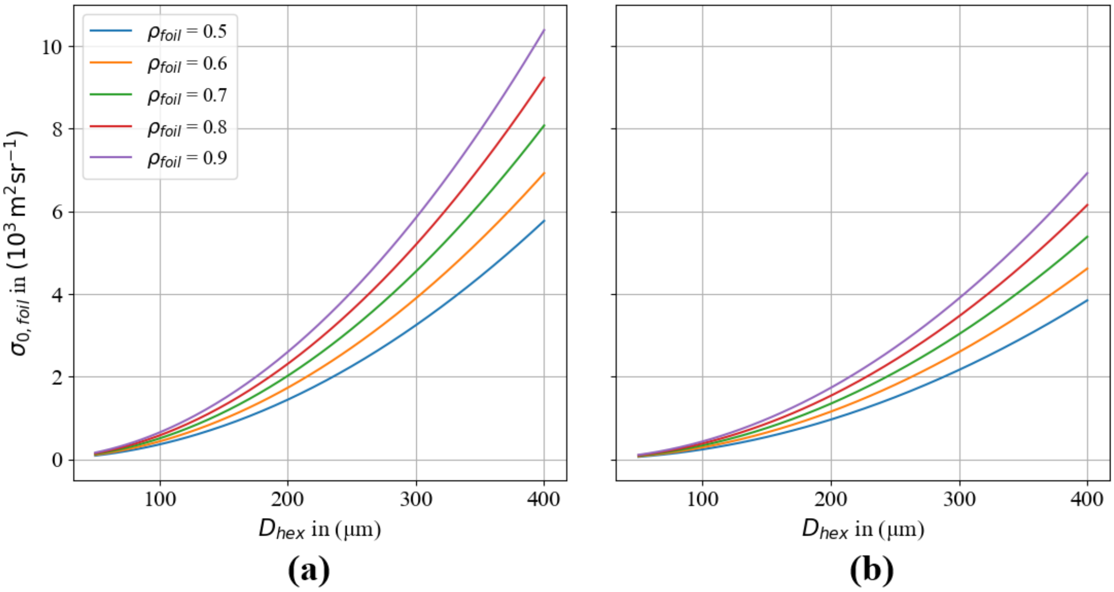

Figure 5.1.: Peak OCS of retroreflective foils with an area of $A_q = 100\,\mathrm{cm}^2$ and an utilized wavelength of $\lambda = 1064\,\mathrm{nm}$. The hexagonal CCRs (a) indicate a significantly larger cross section compared to the triangular CCRs (b). The x-axis represents the output aperture in both cases.

---

[1] The unit "U" is derived from the standard size of CubeSats, where 1U corresponds to a size of $(10 \times 10 \times 11.35)\,\mathrm{cm}$

Further Figure 5.2 show the required area, needed to reach the same peak OCS as a single circular CCR with diameter of $D_{circ} = 10\,\mathrm{mm}$. In the best case scenario an area of $A_q = 613.35\,\mathrm{cm}^2$ is required. The area corresponds to a quadratic edge length of $a_{sat} = 24.77\,\mathrm{cm}$.

In addition, Figure 5.3 shows the required diameter of embedded CCRs needed to reach the same peak OCS as the single circular CCR by using an Area of $A = 100\,\mathrm{cm}^2$. In the best-case scenario, the required diameter is approximately $D_{hex} = 1000\,\mu\mathrm{m}$.

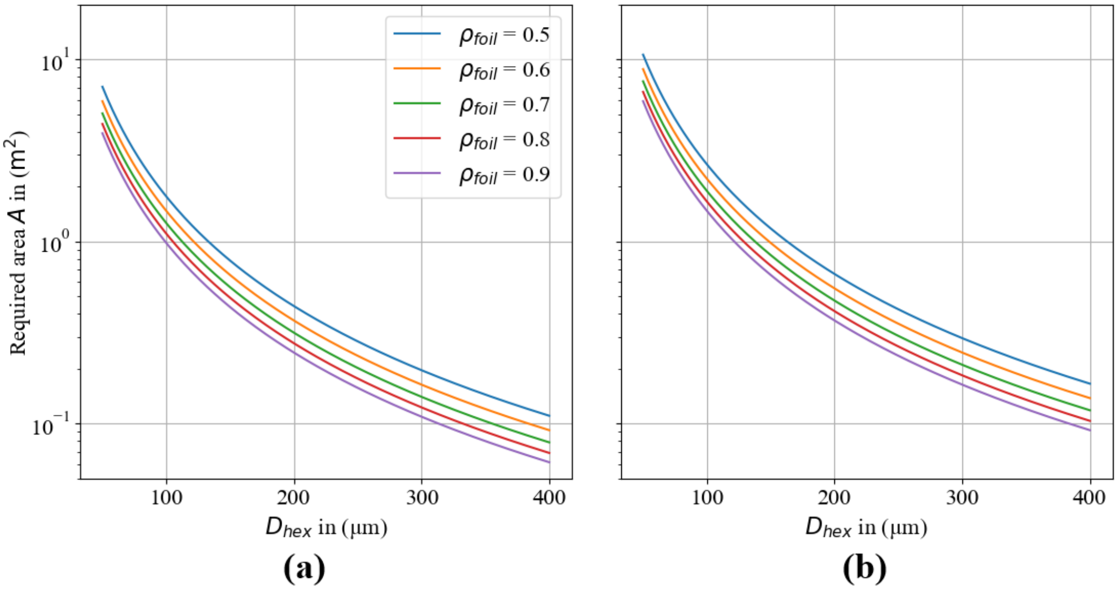

Figure 5.2.: Required area of foil needed to reach the same peak OCS as a single circular CCR with a diameter of $D_{circ} = 10\,\mathrm{mm}$. The utilized wavelength is $\lambda = 1064\,\mathrm{nm}$. The results are given for hexagonal (a) and triangular CCRs (b). The x-axis represents the output aperture in both cases.

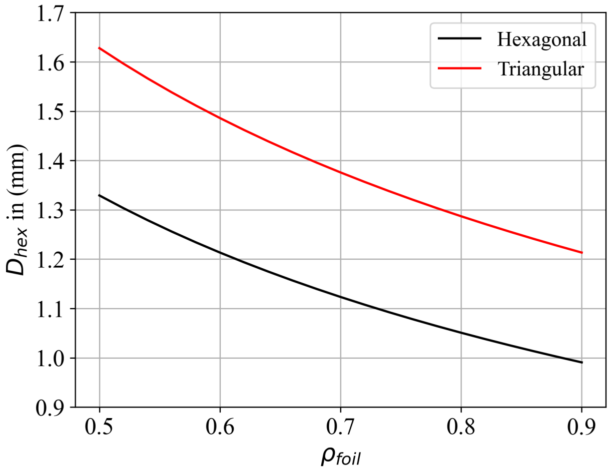

Figure 5.3.: Required diameter of embedded CCRs needed to reach the same peak OCS as a single circular CCR with a diameter of $D_{circ} = 10\,\mathrm{mm}$ by using an Area of $A_q = 100\,\mathrm{cm}^2$. The utilized wavelength is $\lambda = 1064\,\mathrm{nm}$.

5.4.2. Mean OCS

Alongside the peak OCS the mean OCS will be estimated as this generally provides a more comprehensive analysis. Figures 5.5 and 5.6 show the mean OCS in case without and with manufacturing tolerances, where, as mentioned earlier, a stretch factor of $a_s = 0.911$ is used in the first case, and $a_s = 0.39$ in the second case.

The best result is once again achieved with hexagonal CCRs exhibiting the highest reflectivity and the largest diameter. In the case of perfect foils this leads to $\sigma_{foil} = 2405\,\mathrm{m^2sr^{-1}}$, which corresponds to approximately 18.1 % of σ_{circ}. The triangular CCRs result in $\sigma_{foil} = 2303\,\mathrm{m^2sr^{-1}}$, which corresponds to approximately 17.3 % of σ_{circ}.
Assuming manufacturing tolerances the cross section is further reduced to $\sigma_{foil} = 1030\,\mathrm{m^2sr^{-1}}$ for hexagonal CCRs (7.7 % of σ_{circ}) and $\sigma_{foil} = 986\,\mathrm{m^2sr^{-1}}$ for triangular CCRs (7.4 % of σ_{circ}).
The OCS of the triangular foil is generally lower due to the reduced effective area. In addition to the previously mentioned values, Table 5.2 contains an overview of additional stretch factors, their corresponding cross sections, and ranging probabilities.

The required area equivalent to Figure 5.2 has not been calculated analytically, as it is embedded within the argument of the Bessel function. Figure 5.7 and 5.8 show the mean OCS for different diameters by a given reflectivity of $\rho_{foil} = 0.9$, where a step size of $a_{sat} = 1\,\mathrm{cm}$ is used for a quadratic edge length. In addition, the mean OCS of a circular CCR is plotted for comparison. As seen the plot is limited on the x-axis for better clarity, so that a diameter of $D_{hex} = 50\,\mu\mathrm{m}$ does not reach the mean OCS of the circular CCR by a maximum area of $A_q = 1200\,\mathrm{cm^2}$.

Nevertheless, this approach can be done for different values of reflectivity. By calculating the mean OCS as a function of the used area for different diameters, the area which leads closest to the mean OCS of the circular CCR can be collected and approximately referred to the required area. Figure 5.10 and 5.9 show the result of this method. 20 diameters in a range from 50 to 400 µm were each used for five values of reflectivity. The step size of the quadratic edge length is still $a_{sat} = 1\,\mathrm{cm}$.
For a diameter of $D_{hex} = 400\,\mu\mathrm{m}$ (hexagonal CCRs) an area of around $577\,\mathrm{cm^2}$ is required by assuming perfect conditions (a stretch factor of $a_s = 0.911$). This leads to an edge length of around 24.02 cm. By reducing the diameter the required area is rapidly increasing, for $D_{hex} = 50\,\mu\mathrm{m}$ and $\rho_{foil} = 0.5$ an edge length of $a_{sat} \approx 400\,\mathrm{cm}$ is required.

Table 5.2.: Ranging probability from different types of foil with the corresponding OCS and the mean numbers of detected photons under an elevation angle of $\alpha_e = 20°$. All values of the OCS were calculated using $\rho_{foil} = 0.9$, $D_{hex} = 400\,\mu\mathrm{m}$, Table B.1 and Table 5.2.

a_s	Type of CCR	σ in $(\mathrm{m^2sr^{-1}})$	N_{pe} in $(1 \cdot 10^{-3})$	$P_d(N_{pe})$ in (%)
-	Circular	13300	3.277	0.327
0.911	Hex. / tria.	2405 / 2303	0.592 / 0.568	0.059 / 0.057
0.66	Hex. / tria.	1743 / 1669	0.429 / 0.411	0.043 / 0.041
0.39	Hex. / tria.	1030 / 986	0.253 / 0.243	0.025 / 0.024

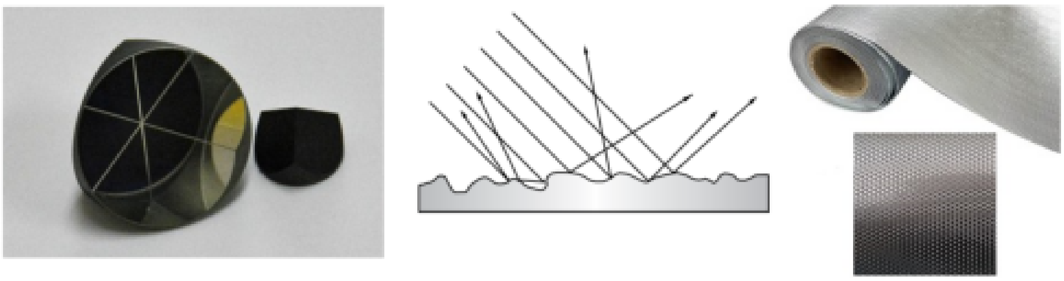

$D_{circ} = 10\,\text{mm}$

(a)

$A_q = 13{,}000\,\text{m}^2$
$a_{sat} = 114\,\text{m}$

(b)

$A_q = 577\,\text{cm}^2$
$a_{sat} = 24.0\,\text{cm}$

(c)

Figure 5.4.: Required Area of diffusely reflective surface (b) [11, p. 203] and retroreflective foil (c) [38] needed to achieve an OCS equivalent to that of a single circular CCR with $D_{circ} = 10\,\text{mm}$ (a) [39]. The foil represents the best-case scenario with a reflectivity $\rho = 0.9$, hexagonal CCRs with a diameter $D_{hex} = 400\,\mu\text{m}$ and a stretch factor of $a_s = 0.911$.

Figure 5.4 summarizes the results of the required area needed to achieve an OCS equivalent to that of a single circular CCR with $D_{circ} = 10\,\text{mm}$. Here, the optimal performance scenario for the retroreflective foil is compared against a diffusely reflecting surface.

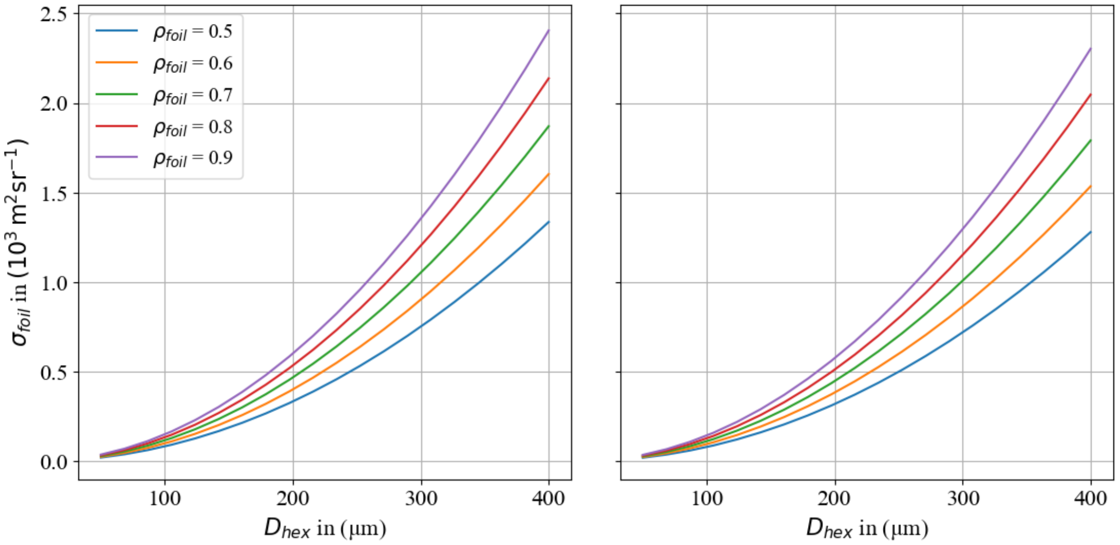

(a) **(b)**

Figure 5.5.: OCS for different types of retroreflective foils with hexagonal (a) and triangular (b) embedded CCRs using an area of $A_q = 100\,\mathrm{cm}^2$ and a stretch factor of $a_s = 0.911$. The utilized wavelength is $\lambda = 1064\,\mathrm{nm}$. The x-axis represents the output aperture in both cases.

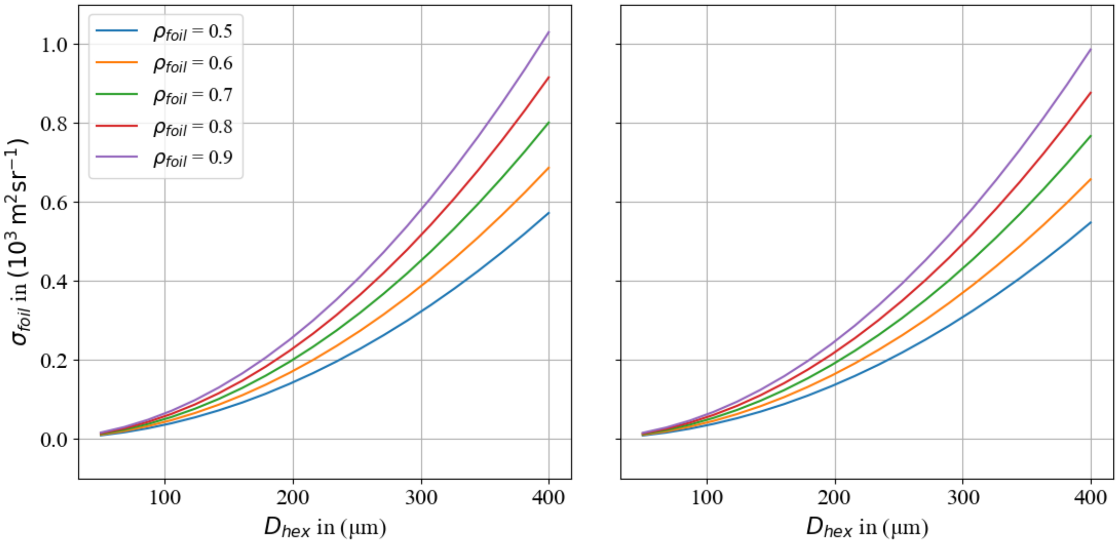

(a) **(b)**

Figure 5.6.: OCS for different types of retroreflective foils with hexagonal (a) and triangular (b) embedded CCRs using an area of $A_q = 100\,\mathrm{cm}^2$ and a stretch factor of $a_s = 0.39$. The utilized wavelength is $\lambda = 1064\,\mathrm{nm}$. The x-axis represents the output aperture in both cases.

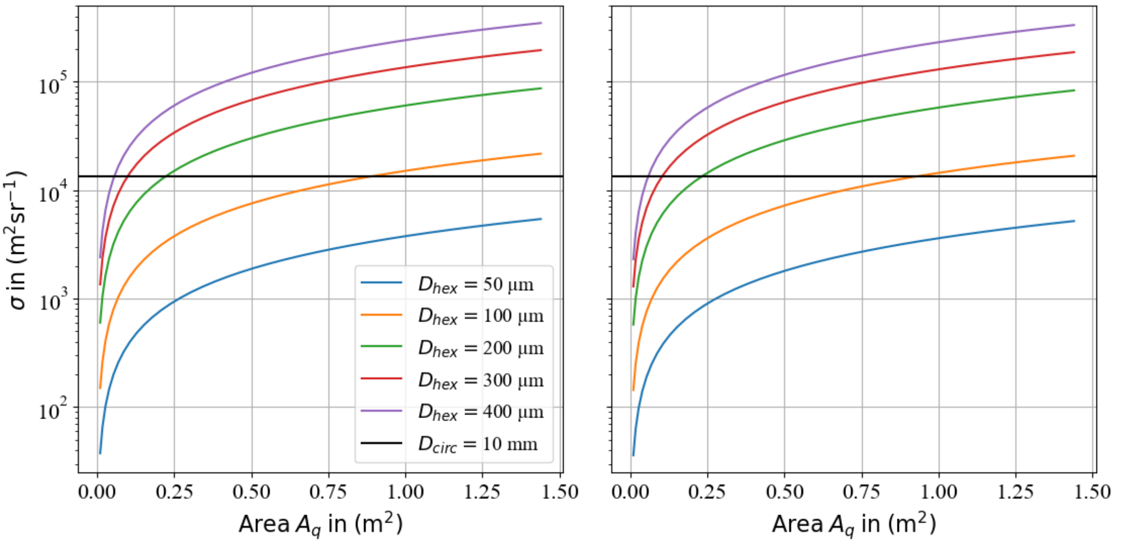

(a) (b)

Figure 5.7.: OCS of foil for hexagonal (a) and triangular (b) embedded CCRs as a function of the utilized area A_q with a stretch factor of $a_s = 0.911$ and a reflectivity of $\rho_{foil} = 0.9$. The utilized wavelength is $\lambda = 1064$ nm. In addition, the mean OCS of a circular CCR is plotted in black for comparison.

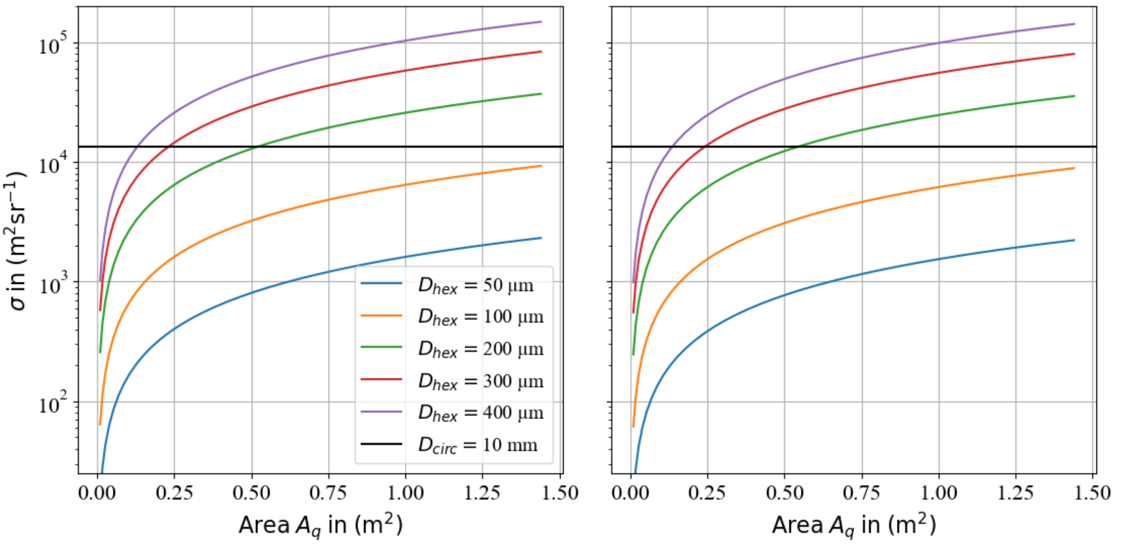

(a) (b)

Figure 5.8.: OCS of foil for hexagonal (a) and triangular (b) embedded CCRs as a function of the utilized area A_q with a stretch factor of $a_s = 0.39$ and a reflectivity of $\rho_{foil} = 0.9$. The utilized wavelength is $\lambda = 1064$ nm. In addition, the mean OCS of a circular CCR is plotted in black for comparison.

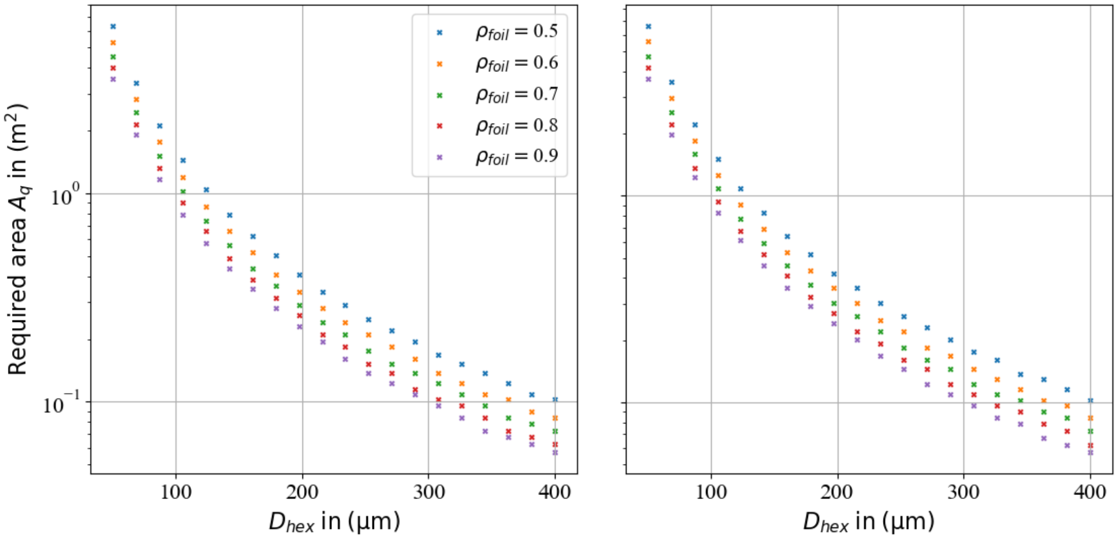

(a) **(b)**

Figure 5.9.: Required area of foil needed to reach the same OCS as a single circular CCR with a diameter of $D_{circ} = 10\,\text{mm}$. The utilized wavelength is $\lambda = 1064\,\text{nm}$. The results are given for hexagonal (a) and triangular CCRs (b) with a stretch factor of $a_s = 0.911$. The x-axis represents the output aperture in both cases.

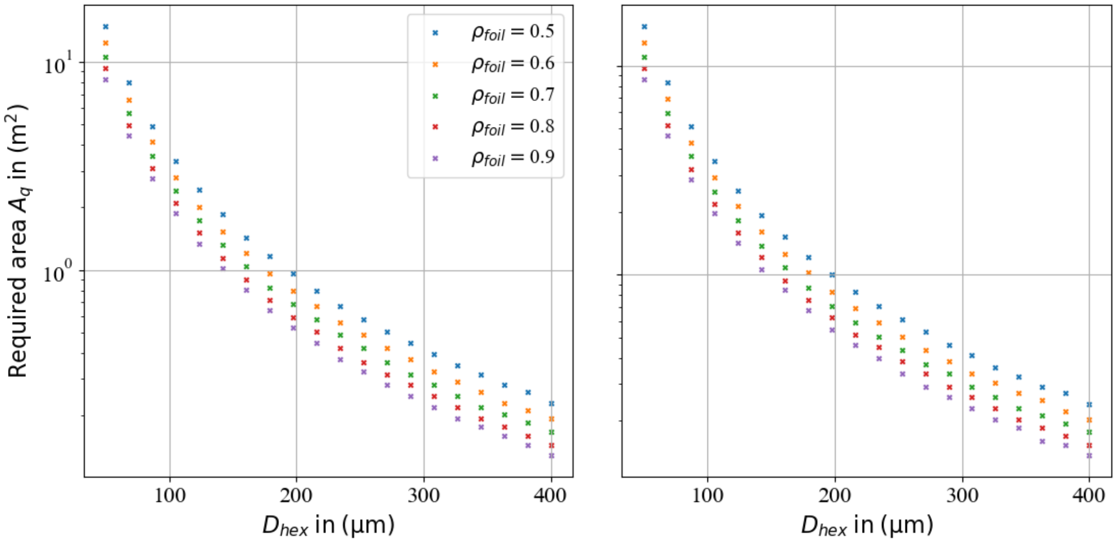

(a) **(b)**

Figure 5.10.: Required area of foil needed to reach the same OCS as a single circular CCR with a diameter of $D_{circ} = 10\,\text{mm}$. The utilized wavelength is $\lambda = 1064\,\text{nm}$. The results are given for hexagonal (a) and triangular CCRs (b) with a stretch factor of $a_s = 0.39$. The x-axis represents the output aperture in both cases.

6 Chapter 6.

Discussion

The results have shown that an OCS of retroreflective foil with an area $A_q = 100\,\mathrm{cm}^2$, hexagonal embedded CCRs with a diameter $D_{hex} = 400\,\mu\mathrm{m}$ and a reflectivity $\rho = 0.9$ reaches 18 % of the OCS of a single circular CCR with a diameter $D_{circ} = 10\,\mathrm{mm}$ and a reflectivity $\rho_{circ} = 0.93$ in the best case scenario by using a stretch factor $a_s = 0.911$. By using more realistically scenarios with $a_s = 0.39$, which takes error tolerances into account, this is further reduced to 7%.
To achieve the same OCS as that from the single CCR, an area of $A_q = 613.35\,\mathrm{cm}^2$ was first calculated based on the peak OCS, which corresponds to an square edge length of $a_{sat} = 24.77\,\mathrm{cm}$. Further a required area of $A_q = 577\,\mathrm{cm}^2$ was calculated based on the mean OCS (corresponding to an edge length of $a_{sat} = 24.02\,\mathrm{cm}$). Due to the factor of $a_s = 0.911$, a larger area would be needed in case of the mean OCS. Nevertheless, as the circular CCR performs worse in the averaging (lower OCS at higher angles of incidence compared to hexagonal and triangular CCRs) and the accuracy of the required area was limited to $a_{sat} = 1\,\mathrm{cm}$ a slightly better value of required area is achieved in case of the mean OCS. Here, the mean OCS is more essential. Nevertheless, the ratios of σ_{foils} and σ_{circ} depending on the orbit specifications, for example, the deviations between both where higher if no high angle of incidence occurs.

The OCS was calculated based on the assumption that the embedded CCRs interfere in accordance with the array theorem and, due to error tolerances, form a circular main maximum. Experimentally, however, only VC170 showed a clear correlation with this assumption. Since the diffraction patterns were more complex, no clear minima could be identified through a radial intensity analysis, which made the derivation of the diffraction angle impossible. To still account for the diffraction effects of these films, a compromise solution was adopted. It was decided to include an additional scenario in the calculation of the OCS, in which a larger diffraction angle was generally assumed. The simulations demonstrated that a randomly distributed phase shifts in the wave front lead to a blurring of the FFDP. With a higher error tolerance, a larger diffraction angle arises, which can be implemented in the calculations using the stretch factor.
For a more accurate estimation of the OCS, it is certainly reasonable to first consider developing a more precise analytical description of the intensity distribution of the foils, considering the more complex structure (isosceles triangular CCRs, macrostructure, etc.). Nevertheless, the intensity distribution alone is not sufficient for this purpose. The intensity distribution is only relevant for the FFDP, where the effective area and the peak OCS, however, are based on specific diameters of hexagonal or circular structures in case of this study. For a more accurate estimation of the OCS, a simulation-based calculation of the OCS or a semi-empirical model based on measurements of the intensity and scattering would actually be required.

Therefore, the self-developed assumptions and proprietary utilized measurements could also be improved in certain areas. For the collimation of the beam, no custom lens setup was used; instead, a beam expander developed by Thorlabs was employed, which was expected to appropriately collimate the beam. Nevertheless, using a shearing interferometer or a reference value, such as a mirror, would confirm the collimation. The calibration was simplified and neglected the angle between the wall and the camera plane. Further the effective area of hexagonal and triangular CCRs could be analytically described. H. Kim et al. [25] provides a good approach, but only D. Arnold [15] offers a complete analytical solution. The laser stability measurement was not really necessary for a qualitative analysis of the FFDPs but could be useful should absolute intensity measurements be conducted. All these points would, of course, allow for a more precise calculation of the OCS. However, a precise estimation was successfully achieved using VC170. Further, re-examining Equation 2.10, it must be assumed that many of the parameters used, especially the atmospheric attenuation factors, are subject to significant errors. A more precise calculation of the OCS would not provide an improved link budget estimation in this case. Therefore, it is sufficient to estimate the order of magnitude of the OCS of retroreflective foils and relate it to a single circular CCR with a diameter of $D_{circ} = 10\,\mathrm{mm}$, which represents the lower bound using the specifications of the miniSLR® for ranging.

For the analysis of the array structures this study developed a Python script, which can construct arrays of triangular or hexagonal CCRs with the diameter D_{hex} being adjustable as needed. Furthermore, while manufacturing tolerances could be implemented, the tilt of the array was only feasible to a limited extent with the concept of the POB files. Here, the individual files had to be exported using a Boolean function into a CAD file first. An alternative and potentially simpler method would have been to go directly through the construction with CAD.

Further investigations remain to be conducted. 3M4090 needs to be further investigated. The FFDP shows similarities to that of a trapezoid, as it is shown in R. Smith et al. [17]. Since the arrays have already investigated through simulations at an angle, it would also be desirable to consider this in the setup, which would represent a combination of both incoherent cases.
A large parameter range was used for the reflectivity. The specifications sheets of the foils provide a norm that specifies only the absolute values of the reflected intensity. Since the norms vary depending on the datasheets it would probably be the easiest to determine the reflectivity's experimentally on one's own.
To simplify the design of retroreflective foils, the manufacturing tolerances could be set as a function of the diffraction angle. For this, a threshold for the intensity could be defined, such that within a specific angle a certain proportion of the total intensity is contained. In this way, also manufacturing limits could be defined should retroreflective foils find practical applications.

7 Chapter 7.

Conclusion

This Thesis has analyzed the diffraction behavior and the cross section of commercially available retroreflective foils in depth. It can be used to calculate the cross sections for retroreflective foils with a wide range of different specifications, including the diameter, the type, and the reflectivity of the embedded CCRs.
This study has classified retroreflective foils into different types and related the respective output apertures to their diffraction patterns. The diffraction phenomena observed in the experiment were successfully related with the array theorem and simulation based investigations. It was demonstrated how manufacturing tolerances impact the FFDP, ultimately leading to an increase in the diffraction angle. From the combination of experimental and simulation based data, corresponding assumptions could be made to calculate the OCS, not only for perfect foils but also for a much more realistic scenario involving these manufacturing tolerances.

The results indicate that the use of retroreflective foil for SLR is not possible for CubeSats of the size 1 to 2 U if the diameter is limited to $D_{hex} = 400\,\mu\text{m}$ and the performance of the SLR is restricted to the specifications of the miniSLR®. Nevertheless, the OCS of the foils is still 10 to 20 % of that from a single circular CCR with a diameter of $D_{circ} = 10\,\text{mm}$ under these conditions and lies within 5 orders of magnitude above that of a diffusely reflecting surface. By using $D_{hex} = 1000\,\mu\text{m}$ and an area of $A_q = 100\,\text{cm}^2$ the OCS of the single CCR is already achieved.

Furthermore, this study did not address potential applications and material adjustments under space conditions, as it would exceed the scope of this research. In addition, the potential area which could be used for the foils was not further investigated. Nevertheless, one potential application could be the reduction of light emission, for instance. At the end of a satellite mission's operational life, deorbiting can be achieved using so-called drag sails, which save fuel and thus reduce costs. Nevertheless, these sails generally contribute significantly to light pollution, which interferes with astronomical observations. If the drag sails were coated with retroreflective foils, the light pollution would be rapidly reduced.
Should additional potential applications arise, they will certainly depend on further parameters, particularly material properties. With the simulated tolerance errors, as explained in Chapter 6, the tolerance can be set as a function of the diffraction angle to establish manufacturing limits. This study can further support and significantly accelerate the overall design process by calculating the OCS of a retroreflective foil with the Python scripts, based on thoroughly explained assumptions.

A

Appendix A.

Calculations

A.1. Velocity aberration

For the velocity aberration the slant range has to be split into components expressed in the reference frame of the satellite. Most of the terms were already discussed in Section 2.4. The unit vector from center of the Earth to the satellite can be written by

$$\hat{s} = \left[0, h_{sat} + h_{station} + R_E, 0\right]. \tag{A.1}$$

Assuming the satellite is moving in a circular orbit, the tangential velocity can be calculated by the first cosmic velocity

$$v_t = \sqrt{\frac{GM_E}{R_E}}, \tag{A.2a}$$

$$\hat{v} = \left[v_t, 0, 0\right], \tag{A.2b}$$

where v_t is the tangential velocity of the satellite, G the gravitational constant and M_E the mass of earth. With Figure C.5 the slant range R can be geometrically determined via

$$R^2 = (R_E + h_{sat})^2 + (R_E + h_{station})^2 - 2 \cdot (R_E + h_{sat}) \cdot (R_E + h_{station}) \cdot \cos(\varphi). \tag{A.3}$$

Rearranging for $\cos(\varphi)$ yields

$$\cos(\varphi) = \frac{2R_E \cdot (R_E + h_{sat} + h_{station}) + h_{sat}^2 + h_{station}^2 - R^2}{2R_E \cdot (R_E + h_{sat} + h_{station}) + h_{sat} h_{station}}. \tag{A.4}$$

Because the calculations belong in the reference frame of the satellite, the elevation angle α_e must be considered. Therefore, the components of the slant range can be written by

$$R_x = R\cos(\varphi + \alpha_e), \tag{A.5}$$

$$R_y = R\sin(\varphi + \alpha_e). \tag{A.6}$$

Then the unit vector from the SLR station to the satellite can be written by

$$\hat{r} = \left[R_x, R_y, 0\right] \tag{A.7}$$

B

Appendix B.

Tables

Table B.1.: Specifications of the miniSLR® system with the assumptions of the transmission coefficients of the atmosphere.

Symbol	Size	Description
λ	1064 nm	Wavelength
E_p	$100 \cdot 10^{-6}$ J	Pulse energy
δ_d	$50 \cdot 10^{-6}$ sr	Field beam divergence
η_{obs}	0.1	Obscuration of secondary mirror
η_q	0.25	Quantum efficiency
τ_{filter}	0.9	Transmission efficiency of filter
τ_r	0.2	Transmission efficiency of receiver
τ_t	0.7	Transmission efficiency of transmitter
τ_c	0.8	Transmission efficiency of cirrus clouds
τ_{atm}	0.39	Transmission efficiency of atmosphere
$h_{station}$	480 m	Altitude of system above the sea level

Table B.2.: Specifications of the examined retroreflective foils. The values of D_{hex} are given in µm. The suffix "B" in R3AB indicates the type of application, specifying whether it is rigid or flexible. The adhesive layer was identified through independent testing, whereby *for metal surfaces* was recommended by the specification sheet.

	M149-20	M120-24	VC170	OR6910	F056	3M4090
Type of CCR	Hexagonal	Hexagonal	Triangular	Triangular	Triangular	-
D_{hex} (manufacturer)	400	300	50-100	50-100	200	-
D_{hex} (DIC)	462	345	67	100	100	-
Reflectivity class	-	-	RA3	RA3B	-	RA3
Construction type	-	-	C	C	-	C
Coating	-	-	Aluminum	Total reflection	Aluminum	-
Adhesive layer	No	No	For metal surfaces	For metal surfaces	Yes	For metal surfaces
Flexibility	Lasercube®	Lasercube®	Flexible	Flexible	Flexible	Flexible
Company	IMOS®	IMOS®	ORAFOL®	ORAFOL®	IMOS®	3M®

Table B.3.: Inventory list of optical systems used in the experimental setup.

Optical system	Description	Specification	Function	Company
Laser	Helium-neon laser	Maximum output power: 4.5 mW, wavelength: $\lambda = 632.8\text{nm}$	Collimated light source	Spectra-Physics®
Beam expander	Achromatic fixed magnification beam expander GBE20	20x expansion, $400 - 650\,\text{nm}$ AR coating	Expansion and collimation	Thorlabs®
Beam splitter	Laser line non-polarizing cube beam splitter	$(25 \times 25 \times 1.5 \pm 0.1)\,\text{mm}$	Splitting laser beam	TECHSPEC®
Screen	Screen with retroreflective foils	Aluminum 7075	Mount for foils	Intern manufactured
Camera	Fujifilm XE-2	16.3 Megapixel, image resolution 4.896×3.264 (3:2)	Capturing FFDPs	Fujifilm®
Photodiode sensor	PD300-UV	Aperture size $(10 \times 10)\,\text{mm}$, Spectral range $220 - 1100\,\text{nm}$, Power Range $2\,\mu\text{W} - 300\,\text{mW}$	Intensity measurement for laser stability	Ophir®

Appendix C.

Plots

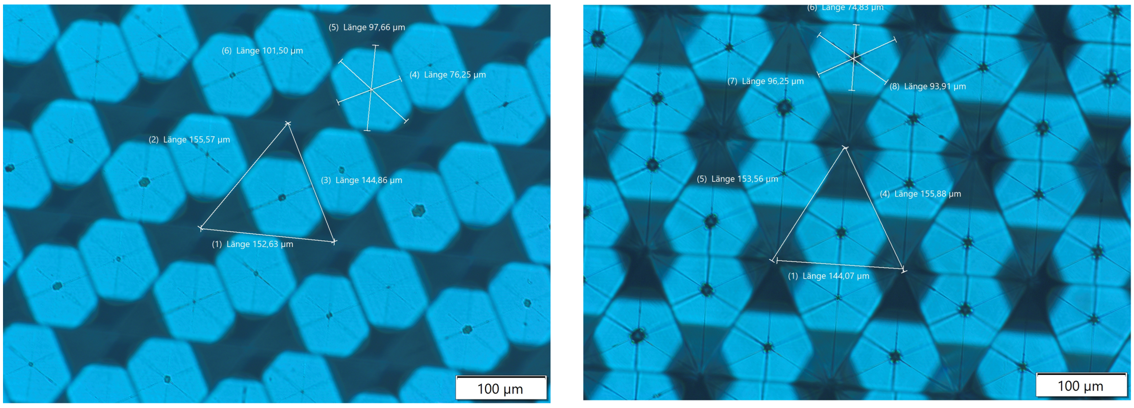

(a) **(b)**

Figure C.1.: Microscopic structure of F056 (a) and OR6910 (b). One of the three triangular edge lengths is significantly shorter in each case.

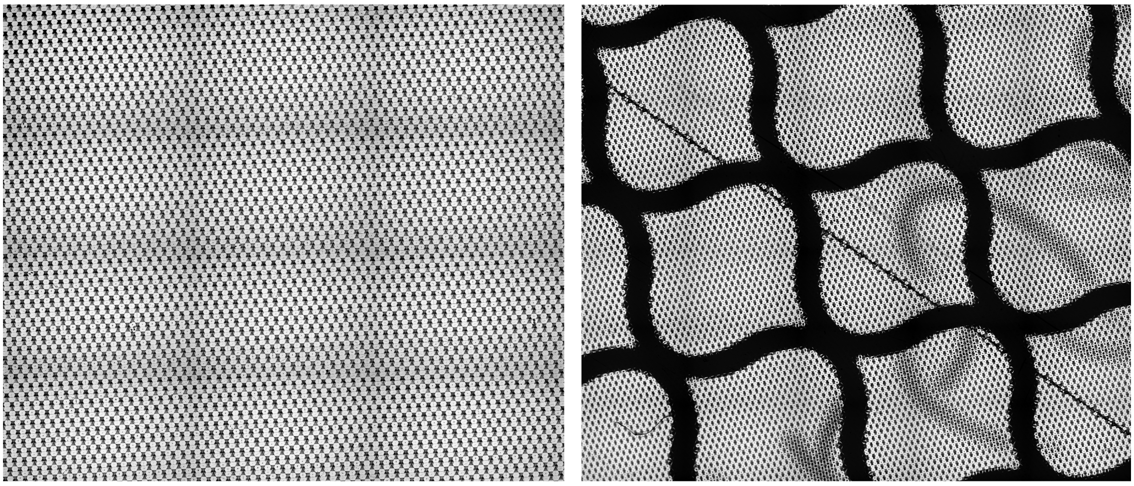

(a) **(b)**

Figure C.2.: Macroscopic structure of F056 (a) and OR6910 (b). Within the dark pattern used for identification, no CCRs are embedded.

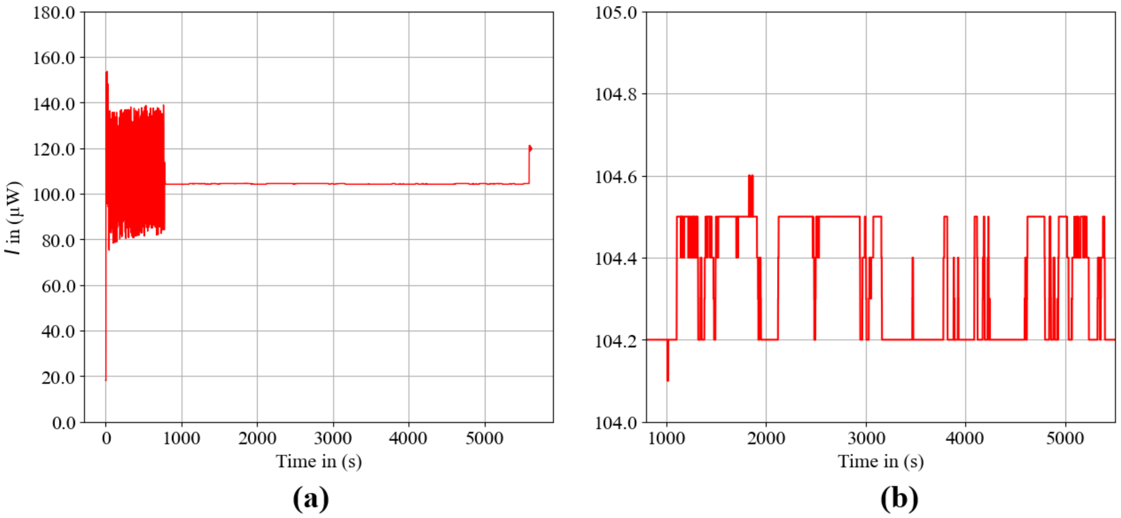

Figure C.3.: Measurement of the stability of the Helium-Neon laser. In addition to the overall measurement (a), the fluctuations due to operating time are also presented (b).

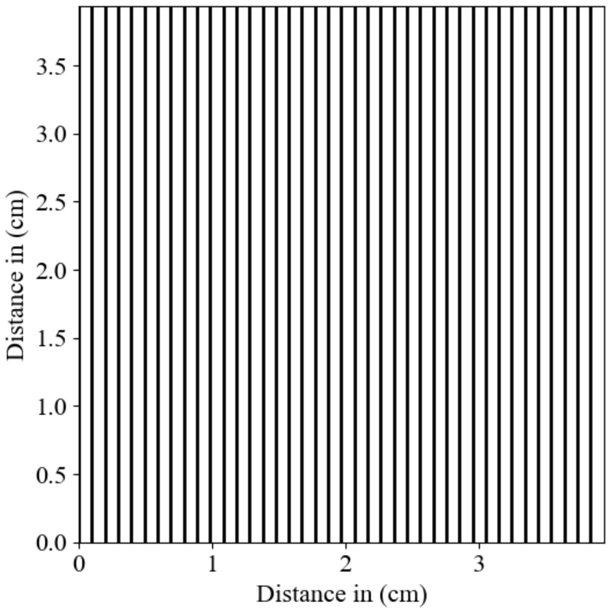

Figure C.4.: Calibration tool with a line distance of 0.25 cm. The figure has been scaled down for this representation and is therefore not to scale.

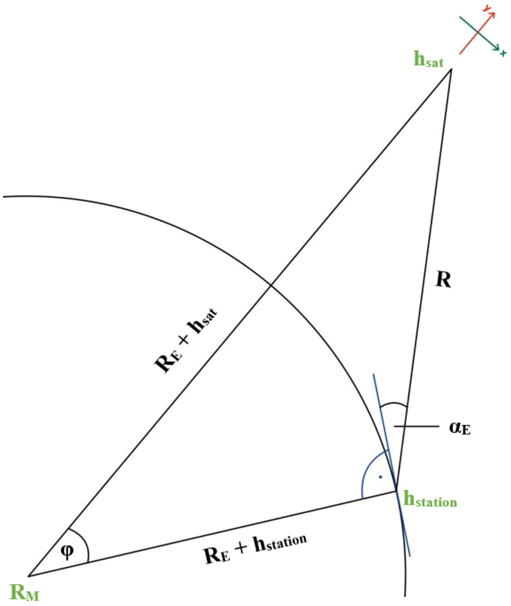

Figure C.5.: Schematic of Slant range split into components

C.1. Simulation Data

The following plots presents additional results from the analysis of the FFDPs of the optical systems discussed in Chapter 4, where $D_{circ} = D_{hex} = 460\,\mu\text{m}$ and $\lambda = 633\,\text{nm}$ applies to all plots.

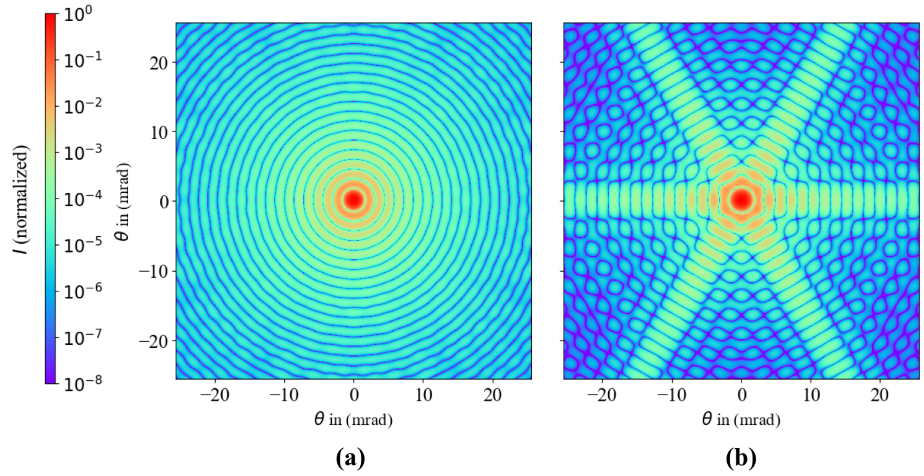

Figure C.6.: FFDPs of a circular (a) and a hexagonal (b) aperture within a wider angular range.

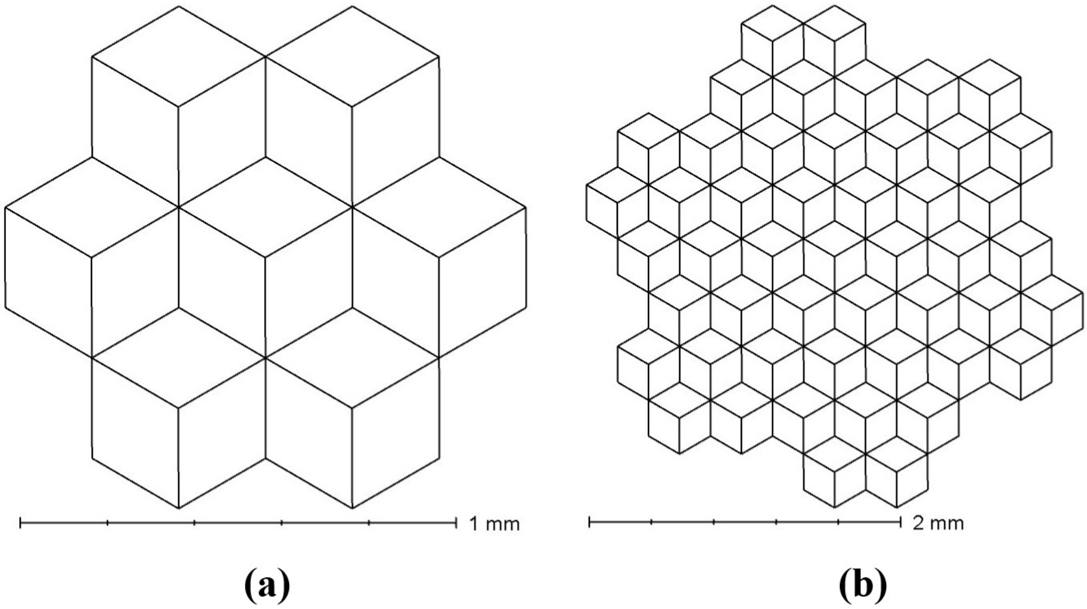

Figure C.7.: POB file of the hexagonal CCR array. After defining the points of one CCR, they were rotated five times by 60 degrees around a fixed point (a), and subsequently translated multiple times (b).

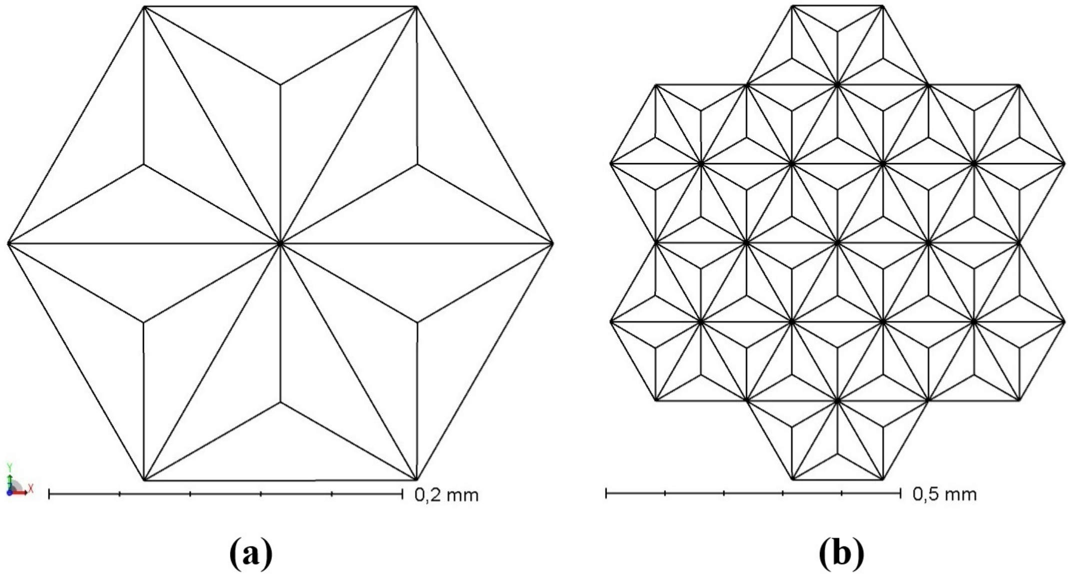

Figure C.8.: POB file of the triangular CCR array. After defining the points of one CCR, they were rotated five times by 60 degrees around a fixed point (a), and subsequently translated multiple times (b).

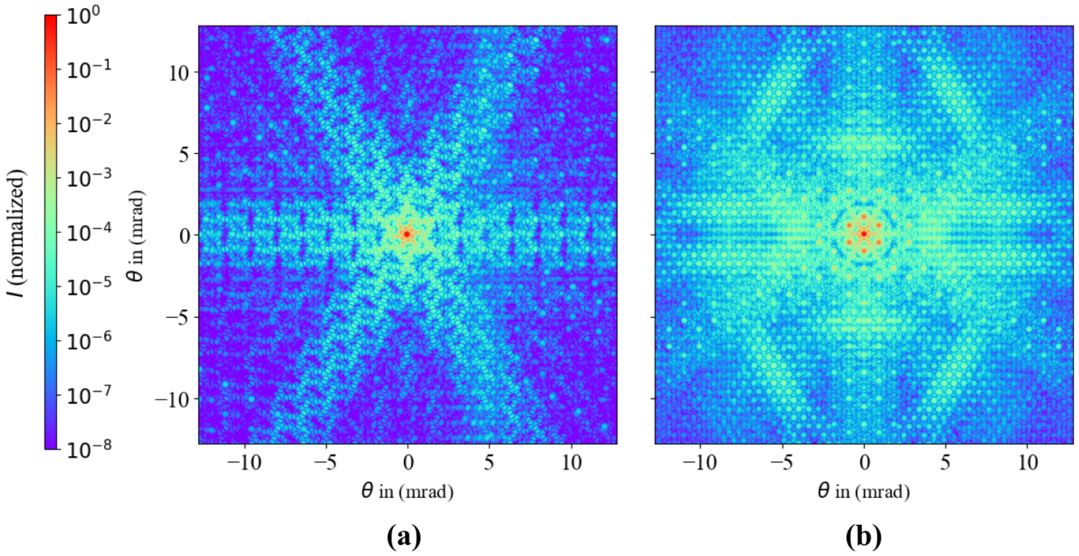

Figure C.9.: FFDPs of a hexagonal (a) and a triangular (b) CCR array within a wider angular range. The enveloped distribution of the single CCR embedded in the array is clearly visible. In addition to the first minimum in the triangular array, the hexagonal array also exhibits higher orders.

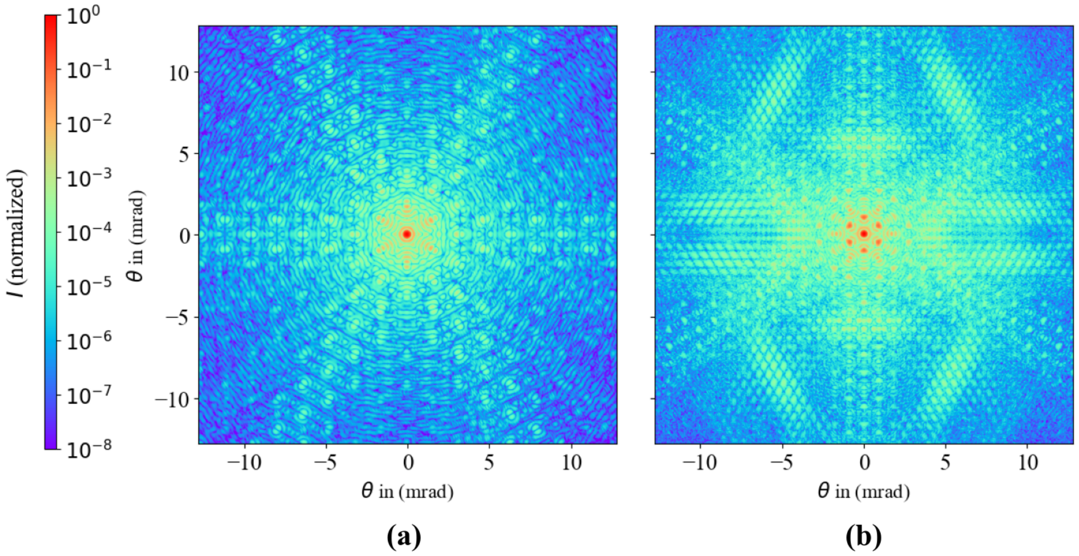

Figure C.10.: FFDPs of a hexagonal (a) and a triangular (b) CCR array within a wider angular range. The enveloped distribution of the single CCR embedded in the array is clearly visible. In addition to the first minimum in the triangular array, the hexagonal array also exhibits higher orders.

Bibliography

[1] NASA, “Cubesat 101: A Beginner’s Guide to CubeSats,” tech. rep., NASA, 2017.

[2] P. Sauer, G. Kirchner, M. Michel, V.Neumann, C. Webera, D. Autha, R. Bertrand, and S. Breuer, “Examining retro-reflective foils for use in smallsat applications and space debris laser ranging,” in *Proceedings of the 72nd International Astronautical Congress (IAC)*, (Dubai, United Arab Emirates), pp. 1–5, International Astronautical Federation (IAF), October 2021.

[3] H. Klinkrad, “Weltraummüll - Eine Gefahr für die Raumfahrt,” *Physik in unserer Zeit*, vol. 43, no. 2, pp. 64–71, 2012.

[4] M. Wilkinson, U. Scheriber, I. Procházka, C. Moore, J.Degnan5, G. Kirchner, Z. Zhongping, P. Dunn, V. Shargorodskiy, M. Sadovnikov, C. Courde, and H. Kunimori, “The next generation of satellite laser ranging system,” *Journal of Geodesy*, vol. 93, pp. 2227–2247, 2019.

[5] D. Hampf, P. Wagner, E. Schafer, P. Mösbauer, P. Lützen, and W. Riede, “MiniSLR: A fully automated miniature satellite laser ranging ground station,” in *Proceedings of the International Astronautical Congress, IAC*, 2018.

[6] M. Pearlman, C. Noll, E. Pavlis, F. Lemoine, L. Combrink, J. Degnan, G. Kirchner, and U. Schreiber, “Laser geodetic satellites: a high-accuracy scientific tool,” *Journal of Geodesy*, vol. 93, pp. 2181–2194, 2019.

[7] G. Xu, *Sciences of Geodesy - I.* Heidelberg: Springer-Verlag, 2010.

[8] J. Bennett, J. Sang, C. Smith, and K. Zhang, “Accurate orbit predictions for debris orbit manoeuvre using ground-based lasers,” *Advances in Space Research*, vol. 52, no. 11, pp. 1876–1887, 2019.

[9] J. Degnan, “Millimeter Accuracy Satellite Laser Ranging: A Review,” *Contributions of Space Geodesy to Geodynamics: Technology*, vol. 25, pp. 133–162, 1993.

[10] M. Born and E. Wolf, *Principles of Optics.* London: Camebridge University Press, 2019.

[11] E. Hecht, *Optik.* Berlin: De Gruyter, 2023.

[12] G. Brooker, *Modern Classical Optics.* Oxford: Oxford University Press, 2003.

[13] W. Demtröder, *Experimentalphysik 2 - Elektrizität und Optik.* Berlin: Springer-Verlag gmbH, 2017.

[14] B. D. Guenther, *Modern Optics Simplified.* Oxford: Oxford University Press, 2020.

[15] D. Arnold, “Method of calculating retroreflector-array transfer functions,” Tech. Rep. NASA-CR-157932, Smithsonian Astrophysical Observatory, 1978.

[16] F. Pedrotti, L. Pedrotti, W. Bausch, and H. Schmidt, *Optik für Ingenieure Grundlagen.* Berlin: Springer-Verlag, 2005.

[17] R. Smith and J. S. Marsh, “Diffraction patterns of simple apertures,” *Journal of the Optical Society of America*, vol. 64, no. 6, pp. 798–803, 1974.

[18] H. Eckhardt, “Simple Model of Corner Reflector Phenomena,” *Applied Optics*, vol. 10, no. 7, pp. 1559–1566, 1971.

[19] J. Kästel and J. Speiser, “Laser-based space debris removal: design guidelines for coherent coupling power transmission,” in *High-Power Lasers 2016: Technology and Systems* (H. Ackermann, W. L. Bohn, and D. H. Titterton, eds.), vol. 9990, p. 99900L, International Society for Optics and Photonics, SPIE, 2016.

[20] A. Brown, *Active electronically scanned arrays: fundamentals and applications.* John Wiley & Sons, 2021.

[21] C. Balanis, *Antenna Theory: Analysis and Design.* John Wiley & Sons, 2016.

[22] M. Skolnik, *Introduction to Radar Systems.* McGraw-Hill Book Company, 1981.

[23] M. Fitzmaurice, P. Minott, J. Abshire, and H. Rowe, “Prelaunch testing of the laser geodynamic satellite (LAGEOS),” Tech. Rep. 78N10200, NASA, 1977.

[24] J. Degnan, “A Tutorial on Retroreflectors and Arrays Used in Satellite and Lunar Laser Ranging,” *Photonics*, vol. 10, no. 11, p. 1215, 2023.

[25] H. Kim and B. Lee, “Optimal design of retroreflection corner-cube sheets by geometric optics analysis,” *German Academic Society for Production Engineering*, vol. 46, no. 9, pp. 1–14, 2007.

[26] J. Yuan, S. Chang, S. Li, and Y. Zhang, “Design and fabrication of micro-cube-corner array retro-reflectors,” *Optics Communications*, vol. 209, no. 1-3, pp. 75–83, 2002.

[27] H. Seward and S. Cort, “Measurement and characterization of angular reflectance for cube-corners and microspheres,” *Optical Engineering*, vol. 38, no. 1, pp. 164–169, 1999.

[28] B. C. Park, T. B. Eom, and M. S. Chung, “Polarization properties of cube-corner retroreflectors and their effects on signal strength and nonlinearity in heterodyne interferometers,” *Applied Optics*, vol. 35, no. 22, pp. 4372–4380, 1996.

[29] E. Brinksmeier, R. Glaebe, and C. Flucke, “Manufacturing of molds for replication of microcube corner retroreflector,” *Production Engineering*, vol. 2, no. 1, pp. 33–38, 2008.

[30] E. Brinksmeier, R. Gläbe, and L. Schönemann, “Diamond Micro Chiseling of large-scale retroreflective arrays,” *Precision Engineering*, vol. 36, no. 4, pp. 650–657, 2012.

[31] Altechna, “Corner Cube Retroreflector.” https://www.altechna.com/products/corner-cube-retroreflector/, 2024. Accessed on: September 16, 2024.

[32] R. Chang, D. G. Currie, C. . Alley, and M. E. Pittman, “Far-Field Diffraction Pattern for Corner Reflectors with Complex Reflection Coefficients,” *Journal of the Optical Society of America*, vol. 61, no. 4, pp. 431–438, 1971.

[33] M. Naboulsi, H. Sizun, and F. Fornel, “Propagation of optical and infrared waves in the atmosphere,” *Proceedings of the Union Radio Scientifique Internationale*, vol. 43, no. 2, pp. 64–71, 2005.

[34] Zemax LLC, *Zemax OpticStudio User Manual.* Zemax LLC, Canonsburg, PA, USA, 23.1 ed., 2023. Available as PDF, not publicly accessible online.

[35] C. Preza, D. Snyder, and J. Conchello, “Theoretical development and experimental evaluation of imaging models for differential-interference-contrast microscopy,” *Optical Society of America*, vol. 16, no. 9, pp. 2185–2199, 1999.

[36] G. Ruck, D. Barrick, W. D. Stuart, and C. K. Krichbaum, *Radar Cross Section Handbook 2.* Peninsula Publishing, 1970.

[37] L. Jung, “Trace – cubesat team,” 2024. Accessed: 12th November 2024.

[38] kayashop, “Mylar diamond "light" meterware,” 2024. Accessed: 11th November 2024.

[39] R. P. AG, “Corner cube prisms,” 2024. Accessed: 11th November 2024.